Geodetic study of gravity and sea level changes in the coastal regions of north Australia and Thailand Gulf using multiple sensors

Master Thesis

Space Geodesy Laboratory, Earth and Planetary Dynamics, Natural History Sciences, Graduate School of Science, Hokkaido University

Yuta Tokui

Supervisor : Kosuke Heki

February 2020

要旨

海水面の変動は、地球温暖化が問題となっている現代において非常に重要な課題である。海水面変動には陸水流入や風による吹き寄せなど質量変化を伴うものと、海水の熱膨張による体積変化という大きく２つの要因があることが知られている。本研究では、衛星観測・現地観測の双方を含む様々な測地観測技術の結果を利用して、東南アジアおよびオーストラリア地域から水深の浅い２つの湾（カーペンタリア湾およびタイランド湾）を取り上げ、それらの海域での海水面変動と、その周辺地域も含めた重力変化について議論する。これらの地域の特徴は、水深が浅く熱膨張による海水面変動が小さいこと、風の吹き寄せによる季節変動が大きいこと、そして海洋潮汐モデルの不確実性が大きいことが挙げられる。この潮汐モデルの不確実性が衛星観測のデータに与える影響を評価するため、現地観測と衛星観測のデータの比較も行う。

衛星高度計での観測結果は、2 つの湾でともに最大 50cm を超える海面高の季節変化が存在することを示し、その振幅・位相は潮位計で観測されたものと良い一致を示した。また、カーペンタリア湾でのより長期的な変化は、代表的な気候変動である ENSO の影響を受けていた。また、重力衛星 GRACE で観測された重力の季節変化も、海面高と同じ位相を示した。タイランド湾では振幅も非常に良い一致を見せたが、カーペンタリア湾では高度計や潮位計で観測されたものに比べ半分以下の振幅にとどまった。これは湾が大陸に囲われていることによって、空間分解能が悪い GRACE の信号が見かけ上弱く表れていることを示唆している。また、重力の非季節性変化も ENSO との相関を陸海問わず示したが、これは ENSO による降雨と風の変化が組み合わさることによって生じていると考えられる。

さらに、GRACE で観測される重力季節変化は陸（オーストラリア北部）と海（カーペンタリア湾）で位相がやや異なっていることを示した。この違いが GNSS を用いて陸上における変位として観測できるか試みた。GNSS の水平変位の季節変化は最大 6mm 前後に達し、荷重の存在する方位を示す水平変位の向きは GRACE で観測される荷重の変化を反映するものであった。観測された水平変位が GRACE や衛星高度計で観測された陸水および海水荷重の季節変化によって起こされうるか確かめるため、荷重モデルと荷重グリーン関数を用いた地殻変形の計算を行なった。カーペンタリア湾では変位の絶対量は観測値の半分程度の値にとどまったが、変位の方向は実測値と良い一致を示した。一方タイランド湾では、変位の量は実測値に比べかなりばらつきが大きく、変位方向もモデルとの一致度は低かった。これはカーペンタリア湾と異なり湾を囲う陸地が細い半島であるため、陸水荷重の影響が水平変位にあまり出ないせいではないかと考えられる。

全体を通して、心配された潮汐モデルの誤差の衛星観測値への影響は大きくないことがわかった。そして、陸海が複雑に混ざった地域での荷重変化を考える上で、GNSS 局の季節的地殻変動の水平変位の方位が陸海の荷重の位相の違いを見る手段として有効であることが示された。

Table of contents

Chapter1 Introduction

1.1 Sea level change

Sea level rise is a hot topic of urgent importance, especially for those living in coastal areas. According to Intergovernmental Panel on Climate Change (IPCC) 5th report, the Global Mean Sea Level (GMSL) has risen by up to ~20 cm in 20th century (Figure1-1). Increase of sea surface height (SSH) occurs in two mechanisms, (1) water movement from land to sea, (2) thermal expansion of seawater (Figure1-2). Mass redistribution (change in ocean bottom pressure) is associated only with (1) and not by (2).

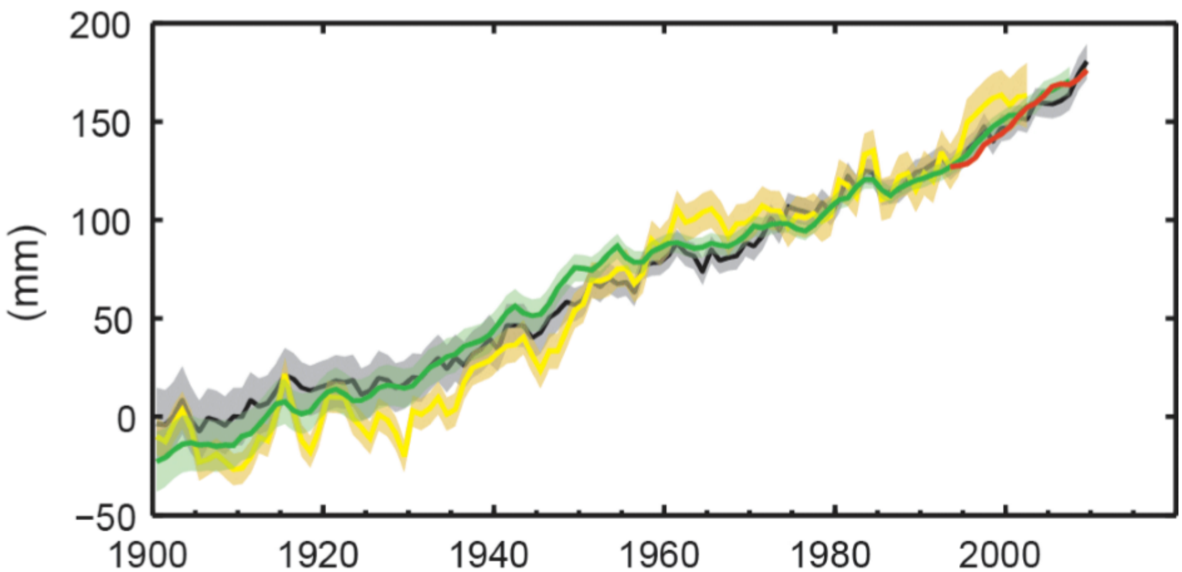

Figure1-1: GMSL change since 1900 by space-born ocean altimeters (red line) and by tide gauges (others) (IPCC 5th report) .

1.1.1 Mass redistribution between land and sea

Water exchanges among land, atmosphere, and ocean occur in various forms such as precipitation (atmosphere to land), river discharge (land to ocean), and evaporation (land to atmosphere, ocean to atmosphere). Part of these circulations can be monitored by satellite observations (Figure1-2: GMSL data seasonal remained). In recent years, it is well known that melting of mountain glaciers and continental ice sheets in polar and high mountain regions melt and cause GMSL rise (Figure1-3).

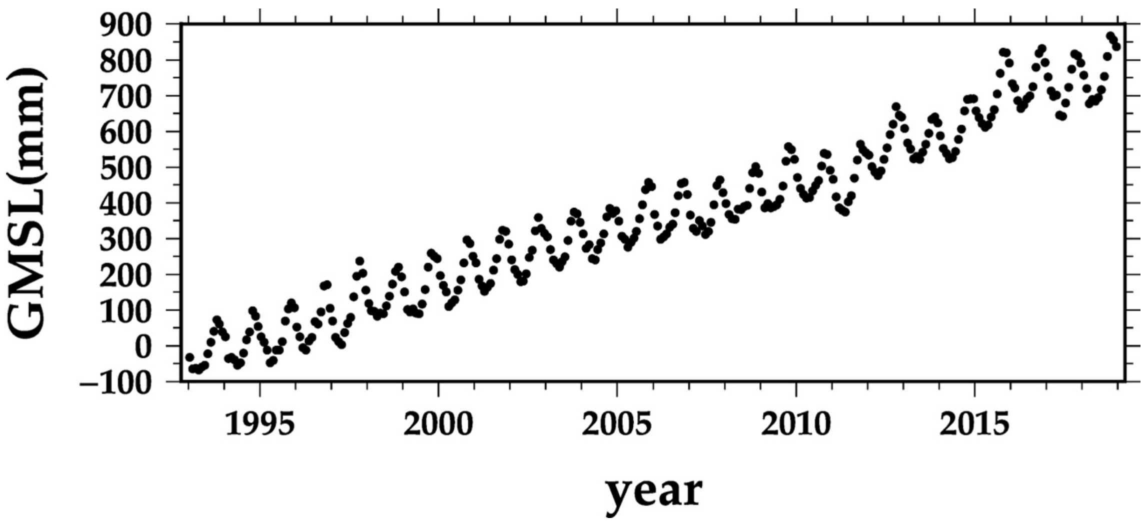

Figure1-2: GMSL from altimetry (data from AVISO)

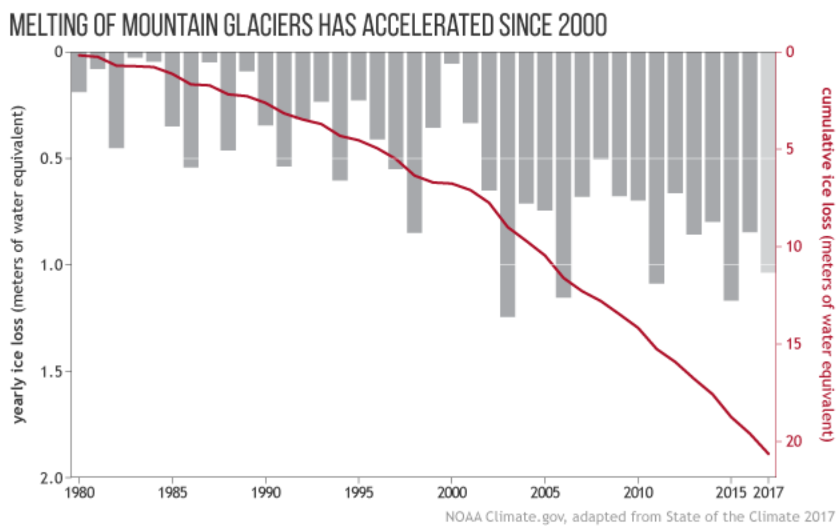

Figure1-3: Mass balance (gray bars) of 37 worldwide glaciers 1980-2017 with available data spanning 30-year or more. Observations for 2017 are preliminary. Cumulative mass losses (orange line) have accelerated around 2000. As of 2016, the total ice loss amounts to ~20 meters in equivalent water thickness (Credits, NOAA; https://www.climate.gov/news-features/understanding-climate/climate-change-glacier-mass-balance).

1.1.2 Thermal Expansion of seawater

Fresh water has the highest density in 4°C. In contrast, density of sea water is dominated by not only temperature but also salinity. These 2 factors play important roles in the circulation of seawater in open ocean. Circulation in deep ocean is often called “thermohaline circulation”. Generally, salinity of seawater varies between 33-36 PSU (Practical Salinity Units) in open ocean. Figure1-4 shows the temperature and salinity dependence of density referred to as the Temperature-Salinity Diagram from NASA (https://aquarius.oceansciences.org/cgi/ed_act.htm?id=18).

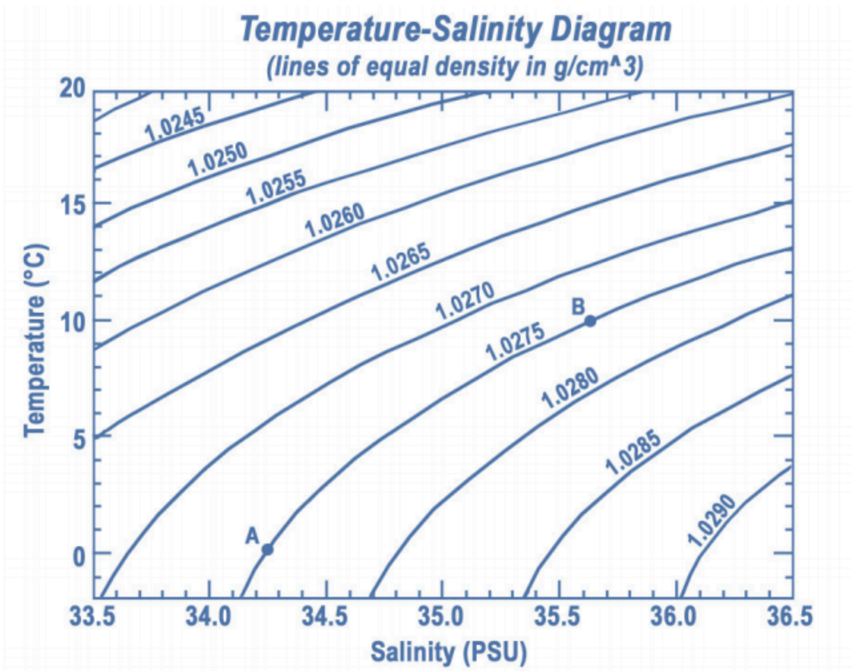

Figure1-4: A Temperature-Salinity Diagram from a NASA web page (https://aquarius.oceansciences.org/cgi/ed_act.htm?id=18).

1.2 Observation of sea level

Conventional technique with long observing history for the measurement of SSH change is tide gauge. Since 1970’s, various satellites have been used to observe SSH. In this section, I review methods to observe SSH using (https://www.climate.gov/news-features/climate-tech/reading-between-tides-200-years-measuring-global-sea-level).

1.2.1 Tide gauge

Attempt to measure SSH with a tide gauge started in 16-17th century. The SSH data in Amsterdam originate from 1700. At first, oceanographers recorded sea level relative to a point fixed to the land to measure SSH changes. This method was used only for episodic observation. Next innovation was to use a paper drum rotating at a constant rate by using clock springs. Like seismometers, pen attached by float moves up and down with ocean tides, and continuous tide records remain on paper attached to the rotating drum. (Figure1-5). This has been a standard way to measure SSH by tide gauges. Currently, we observe SSH change in a more accurate and easier way by using sound wave and microwave.

Figure1-5: Picture of an old tide gauge using a rotating paper drum for continuous recording.

1.2.2 Satellite altimetry

There are problems in the SSH observation with tide gauges. For example, there is serious difference in the density of observatories between Europe (high) and Africa (low). Furthermore, tide gauges can measure SSH only along the coast, and cannot measure SSH at centers of oceans. Considering these problems, people tried to use satellites for SSH observations. Here, I describe the principle and the history of ocean altimetry with satellites according to Ichikawa (2014) and the website of Archiving, Validation, and Interpretation of Satellite Oceanographic (AVISO).

An altimeter measures the SSH by using a microwave pulse. Satellite emits a pulse to sea surface and measures time for the pulse to travel from the satellite to the sea surface and from the sea surface to the satellite after being reflected at the sea surface. From this two-way ranging, we calculate the distance between the sea surface and the satellite. Together with the information on the satellite orbit, we can calculate SSH. Finally, dynamic change in SSH can be calculated by subtracting short-wavelength undulations coming from geoid and short-period fluctuation by ocean tide (Figure1-6). The precision of the orbit is an important factor in this method.

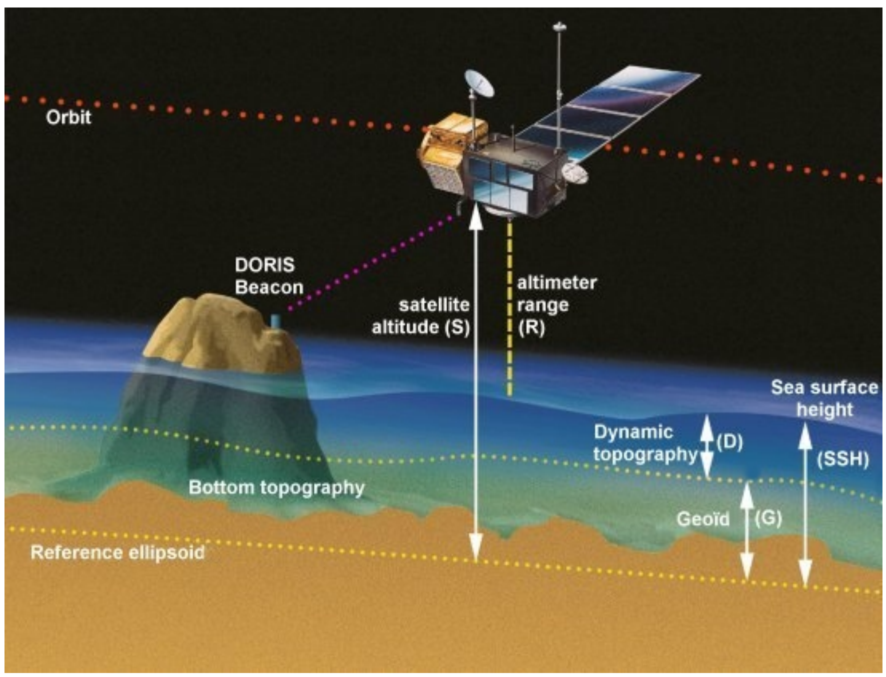

Figure1-6: Concept of ocean altimetry with satellites.

Attempt to measure SSH with satellite started in 1970s, with satellites GEOS-3 and Seasat launched by USA. They could observe variability of ocean bottom topography in terms of the geoid undulation, which reach several meters. However, the orbit error was 6-10 times larger than the natural temporal variability of SSH (~10cm), and these satellites were not suitable for studying SSH changes. (Figure1-7)

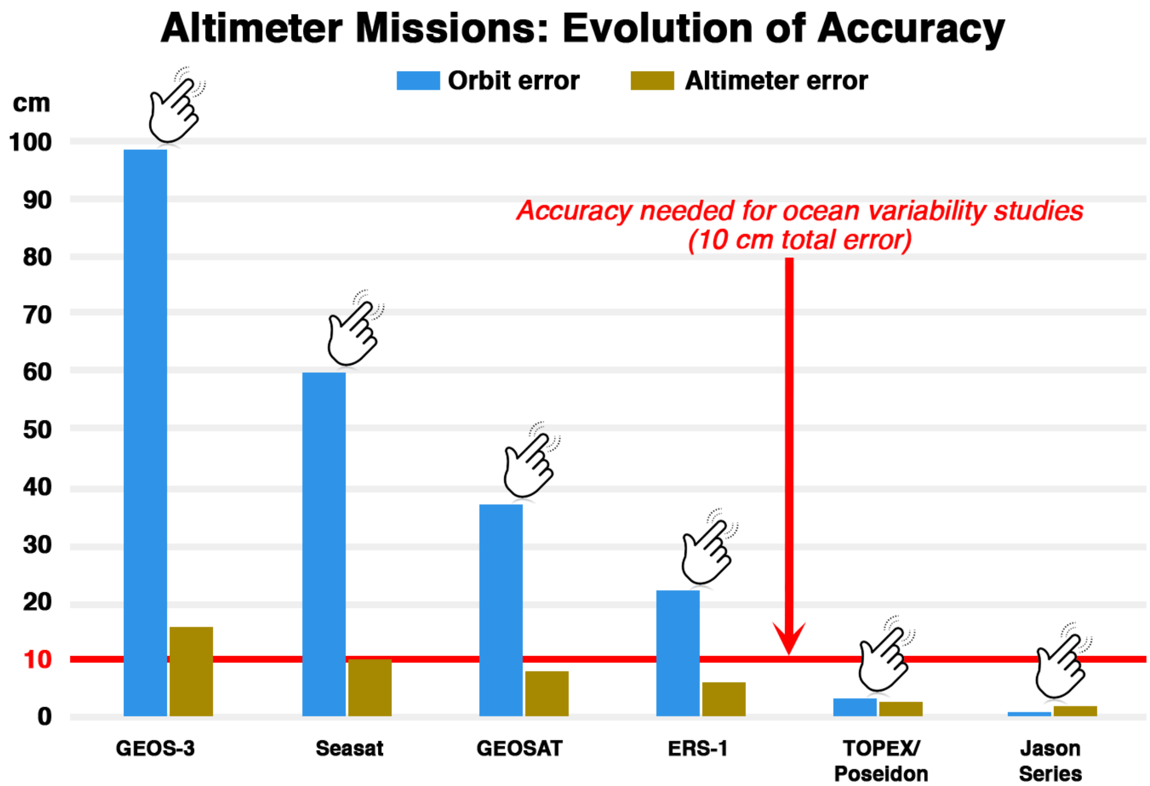

Figure1-7: Improvement of errors in satellite altimetry for different satellites 1970-2015 (Ichikawa et al., 2014)

In 1986, Exact Repeated Mission (ERM) started with GEOSAT by US Navy. ERM is an attempt to reduce orbital determination error by fixing satellite's orbit and cycle (17 orbital motions per day cycle, and ~150 km spacing of adjacent orbit tracks). In ERM, the error of altimeter is reduced by half. After this success, satellite altimetry has employed ERM. However, the error was still about 3 times as large as the natural temporal SSH variability.

In 1992, TOPEX/Poseidon (T/P) by CNES (Centre national d'études spatiales) and NASA (National Aeronautics and Space Administration) was launched. T/P employed many new methods to reduce errors. Its altitude was designed higher than conventional altimetry satellites to reduce influence from complicated Earth's gravity field. To reduce error by ionospheric delay of microwave signals, T/P used altimeter with 2 frequency bands, in Ku and C bands. ERM of T/P was designed to avoid aliasing with major tidal constituents. These attempts worked successfully, T/P's orbit errors have greatly reduced to 2-3cm, and we could observe various types of SSH changes in the ocean.

Figure1-8: Images of satellite altimeters.

A major problem with T/P was its spatial/temporal resolution (10-day and 300 km in mid-latitude). Regarding the satellite altimetry in general, we can only see directly below of satellite and it is not easy to improve both spatial and temporal resolution. Then, the next step should be observation by multiple satellites with various orbits. By doing so, we get satellites with different orbital cycles and orbital heights, and we can get data with improved temporal/spatial resolution as a whole. Figure1-9 shows the timeline of satellite altimetry. Various countries and groups have launched satellites with ocean altimeters and spatial and temporal resolution have been significantly improved.

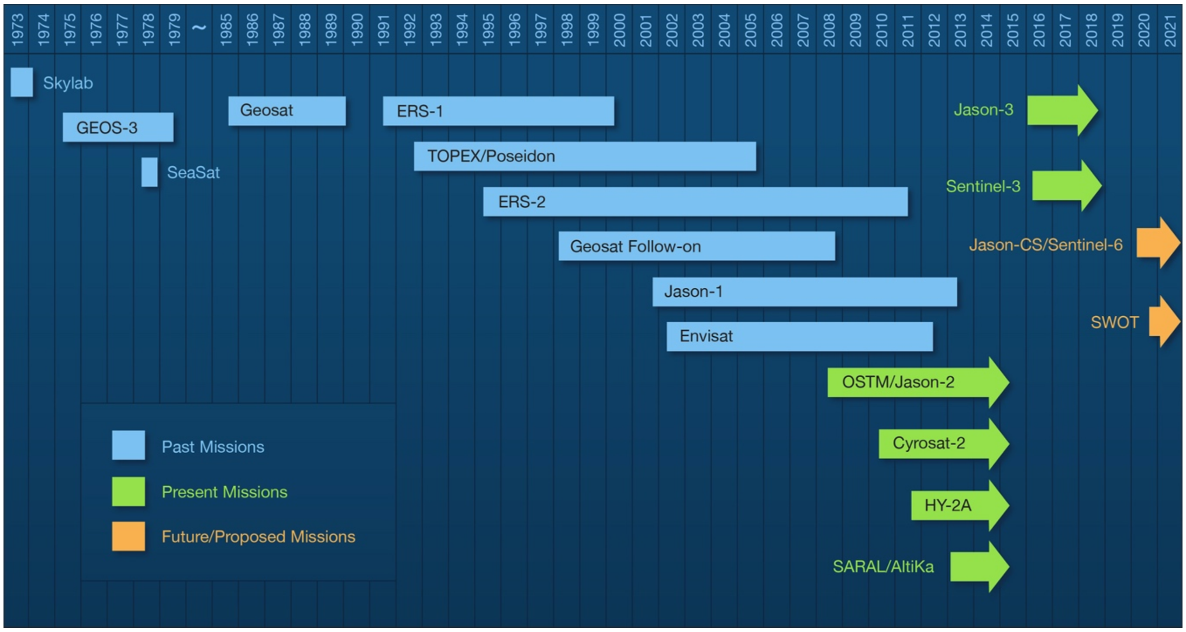

Picture1-9: Ocean altimetry with satellites of past and future (NASA webpage).

A new altimetry satellite SWOT (Surface Water and Ocean Topography) is scheduled for launch in 2021. The SWOT satellite uses Ka-Band microwave pulse. Conventional Ku and C bands radars can observe SSH without being affected by the weather. However, performance of these bands deteriorates near land because of interference from objects other than water surface. On the other hand, a Ka-Band radar can make narrowed pulse and achieve high accuracy even near lands. Furthermore, SWOT is equipped with SAR (Synthetic Aperture Radar) as well as ocean altimeter. By using these sensors simultaneously, we will be able to observe land water and near-shore ocean with a higher accuracy.

After the launch of T/P, high accuracy SSH data have been used for various purposes. Regarding SSH and its change, many important studies have been done based on T/P data [e.g. Cazenave, 2018; Nerem et al., 2018].

1.3 Satellite gravimetry

On the surface, we observe gravity using two major ways, (1) Absolute gravimetry by using falling objects in vacuum, (2) Relative gravimetry with springs. Although these observations offer highly accurate gravity data, they represent only point measurements and vast areas remained without any gravity measurements.

Satellite gravimetry was done for the first time using the Sputnik satellite launched in 1957 from the Soviet Union by observing the secular change of the Keplerian elements over time. In 1970s, satellites equipped with many corner-cube-reflectors (CCR) were launched. We can observe gravity field in high accuracy by performing Satellite Laser Ranging (SLR) to these satellites. SLR is the technology to measure the accurate distance between satellites and ground laser stations with 2-way travel times of laser pulses. By observing small perturbations on the Keplerian elements, we can recover the global gravity field. However, SLR has problems. Due to high satellite altitude (over 6000km) and low spatial density of ground stations, we could attain only a few thousands kilometer spatial resolution in gravity field. Imbalance of the station locations and weather-dependence of the SLR observations are also the problem. In other words, SLR is useful for only long-wavelength (low degree-order) components, and not suitable for measurements of short-wavelength components.

Figure1-10: Picture of a typical SLR satellite, equipped with many CCRs.

In 2000, CHAllenging Minisatellite Payload (CHAMP) was launched by Germany. CHAMP (low orbit) was tracked by GNSS satellites (high orbit), and this technique is called H-L SST (High-Low Satellite-to-Satellite Tracking). By CHAMP, Spatial and temporal resolution of our knowledge of the Earth’s gravity field improved, and we could see global distribution of the short-wave components of the gravity field with uniform accuracy.

H-L SST was successful to improve drawbacks of SLR. However, orbit accuracy of CHAMP was lower than SLR satellites due to several factors including atmospheric delay of radio wave signals. To further improve orbital accuracy, the

Gravity Recovery and Climate Experiment (GRACE) satellite system was launched by USA and Germany in 2002 (Figure1-11). GRACE uses L-L SST (Low-Low Satellite to Satellite Tracking). L-L SST is the method to use 2 satellites in the same low orbit and track each other, measuring their range, range rate, and range acceleration between the two satellites. The GRACE twin satellites (GRACE-A and GRACE-B) orbit approximately 250 km away on the same orbit at about 500 km altitude. They have K-Band Ranging (KBR) instruments and use them to measure between-satellite distances by microwave in 2 different frequencies in K band. In this paper, I use the GRACE data and explain the detail in Chapter 2. In 2016, GRACE finished their mission. There was a period without time-variable gravity data until the GRACE Follow-Om (GRACE-FO) was launched in 2018.

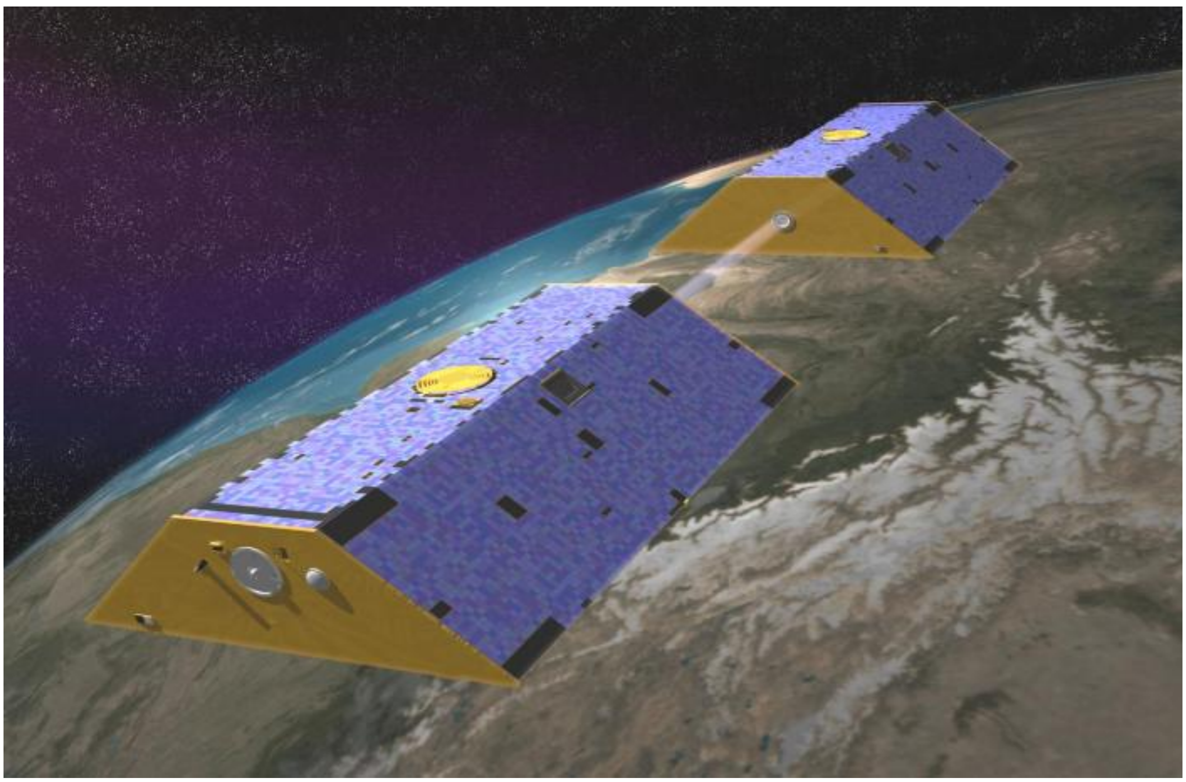

Figure1-11: Conceptual figure of GRACE. One of the satellites chase another satellite in the same orbit, in a style similar to the famous animation “Tom and Jelly”.

GRACE enabled us to study time-variable gravity in a global scale. Gravity changes due to various reasons especially on land. For example, declining mountain glaciers in Himalaya [Matsuo and Heki., 2010; 2014] and in Antarctic Islands [Matsuo and Heki, 2013], coseismic change of gravity [Heki and Matsuo, 2010; Matsuo and Heki, 2011; Tanaka et al., 2015], postseismic gravity change [Ogawa and Heki, 2007; Tanaka and Heki, 2014], change in continental water storage [Castle et al., 2014; Reager et al., 2016] and interannual change in soil moisture due to climate changes [Morishita and Heki., 2008; Fasullo et al., 2013]. In the ocean, many researchers try to study mass changes in oceans in various spatial scales using the sea level budget approach, i.e. testing the consistency among three quantities, time-variable gravity, SSH changes by altimetry, and steric changes by measurements with Argo Floats [Feng and Zhong., 2015; Chambers et al., 2017; Rietbroek et al., 2016; Yi et al., 2017].

In 2009, European Space Agency (ESA) launched the Gravity field and steady-state Ocean Circulation Explorer (GOCE) satellite (Figure1-12). GOCE had an onboard gravity gradiometer, an equipment measuring spatial derivative of gravity, and its orbital height was ~300km. GOCE aimed to improve the stationary short-wavelength components in the Earth's gravity model. GOCE finished its mission in 2013, and the improved geoid model contributed to isolate dynamic SSH due to ocean current. The GOCE data are not suitable for studying time-variable gravity field, and I do not discuss the GOCE data in this thesis.

Figure1-12: Image of the GOCE satellite with gravity gradiometer, launched by ESA in 2007. This satellite contributed to improve short-wavelength components of the Earth's static gravity field.

1.4 GNSS (Global Navigation Satellite System)

Global Navigation Satellite System (GNSS) is a general term for satellite positioning systems launched by various countries including Japan. GPS (Global Positioning System) launched by USA has long been an only GNSS, but several other countries have developed their own satellite systems, so the name GNSS came to be used. New GNSS include GLONASS (GLOBAL'naya Navigatsionnaya Sputnikovaya Sistema) by Russia, Galileo by EU, BeiDou by China, and QZSS (Quasi Zenith Satellite System) by Japan. Using multiple GNSS, we can get high accuracy positioning data. In this section, I introduce some features of GPS and of many other GNSS.

GPS is a system of satellite technique to determine 3-dimensional position of a ground station by receiving microwave signals from multiple satellites simultaneously. For the positioning, there are 2 main analysis methods: (1) single point positioning, and (2) relative positioning. In the single point positioning, they determine the absolute position of the receiving station. In the single point positioning, they use pseudo-range information to determine the approximate position of an object that is stationary or moving on the surface of the Earth. In the relative positioning, we determine the relative position of a station with respect to a reference station using carrier phases of the microwave signals. This method is used to determine the precise position and velocity of a stationary station.

About 30 GPS satellites are deployed at altitude of 20,000km on 6 orbital planes, with separation of 60 degrees in the ascending node. This makes it possible to determine positions of any ground points by observing 4 or more satellites. (Figure1-13)

Figure1-13: Image of GPS satellites deployed in 6 orbital planes.

Satellites send microwave signals in 2 different frequencies in L band which are phase modulated using two different kinds of codes (P code and C/A code). At the stations, receiver calculate times for the microwave signal to travel from satellites to the station discriminating signals from different satellite by their codes. In the single point positioning, the distance between satellite and stations can be calculated by multiplying the propagation time by the light speed. Such a distance is called pseudo-range because it has a bias coming from clock synchronization errors. By using four or more pseudo-ranges, we can determine three components of the satellite position and the clock bias. In the relative positioning, we make double differences of carrier phases received from different satellites at different stations. By doing this, we can cancel phase errors coming from the fluctuations of satellite and station clocks. Because phase measurement always suffers from integer ambiguities, we have to obtain continuous phase measurements over a long time to separate such ambiguities from relative positions of stations.

GNSS is a major tool to study crustal movements, e.g. plate motions, coseismic crustal movements, postseismic transients [e.g. Heki and Mitsui., 2013], displacement by surface loads [e.g. Argus et al., 2017], and slow slip events [e.g. Tu and Heki., 2017]. There are many other studies in such fields done using GNSS.

1.5 Climate changes

1.5.1 ENSO

ENSO is a term that signifies two different phenomena: El Niño and Southern Oscillation. Originally, El Niño meant a rise of seawater temperature due to weakening of upwelling of cold water from depth. Such an increased seawater temperature episode occurs once in a few years. Researches in 1970s found that the area of high seawater temperature extends from Peru to large area of equatorial Pacific Ocean and called such episode as El Niño. In this paper, we use the word El Niño to indicate the latter phenomenon. The opposite phenomenon that negative seawater temperature anomaly extends from Peru to the Pacific Ocean is called La Niña (Figure1-14). Furthermore, the period when neither El Niño nor La Nina occur is called La Nada.

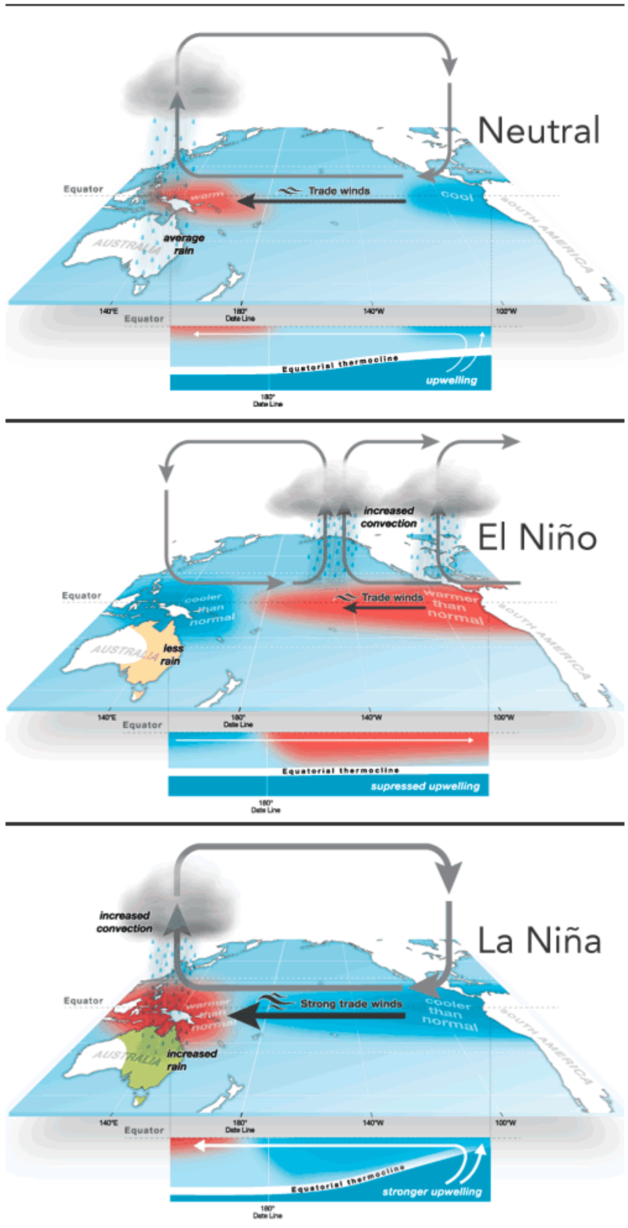

Figure1-14: Comparison of the normal status (top), El Niño (middle) and La Niña (bottom) by Bureau of Meteorology, Australia. There climate changes, originally named for SST changes off Peru, bring various changes in precipitation, wind and temperature worldwide.

Southern Oscillation is a seesaw-like fluctuation of sea surface pressure between eastern (Tahiti) and western (Indonesia and Australia) parts of the South Pacific Ocean. Southern Oscillation usually occur together with El Niño (La Niña), and the two phenomena are called together as ENSO.

There are no internationally-agreed rigorous definition of El Niño and La Niña. Each country has its own definition. Japan Meteorological Agency (JMA) defines El Niño monitoring the sea surface temperature (SST) within area 5°N-5°S and 90°W-150°W (NINO.3 area). JMA call it El Niño when 5-month moving average of the SST in NINO.3 exceed the average monthly SST over the last 30 years by 0.5 degrees for more than 6 consecutive months. La Niña is defined in a similar manner with −0.5 degrees as the threshold. In this study, I call this index "D-SST" and employ the definition of El Niño and La Niña by JMA (https://www.data.jma.go.jp/gmd/cpd/db/elnino/index/dattab.html).

In the last 25 years, El Niño has occurred in 1997 spring - 1998 spring, 2002 summer -early 2003, 2009 summer -2010 spring, 2014 summer - 2016 spring, and 2018 autumn – 2019 spring. On the other hand, La Niña occurred in 1995 summer -early 1996, 1998 summer - 2000 spring, 2005 autumn - spring 2006, 2007 spring - 2008 spring, 2010 summer - 2011 spring, and 2017 autumn - 2018 spring.

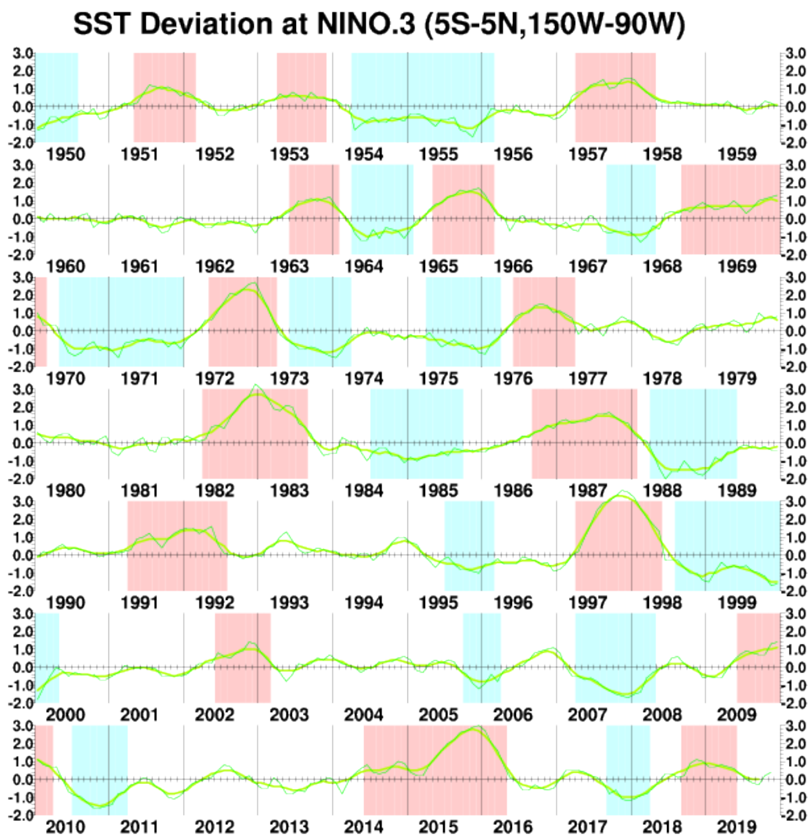

Figure1-15: Change of D-SST from 1950. Red and blue shading represents El Niño and La Niña, respectively.

When El Niño or La Niña occur, strength of the trade wind and area of precipitation change in the equatorial Pacific Ocean. As a well-known change, it rains more than usual in coastal desert in Peru. On the other hand, precipitation decreases in Indonesia and Papua New Guinea because center of precipitation in equatorial Pacific Ocean moves eastward. Such rainfall anomalies occur not only in the Pacific Ocean but also tropical and midlatitude area all over the world. These simultaneous occurrences of climate change in various area of the world is called “teleconnection”. (Figure1-16)

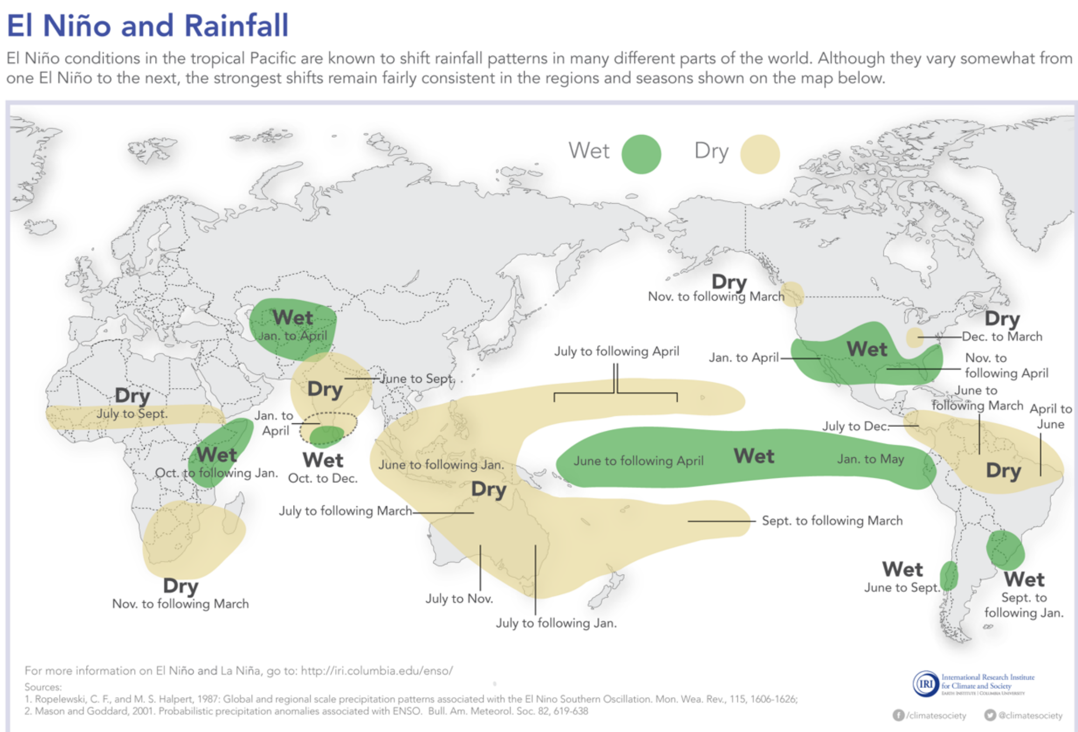

Figure1-16: Areas where precipitation is influenced by in El Niño and La Niña by IRI (International Research Institute of Climate and Society). In green/yellow areas, El Niño brings more/less precipitation and less/more in La Niña.

The rainfall anomaly caused by ENSO has influence to GMSL. Fasullo et al (2013) reported that multiple climate changes including the 2010-2011 La Niña episode caused large amount of rain in Australia. Because of small runoff from the Australian desert, groundwater increased there and made GMSL drop during that period.

1.5.2 IOD

Indian Ocean Dipole (IOD) is an atmosphere-ocean interaction phenomenon in the Indian Ocean. Name “IOD” comes from the fact that the values of sea temperature, precipitation, sea level changes, etc., behave like a dipole in the eastern and western parts of the equatorial Indian Ocean region.

In a positive IOD, seawater temperature gets higher than normal near the African coast and lower around Indonesia. Negative IOD causes the opposite phenomenon and often occur before and after a positive IOD. (Figure1-17)

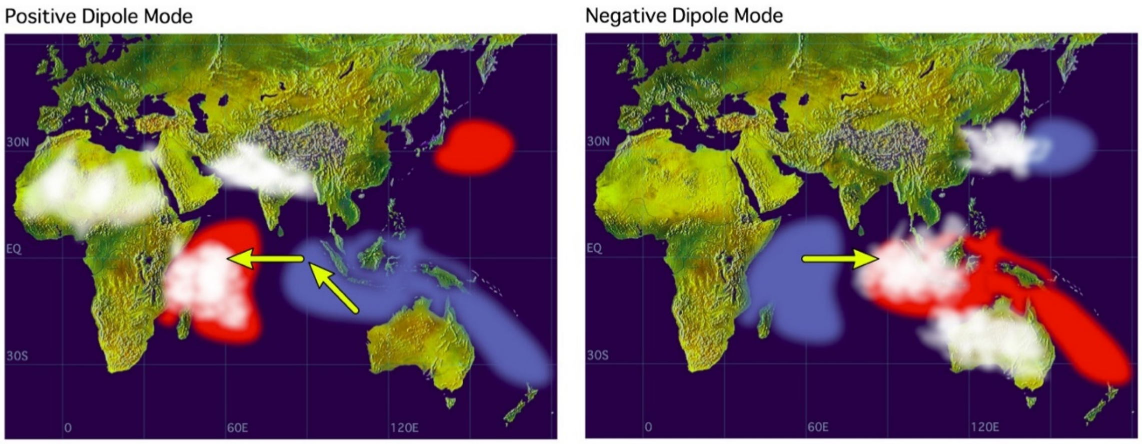

Figure1-17: Conceptual figure of positive (left) and negative (right) IOD. The red and blue ocean areas show the region with the positive and negative seawater temperature anomalies, respectively. The arrows indicate the marine wind that becomes stronger associated with the IOD occurrences. The clouds indicate areas of increased amount of precipitation.

IOD is known to influence a wide range of weather conditions, including forest fires in Africa and heavy rains in and around Japan, far away from the Indian Ocean. IOD is an independent phenomenon from ENSO, and even when El Niño and La Niña do not occur, IOD-type seawater temperature anomalies may appear.

It is known that changes in ocean currents due to changes in equatorial jets and offshore winds in the Indian Ocean significantly contribute to the occurrence of IODs. Dipole Mode Index (DMI), an index for IOD, is calculated from the SST gradient anomaly between eastern (E50°-E70° and S10°-N10°) and western (E90°-E110° and S10°-N10°) equatorial Indian Ocean. In this paper, we use DMI available from http://www.jamstec.go.jp/aplinfo/sintexf/e/index.html.

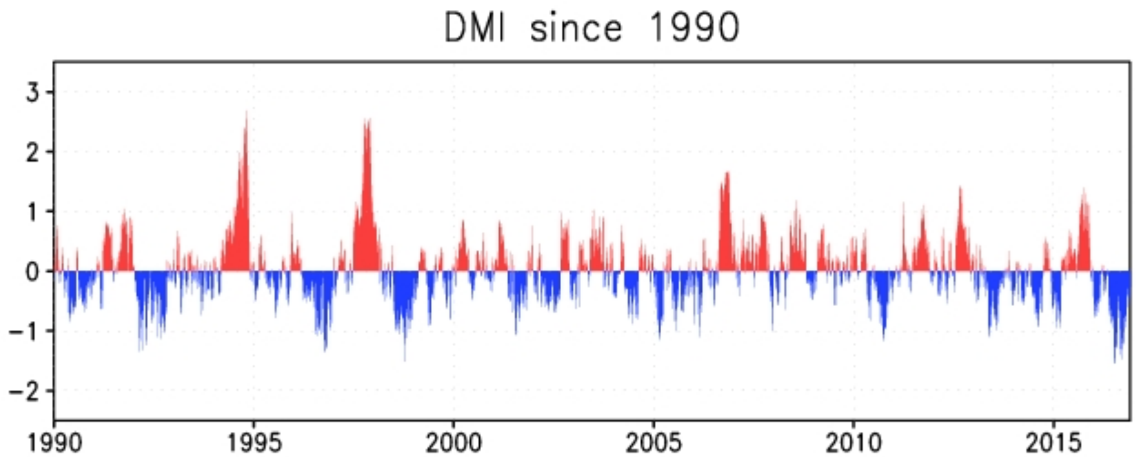

Figure1-18: DMI change from 1990.

1.6 Satellite observations in shallow coastal seas

As mentioned in Section 1.2 and 1.3, satellite observations in coastal area has some difficulties. Altimeter data are less accurate in coastal areas and GRACE data often have “leakage” near land-ocean boundaries (see Section 2.1).

These problems arise from the observing systems of satellites. An example is the ocean tide model. Generally, in shallow seas, ocean tide models have more uncertainties. Figure1-19 shows the standard deviations for M2 and K1 tides from 7 modern data-constrained models by Stammer et al (2014). We can see the models are less accurate in shallow sea areas. Such an error seriously influences the output of altimeter and GRACE data. This is the reason why we need data other than satellites for sea surface heights and ocean mass changes.

Wind and complicated seafloor topography are dominant factors responsible for tidal model errors. In the coastal region, wind has a large influence on sea level changes. Bulk equation of sea level rise H by wind stress is shown below.

$$\frac{dH}{dx} = \frac{\tau}{\rho h g} \tag{1-1}$$

where x is the horizontal distance along the wind blowing direction, ρ is the density of the water, h is the water depth, g is the gravity acceleration and τ is the wind stress over the unit sea surface area computed by bulk equation (1-2).

$$\begin{aligned} \tau_x &= \rho_a C_D u\left(u^2+v^2\right)^{1/2} \\ \tau_y &= \rho_a C_D v(u^2+v^2)^{1/2} \end{aligned} \tag{1-2}$$

Here, ρ_a is the density of the air ($\rho_a = 1.20 \times 10^{-3} g\ cm^{-3}$), C_D is the exchange coefficient for momentum, u and v are the eastward and northward components of wind velocity. SSH height H can computed by integrating the equation (1-1) along the wind direction.

As seen in equation (1-1), water depth is an important factor to change SSH by wind stress. Considering these points, in-situ observation methods other than satellites are needed to study SSH and mass changes in the shallow regions near the coastline.

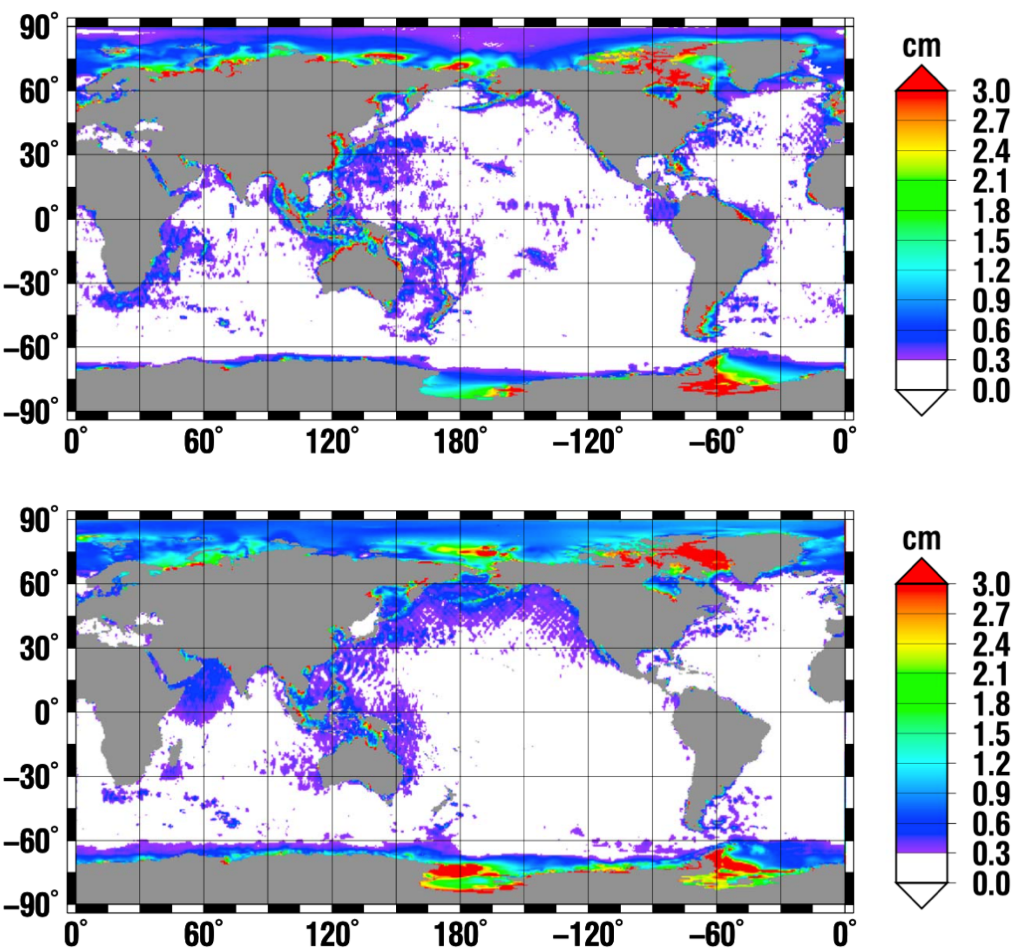

Figure1-19: Standard deviations for M2 and K1 tidal constituents from 7 modern data-constrained ocean tide models (Stammer et al., 2014).

1.7 Scope of this study

In this paper I try to study SSH changes in oceans where wind plays a major role in SSH changes using multiple observation data as reviewed in previous sections. I evaluate the difference in data from different observational techniques. To cover insufficient accuracy of satellite altimetry and satellite gravimetry, I use data of GNSS and tide gauge. To interpret crustal movements measured with GNSS, I model the surface displacement caused by load.

By comparing satellite data with in-situ observation data, I discuss accuracy of satellite observations and model SSH change in terms of mass changes and thermal expansion of seawater. In some areas, climate changes such as ENSO and IOD have a large influence on SSH. So, I evaluate the influence of climate changes using the Empirical Orthogonal Function (EOF) analysis technique.

1.8 Research areas and previous studies

This paper consists of 5 sections. Section 2 shows data used in this study and methods of numerical analysis. In Section 3, I describe the results. Geophysical discussion on the results is given in Section 4, and I give conclusions in Section 5. Below, I describe regions I studied.

1.8.1 Gulf of Carpentaria

The Gulf of Carpentaria (GOC) is located to the north of Australia. GOC is surrounded on 3 sides by the Australian continent and the northern side is open to the Arafura Sea. The total area of GOC is approximately 300,000 km^2. GOC is relatively shallow, with the maximum is 82 m, and the average depth of the central region is 55-66 m (Figure1-20). GOC has one of the largest seasonal SSH change in the world according to the altimeter data (Figure1-21).

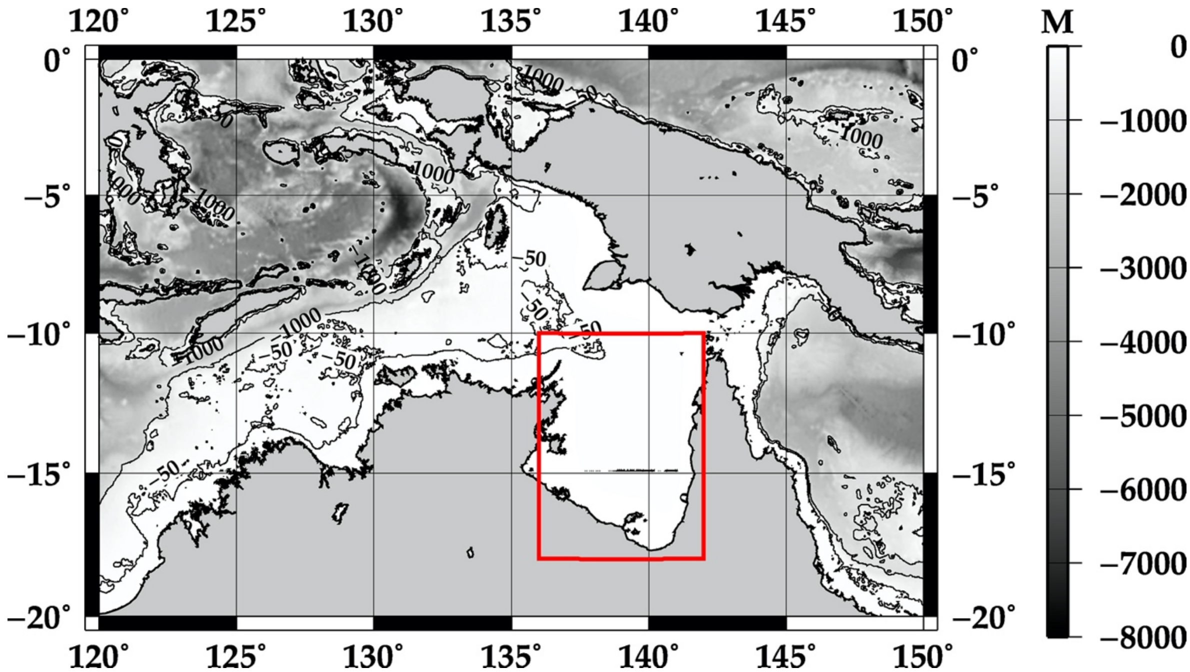

Figure1-20 Bathymetry in and around GOC (red square).

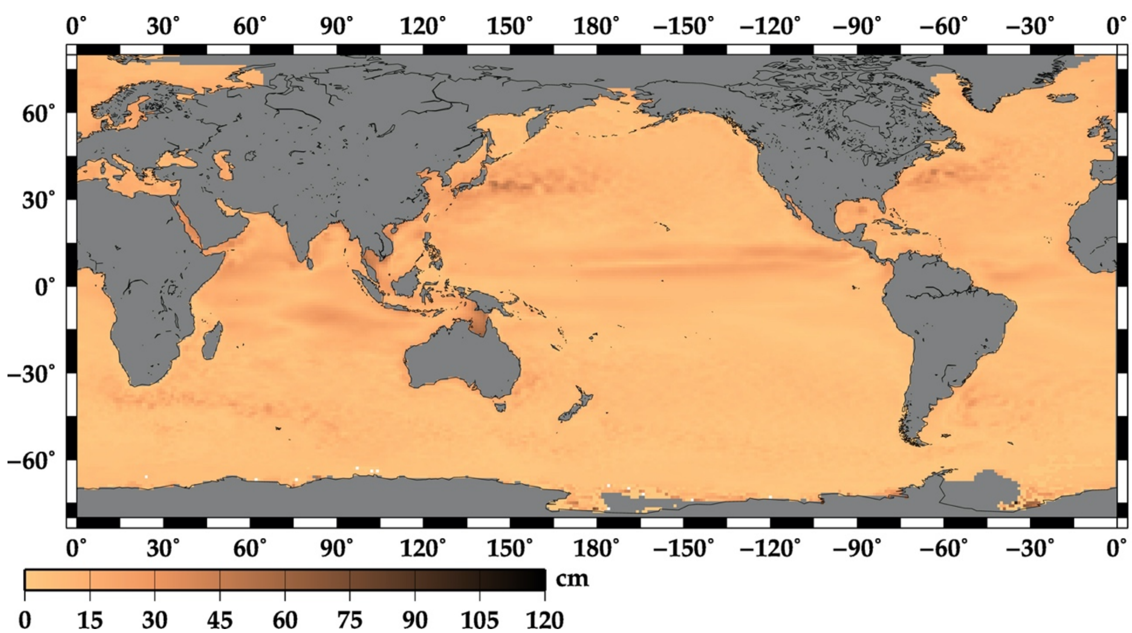

Figure1-21 Amplitude of annual change of SSH (cm) by satellite altimeter measurements (1993-2018).

From now, we introduce several past studies about SSH in GOC and other ocean areas to the north of Australia. Forbes and Church (1983) reported the annual SSH change in GOC, with the maximum height of 75cm in the south-east corner, by observation of satellite-tracked drogued buoys. They suggested that its 70% is explained by winds, atmospheric pressure changes, and steric variations. Tregoning et al (2008) found there are good correlation (r=0.93) between the tide gauge data and the GRACE time-variable gravity. Amplitude of seasonal change is ~40cm.

Oliver and Thompson (2011) showed that the intra-seasonal change in GOC is driven by wind by using a barotropic circulation model. They also show Madden-Julian Oscillation (MJO) is a significant contributing factor to inter-annual changes of SSH in north of Australia. Wang et al (2016) compared annual SSH changes from altimeters and GRACE. They found that the inter-annual SSH change is related to other large-scale climate changes such as ENSO and Pacific Decadal Oscillation (PDO). Gharineiat and Deng (2018) showed that there are also good correlations between tide gauge and altimeter data. They also showed that, in the northern Australian coast, inter-annual changes of altimeter data are also correlated with ENSO by EOF analyses of the altimeter data.

In fact, the ocean tide model has a high uncertainty in this area (Stammer et al., 2014). So, we need to use other observational methods than satellite which are not influenced by tide models and understand the data from multiple perspectives. As an example, Alothman et al (2020) compared vertical and horizontal displacements observed by GNSS and gravity changes by GRACE in the Red Sea and found consistent phases in their seasonal changes. They, however, concluded that there is not enough accuracy of hydrological model for the full comparison with the GNSS data.

In this work, we also apply the EOF analysis to the GRACE data to find how annual and inter-annual changes occur. Furthermore, we use the GNSS data as those not influenced by tide models and perform numerical calculations of surface displacement to compare the in-situ and satellite observations.

1.8.2 Gulf of Thailand

Gulf of Thailand (GOT) is located to the west of the South China Sea. GOT is surrounded by Thailand, Cambodia and Vietnam and continues to the South China Sea to the southeastern side. GOT is as large as ~320,000km^2. It is shallow, with the maximum and average depths of ~85 m and ~58m, respectively (Figure.1-24). Satellite altimetry also shows that large seasonal change in SSH occur in GOT (Figure.1-21).

Wouters and Chambers (2009) suggested that the GRACE data show the same secular trends as altimeters and tide gauges, although the GRACE data is 30% less than the altimeter data. and concluded that sea level rise of 5 mm/year occurs there from the average of the data from tide gauges in GOT.

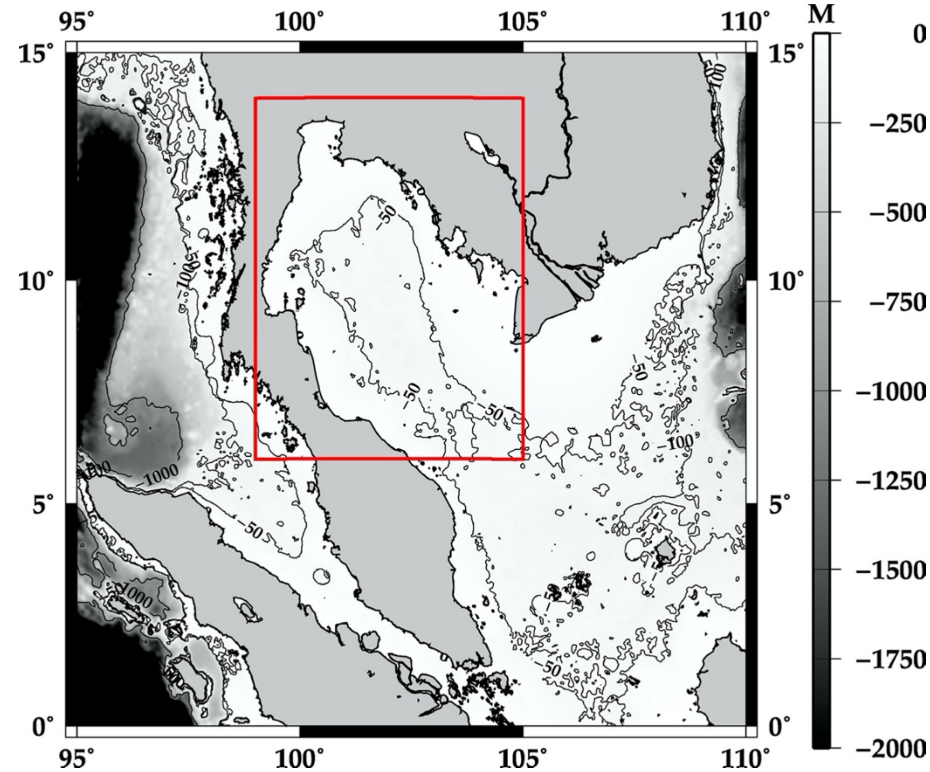

Figure1-22: Bathymetry of GOT (red square).

Chapter2 Data and method

2.1 GRACE data

In this section, I will explain several different solutions of the GRACE gravity model. There are three official GRACE data centers: (1) Center for Space Research (CSR), University of Texas at Austin, USA, (2) NASA Jet Propulsion Laboratory (JPL), USA, and (3) Geoforschungs Zentrum (GFZ), Potsdam, Germany. We can download the results made available by these data centers from PO.DAAC (https://podaac.jpl.nasa.gov). For the Level-2 data, we can use the release-06 (RL06) data as the latest one. In this paper, I use two kinds of solutions, those made of the Stokes' coefficients of spherical harmonics (SH) and the mascon solution. First, I describe common features in the two solutions.

As described in Chapter1-3, the GRACE satellite system directly observes the distance change between the twin satellites. Data related to orbit information are called Level-1A and are not open to the public. They convert these data to the changing rates and the acceleration of the distance between the two satellites. This data set is called the Level-1B data, which are publicly available. This data set is supposed to be used only by technical experts. For general researchers, it is difficult to use the Level-1B data because further processing is needed to obtain information on gravity changes. From here, two types of data, easier to use than Level-1B, will be described.

2.1.1 SH (spherical harmonics) solution

GRACE Level-2 data are given as monthly sets of the (Stokes') coefficients of spherical harmonic. The three analysis centers use sophisticated models of atmosphere and ocean to remove signals arising from these factors apply to finalize the Level-2 data. Because we need some knowledge on spherical harmonics to use the Level-2 data, the analysis centers also provide data composed of gravity values at grid points, called the Level-3 data. Level-3 data is the easiest to use. However, they use several kinds of filters to make the Level-3 data. If researchers are not happy in using models that they are not familiar with, they should analyze the Level-2 data.

In the Level-2 data, we can make various components of the static gravity field, i.e., vertical, north-southward and east-west, using equations given in many textbooks e.g. Kaula [1966], Heiskanen and Moritz [1967], and Wang et al. [2012a]. They can be expressed as below.

$$G_r(h,\theta,\varphi) = -\frac{GM}{R^2}\sum_{n=2}^{nmax}(n+1)\left(\frac{R}{R+h}\right)^{n+2}\sum_{m=0}^{n}(C_{nm}\cos m\varphi + S_{nm}\sin m\varphi)P_n^m(\sin\theta) \tag{2-1}$$

$$G_\theta(h,\theta,\varphi) = -\frac{GM}{R}\sum_{n=2}^{nmax}\left(\frac{R}{R+h}\right)^{n+1}\sum_{m=0}^{n}(C_{nm}\cos m\varphi + S_{nm}\sin m\varphi)\frac{dP_n^m(\sin\theta)}{d\theta} \qquad (2\text{-}2)$$

$$G_\emptyset(h,\theta,\varphi) = -\frac{GM}{R^3}\sum_{n=2}^{nmax}(n+1)(n+2)\left(\frac{R}{R+h}\right)^{n+3}\sum_{m=0}^{n}(C_{nm}\cos m\varphi + S_{nm}\sin m\varphi)P_n^m(\sin\theta) \qquad (2\text{-}3)$$

where θ and φ are colatitudes and longitudes, respectively, G is the universal gravity constant, M is the mass of the earth, R is the earth's equatorial radius, h is the height of the observation point from the earth's surface, P_n^m is the n-th degree and m-th order fully-normalized associated Legendre function.

In real cases, we do not apply these formulae directly. The C_{20} term represents the equatorial bulge and is dominant in the non-uniform part of the gravity field. Satellite Laser Ranging (SLR) provides more accurate measurement values of this component because SLR satellites fly in higher orbits than GRACE and are more suitable to measure the long-wavelength gravity components such as the C_{20} component. Therefore, when using the Level-2 data, it is necessary to replace the C_{20} term with those observed by SLR.

In addition, suppression of systematic errors in GRACE data is necessary. The GRACE satellites are flying at altitude ~500 km. As described in Chapter 1, the spatial resolution of gravity satellites is inversely proportional to the orbital altitude of the satellites. Since the spatial resolution in GRACE is ~300km, the short wavelength components are noisy.

Furthermore, GRACE satellites adopt polar orbits, the recovered gravity field tends to show north-south stripe patterns. This effect appears as in Figure2-1. There are strong north-south stripes reflecting the orbit direction. For these reasons, various filters, such as two-dimensional spatial Gaussian filter [Wahr et al.,1998], de-striping filter [Swenson and Wahr., 2006] are applied. We also use hydrological models to correct land water signatures to isolate what we want to study.

When using SH solution, I use the programs uploaded on the homepage of the Geodetic Society of Japan (http://www.geod.jpn.org/contents/book/program.html).

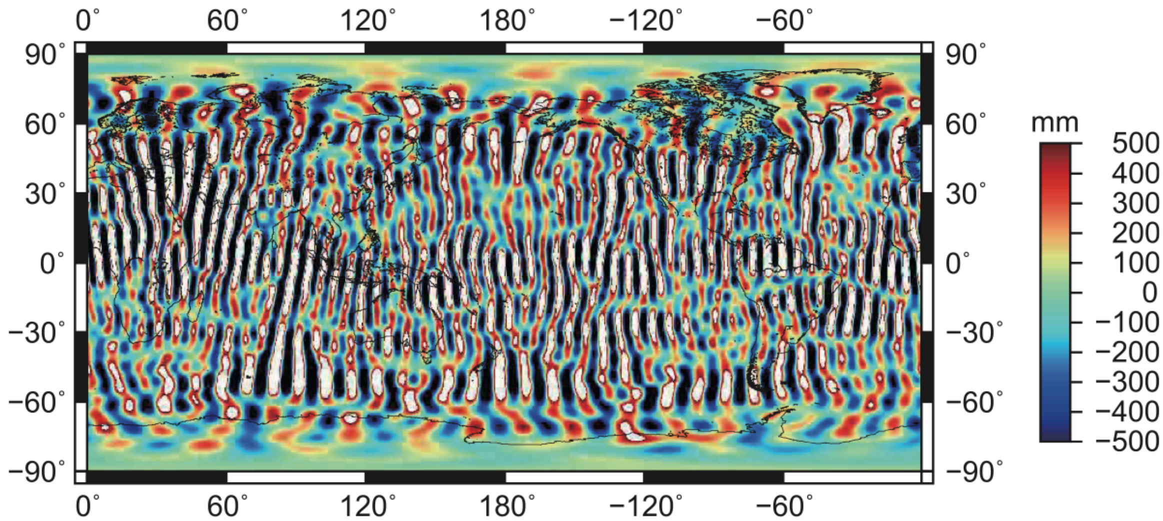

Figure2-1: An example of surface mass anomaly (in equivalent water thickness) derived from GRACE Level-2 data without any filters [Munekane., 2013].

2.1.2 Mascon solution

As described in Section 2.1.1, GRACE SH solutions have some problems, especially large noises in higher degree/order components and longitudinal stripes. Figure 2-2 shows the distribution of the secular trends of gravity during 2003-2016 based on the GRACE SH solutions. The leakage between land and ocean is clear there. For example, gravity decrease in SE Alaska and Patagonia reflects the decline of mountain glaciers. These changes do not occur in the ocean but are limited to the land area. Nevertheless, we see blue color leaking into the ocean. Such a leakage is a big problem in studying mass changes in ocean. Furthermore, some previous studies say that filters used to process the GRACE SH solutions may reduce the amount of the real geophysical signals [Landerer and Swenson, 2012].

The mass-concentration (mascon) solutions have become popular because they solve these problems in SH to some extent. These solutions are obtained by assuming that the mass anomalies occur in discrete mason blocks distributed over the earth's surface. Previous researches employed 3 approaches to derive the mascon solutions. First one is to use partial derivatives, with analytical expression, of inter-satellite range-rate measurements for individual mascon blocks. Second approach is to convert the spherical harmonics, truncated at a finite degree, derived from the range-rate or range-acceleration data to mass anomalies of mascon blocks. Third one is to fit SH solutions to mascon blocks. Because the third solution has to be derived after making GRACE SH solutions, its advantage over the SH solutions is not clear.

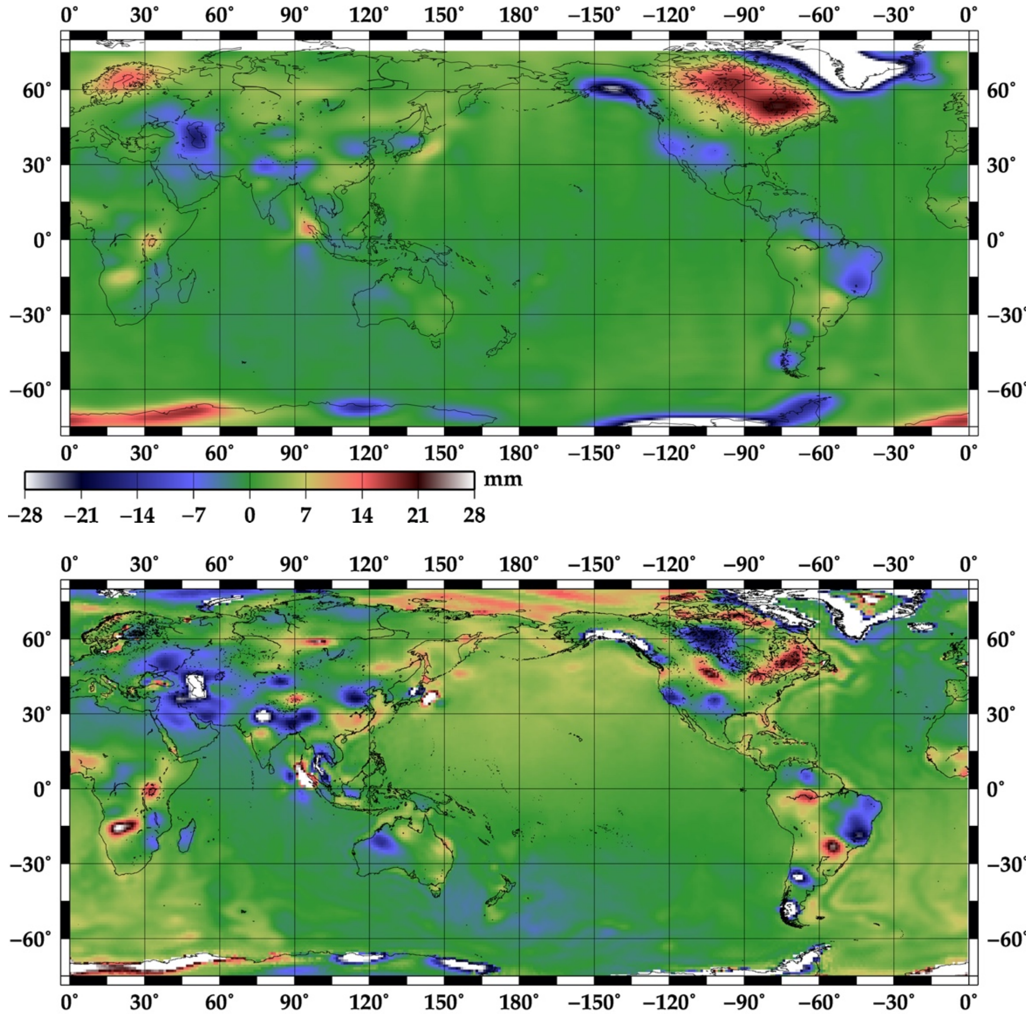

Figure2-2: Linear trend of gravity field in unit of water equivalent height (cm) drawn using the SH (top) and the mascon (bottom) solutions.

In this paper, I use the mascon solution provided by CSR, which was derived using the second approach. Here I give a brief description of the CSR mascon solutions according to Save et al. [2016]. The CSR mascon solutions have the following 3 characteristics. (1) They use only the observation data by the GRACE satellite system, (2) The regularization matrix constrains the mascon solution around the past models from GRACE without biases, and (3) The mascon blocks are assumed on grid points with separation of 1°.

The CSR mascon solution uses 40,950 hexagonal and 12 pentagonal tiles distributed at the geodetic grid proposed by Laven et al. [2010]. Reasons of using the geodetic grid is as follows, (1) to reduce differences in area between tiles in equatorial and polar regions, (2) to let tile boundaries coincide with coastline for easy reduction of land-ocean leakage. Mascon blocks can be represented by using spherical harmonics with degree/order complete to 120. In fact, it needs to be up to 179 to realize 1° grid globally, but they employed 120 for computational efficiency. When estimating mass anomalies at individual tiles, they used the Tikhonov regularization [Save et al., 2012]. In mascon solution, they employed the unit of equivalent water height in centimeter to facilitate later use.

To invert mass anomalies of individual mascon tiles, Save et al [2016] used the following procedures. The gravity potential at the satellite altitude can be expressed using Stokes' coefficients as follows.

$$U(r,\theta,\lambda) \approx \frac{GM}{R}\left[\sum_{l=0}^{l_{max}}\sum_{m=0}^{l}\left(\frac{R}{r}\right)^{l+1}\bar{P}_{lm}\sin(\theta)\left(\bar{C}_{lm}\cos(m\lambda)+\bar{S}_{lm}\sin(m\lambda)\right)\right] \quad (2\text{-}4)$$

where θ is latitude, λ is longitude, and r is the radius distance of the point where the geopotential is evaluated from geocenter; M and R are the mass and reference radius of the Earth; G is the universal gravitational constant; l and m represent the spherical harmonic degree and order; $\bar{C}_{lm}$ and $\bar{S}_{lm}$ are the fully normalized Stokes' coefficients and $\bar{P}_{lm}$ is the fully normalized associated Legendre functions. Rowlands et al. (2010) compute the change of the coefficients caused by a small mass caused by a uniform layer over a certain small region, which is a geodetic tile j in this study, as

$$\begin{aligned}\Delta\bar{C}_{jlm}(t) &= \frac{\sigma_j(t)\left(1+k_l'\right)R^2}{M(2l+1)}\int\bar{P}_{lm}(\sin\theta)\cos m\lambda d\Omega \\ \Delta\bar{S}_{jlm}(t) &= \frac{\sigma_j(t)\left(1+k_l'\right)R^2}{M(2l+1)}\int\bar{P}_{lm}(\sin\theta)\sin m\lambda d\Omega\end{aligned} \quad (2\text{-}5)$$

where the integrations are performed over the area included in geodetic tile j. ⍰ represents the area of tile j; the load Love number of degree l is represented by k_l' reflecting the Earth's elastic yielding. $\sigma_j(t)$, the mass of the layer over the geodetic tile j, is evaluated as $1025 \times h_j(t)$, where $1025\ \mathrm{kg/m^3}$ is the density of water and $h_j(t)$ represents the height of a uniform layer of water over the tile. The time t is the mean over a ~30 day time span. Here we drop the time tag because we here only discuss a snapshot of gravity field. So, we rewrite equation (2-5) to estimate h_j as below,

$$\Delta\bar{C}_{jlm}=h_j\left[\frac{10.25\left(1+k_l'\right)R^2}{M(2l+1)}\right]\int\bar{P}_{lm}(\sin\theta)\cos m\lambda d\Omega$$
$$\Delta\bar{S}_{jlm}=h_j\left[\frac{10.25\left(1+k_l'\right)R^2}{M(2l+1)}\right]\int\bar{P}_{lm}(\sin\theta)\sin m\lambda d\Omega \tag{2-6}$$

For the CSR mascon solution, one geodetic tile j has a dimension of ~1°. Integration in equation (2-6) is approximated with the product of the area and the value of the spherical harmonics which is assumed to be uniform over the geodetic tile j. $\bar{P}_{lm}(\sin\theta)\cos m\lambda$ is evaluated at the center of the tile and $d\Omega$ is approximated by the area A of the tile j. These assumption leads to the following equation:

$$\Delta\bar{C}_{jlm}=\left[\frac{10.25\left(1+k_l'\right)R^2}{M(2l+1)}\right]h_jA_j\bar{P}_{lm}\left(\sin\theta_j\right)\cos m\lambda_j$$
$$\Delta\bar{S}_{jlm}=\left[\frac{10.25\left(1+k_l'\right)R^2}{M(2l+1)}\right]h_jA_j\bar{P}_{lm}\left(\sin\theta_j\right)\sin m\lambda_j \tag{2-7}$$

where θ_j and λ are geocentric latitude and longitude of the center of jth tile. Total change of the geopotential coefficients $\Delta\bar{C}_{jlm}$ and $\Delta\bar{S}_{jlm}$., due to the change of the mass of all the 40,692 geodetic tiles, can be calculated as the sum of each $\Delta\bar{C}_{jlm}$ and $\Delta\bar{S}_{jlm}$.

$$\Delta\bar{C}_{lm}=\left[\frac{10.25\left(1+k_l'\right)R^2}{M(2l+1)}\right]\sum_{j=1}^{40962}h_j\left(\bar{P}_{lm}\left(\sin\theta_j\right)\cos m\lambda_j\right)A_j$$
$$\Delta\bar{S}_{lm}=\left[\frac{10.25\left(1+k_l'\right)R^2}{M(2l+1)}\right]\sum_{j=1}^{40962}h_j\left(\bar{P}_{lm}\left(\sin\theta_j\right)\sin m\lambda_j\right)A_j \tag{2-8}$$

To derive the CSR SH solutions, they use orthogonal transformations to convert the design matrix or the information matrix H of size $m\times n$ to an upper triangular matrix R of size $n\times n$ [Tapley at al., 2004a]

$$Rx = b \tag{2-9}$$

where $QH = R$ and $Qy = b$; Q is the orthogonal matrix that transforms the H matrix to R matrix, an upper triangular matrix, and also the observation vectors y to a corresponding b vector. The $\hat{x}$ vector consists of all the global spherical harmonic coefficients with degree/order complete to n_{max} (120 in this study).

Now we assume vector x consists of the coefficients ($\Delta\bar{C}_{jlm}$ and $\Delta\bar{S}_{jlm}$) and vector z is composed of mass anomalies of 40,962 tiles, proportional to the equivalent water depth h_j for each of the 40,962 tiles. Then, the relationship between x and z can be expressed as

$$x = Tz \tag{2-10}$$

where T is the transformation matrix to transform the mass anomaly (cm of equivalent water for geodetic tiles) to the change in the spherical harmonic coefficients. Assume that $T(a, j)$ is the element of the transformation matrix T at the ath row and jth column, and $x(a)$ is the element in vector x representing the coefficient of $\bar{C}_{jlm}$ and $\bar{S}_{jlm}$, then comparing (2-8) and (2-10) we obtain

$$\begin{aligned} T(a,j) &= \left[\frac{10.25\left(1+k_l'\right)R^2}{M(2l+1)}\right]\left(\bar{P}_{lm}(\sin\theta_j)\cos m\lambda_j\right)A_j \\ T(a,j) &= \left[\frac{10.25\left(1+k_l'\right)R^2}{M(2l+1)}\right]\left(\bar{P}_{lm}(\sin\theta_j)\sin m\lambda_j\right)A_j \end{aligned} \tag{2-11}$$

where A_j is area of the jth tile. Substituting (2-10) into (2-9) and defining $RT = \bar{H}$, we get following equation,

$$\bar{H}z = b \tag{2-12}$$

Equation (2-12) gives us the linear transformation system relating the satellite range-rate and range-acceleration observations to the mass anomalies in each geodetic tile. However, this equation is rank deficient. In Save et al. [2016], they define an invertible matrix (M) (size $j \times j$), called the regularization matrix, and a scalar (μ), called the regularization parameter to formulate the Tikhonov regularization problem to get new state vector (z) by the equation below.

$$\hat{z} = (\bar{H}^T\bar{H} + \mu M^T M)\bar{H}^T b \tag{2-13}$$

where $\bar{H} = RT$.

The 1st step is to make an intermediate GRACE solution that has less leakage between land and sea. This step is based on the method to make regularized SH solution that has significantly reduced striping errors and all signals within the noise-level in Save et al. [2012]. When we see RMS in SH solution, signals by large ices and hydrologic signals have much leakage from land to the ocean. In the CSR mascon solution, ocean RMS is fixed to 4 cm in all the regions even where RMS is less than 4 cm. In regions where RMS exceeds 4 cm, their RMS is preserved. The resulting grid, shown in Figure 2-3, is used as M^{-1} in the equation (2-13). Mascon parameters defined by z vector are calculated in each 40,962 geodetic tiles and for each months by using (2-11). This solution is used as an intermediate GRACE solution and the basement for the 2nd step.

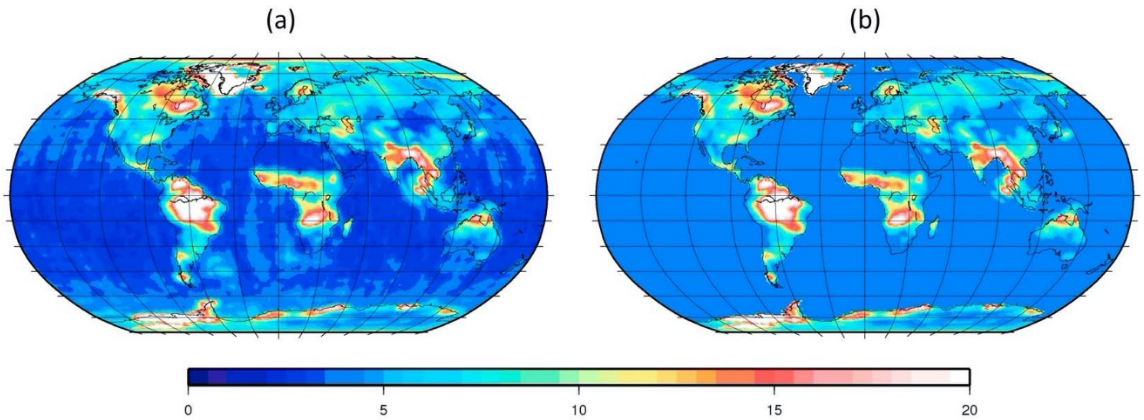

Figure2-3: (a) RMS grid of regularized GRACE SH solution (b) Grid representation of the (M) used for the step 1 [Save et al., 2016].

The 2nd step is to design time-variable regularization matrices (M) to estimate mascon solutions by using the intermediate GRACE solution. Corrections for various factors are applied, but one has to be careful in over- or under-constraining the parameters. In the CSR mascon solution, the regularization matrix (M) is made by combining the forward modeling of the large annual and secular signals and the correction from the regularized GRACE estimates. Annual changes and linear trends in the forward modeling are designed as follows.

(1) Linear trends

Linear trends in the forward model (called $\mathrm{L_{FM}}$) are computed by a method given below. The components C_{20} and C_{21} obtained in the 1st step (called $\mathrm{L_{C20}^{S1}}$ and $\mathrm{L_{C21}^{S1}}$, respectively) are subtracted from linear trend of the result in Step1 ($\mathrm{L_{S1}}$). Furthermore, the ICE5G GIA model by Geruo et al., (2013) (called $\mathrm{L_{GIA}}$) is subtracted. Then, the filter (HLIEF) is applied to this result. In HLIEF, they retain linear trends exceeding 2 cm/yr only in regions with high latitudes (>50° or <-45°) or regions around the Sumatra and Tohoku-Oki earthquakes and fix the others to 0. After this filter, C_{20} and C_{21} components in SH solution RL05 ($\mathrm{L_{C20}^{RL05}}$ and $\mathrm{L_{C21}^{RL05}}$) and $\mathrm{L_{GIA}}$ is added. This process is represented in equation (2-14)

$$L_{FM} = \mathrm{HLIEF}\left[L_{S1} - L_{C20}^{S1} - L_{C21}^{S1} - L_{GIA}\right] + L_{C20}^{RL05} + L_{C21}^{RL05} + L_{GIA} \qquad (2\text{-}14)$$

(2) Annual components

In the annual component, process is performed for only C_{20}. The C_{20} component obtained in the 1st step is replaced with that in the RL05 SH solution.

By applying these processes, linear components occur for only ice loss and GIA signals in high latitude regions, and megathrust earthquake signals. Annual components occur for all regions.

Residuals of the intermediate mascon solution with respect to the forward modeled signals (called G1(t) grid hereinafter, t is the time) provide the 1st step to make time variable regularization matrix for avoidance of bad influence caused by long-term statistics of the RMS of the residual. They made residual grid G2(t) with respect to the forward model described above by using the regularized spherical harmonic solution in Save et al. [2012]. They applied a 200 km Gaussian smoothing.

For $j = 1, \ldots, 40962$, at any given time step t,

$$\begin{gathered} M^{-1}(j,t) = \mathrm{MAX}[G1(j,t), G2(j,t)] \ \ \text{for land tiles} \\ M^{-1}(j,t) = G1(j,t) \ \ \text{for ocean tiles} \end{gathered} \qquad (2\text{-}15)$$

where, $M^{-1}(j,t)$ is the diagonal entry in the M^{-1} matrix at the jth row and column for the solution time t. Because a 200km Gaussian filter causes leakage from land to the ocean, only $G1(t)$ is used in the ocean. Furthermore, this solution does not allow correlations between neighboring cells because it may cause longitudinal stripes. These procedures make the CSR mascon solution capture regional time-variable gravity signals without attenuation.

In this paper, I use the mascon solution from CSR RL06 (http://www2.csr.utexas.edu/grace/RL06_mascons.html). One of the differences of the mascon solutions between CSR and JPL is the areas of the tiles. JPL employs 3° grid and this is too large to suit the purpose of my study.

2.2 Satellite altimetry data

We use global monthly SSH data combined multiple satellite altimetry (Topex/Poseidon, Jason1-3, ERS1-2 and Envisat) from AVISO. The data are available at grid points with 0.25° x 0.25° separation. However, we averaged them to 1° grid data to make it possible to directly compare with the GRACE data.

2.3 Tide gauge data

In this work, we obtained monthly SSH data at 6 tide gauge stations around GOC and 4 stations around GOT (positions shown in Figure2-4 and 2-5) provided from the website of the Permanent Service of Mean Sea Level (PSMSL) [Holgate et al., 2013; PSMSL, 2018]. The two stations around GOC (Centre Island and Melville Bay) seem to have lower accuracy than the other stations.

2.4 GNSS data

We used data of horizontal movement of 7 GNSS stations around GOC and 3 around GOT (positions shown in Figures 2-4 and 2-5) available from the data base at the Nevada Geodetic Laboratory in University of Nevada Reno (UNR) [Blewitt et al., 2018]. All observation points have time spans of the data exceeding 2 years and are sufficient for calculating seasonal crustal movements.

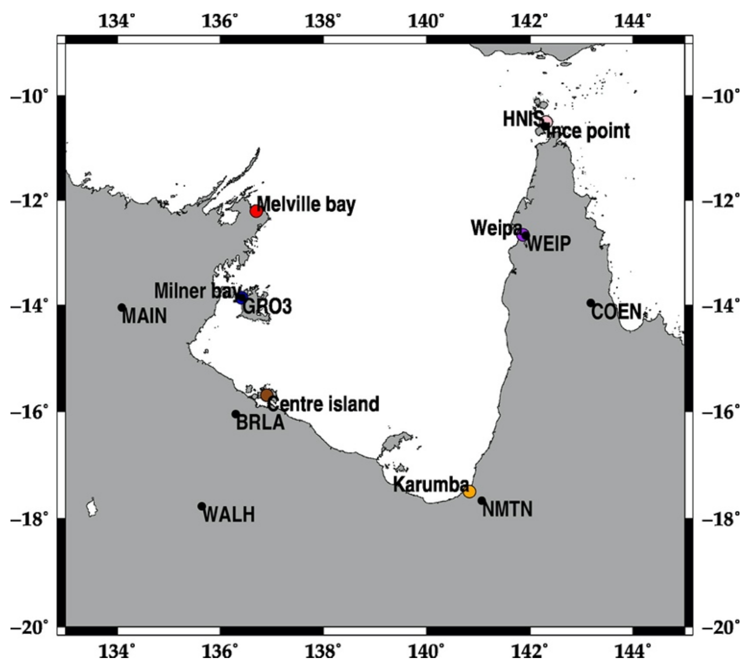

Figure2-4: Positions of tide gauges and GNSS stations around GOC. GNSS stations is indicated by black dots. Others show tide gauges.

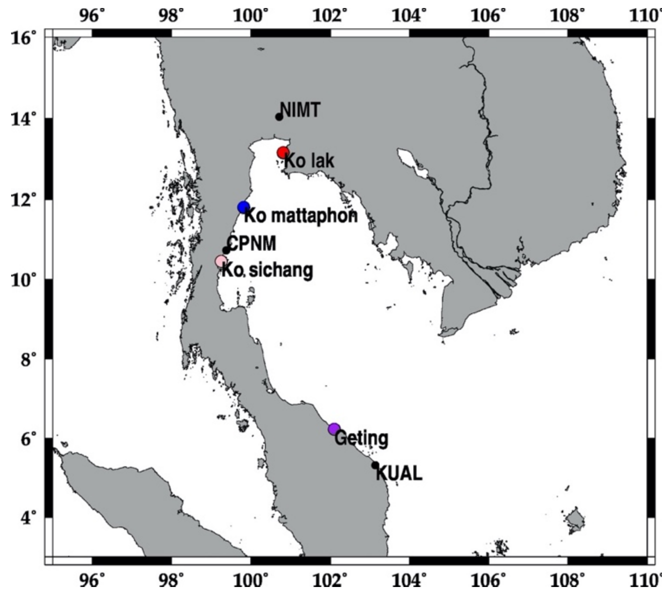

Figure2-5: Positions of tide gauges and GNSS stations around GOT. GNSS stations is indicated by black dots. Others show tide gauges.

2.5 Thermal Expansion of Seawater

In this paper, I use reanalysis data of seawater temperature and salinity accessible in homepage (https://www.metoffice.gov.uk/hadobs/en4/download-en4-2-0.html) of MET (METeorological) office in UK, version EN4.2.0. [Good et al., 2013]

2.6 Numerical calculation

Solid earth deforms by various surface loads, e.g. water, snow and atmosphere. Elastic response of the Earth to surface loads is given as the Green's function [Farell, 1972], which is sensitive to the Earth's rheologic structure [Chanard et al., 2014; Wahr et al., 2013]. Argus et al (2017) use vertical component of GPS data to calculate change of total mass load and compare with GRACE data. In terms of horizontal, surface load also causes movement of GNSS and displacement can be computed by Green's function [Farell, 1972].

We use the Green's function to calculate surface displacement by surface loads. Load distribution was derived from GRACE, altimeter, and tide gauge, in which GRACE data represent larger areas than the other two owing to poor spatial resolution. I used satellite altimeter for the ocean, especially tide gauge for coastal region.

In the calculation of surface displacements by loads, we used a subroutine from the software package GOTIC2 (Global Ocean Tide Calculation) [Matsumoto et al., 2001]. Below is the description of the calculation procedure.

Horizontal displacements by ocean tide load L is given by equation (2-15).

$$L(\theta', \lambda') = \rho \int \int H(\theta, \lambda)\, G_L(\phi)\, T(\alpha) dS \qquad \text{(2-14)}$$

where ρ is the ocean water density, H is the ocean tidal height, G_L is the Green's function for displacements, and T is the combination of trigonometric functions of azimuth (α) which is necessary to compute horizontal displacement vectors by the load. H and L are complex-valued with the real and imaginary parts representing the east and north components, respectively.

The Green's function for radial displacement is given by equation (2-16).

$$G_L^{RD}(\phi) = \frac{R}{M_e} \sum_{n=0}^{\infty} h'_n\, P_n(\cos \phi) \qquad \text{(2-16)}$$

M_e and R is mass and radius of the Earth (assumed spherical), h'_n is the load Love number and P_n is the Legendre function of degree n. When integrating Green's function over the finite area dS in (2-15), if dS is small enough, we can approximate the Green's function using a quadratic polynomial as follows.

$$F(\phi) G_L(\phi) = a + b\phi + c\phi^2 \qquad \text{(2-18)}$$

For displacements and gravity, $F(\phi) = R\phi$. Then contribution of loading at a grid point (θ_c, λ_c) with size of Δ_y by Δ_λ is given as equation (2-19).

$$\Delta L_i(\theta', \lambda') = \rho R^2 \int_{\lambda_c - \Delta_\lambda/2}^{\lambda_c + \Delta_\lambda/2} \int_{\theta_c - \Delta_\theta/2}^{\theta_c + \Delta_\theta/2} H(\theta, \lambda) \frac{a + b\phi + c\phi^2}{F(\phi)} \qquad \text{(2-19)}$$

By approximating the integration area in (2-19) as a rectangle with size Δx and Δy, we can project the spherical coordinates on a plane contacting the Earth at the center of the area (X_c, Y_c). We can transform equation (2-19) with $T(\alpha) = 1$ for radial displacement.

$$\Delta L_i^{RD}(x', y') = \rho \int_{x_c - \Delta_x/2}^{x_c + \Delta_x/2} \int_{y_c - \Delta_y/2}^{y_c + \Delta_y/2} H(x, y) \left[\frac{a}{\sqrt{(x' - x)^2 - (y' - y)^2}} + \frac{b}{R} + \frac{c}{R^2} \sqrt{(x' - x)^2 - (y' - y)^2} \right] dxdy \qquad \text{(2-20)}$$

Total effect of loadings can be obtained as the sum of ΔL_i over the whole grids.

$$L = \sum_i \Delta L_i \qquad \text{(2-21)}$$

Chapter3 Results

3.1 GOC (Gulf of Carpentaria)

3.1.1 SSH change

First, I compare 2 GRACE solutions to see mass changes in GOC. Figure3-1 is the average seasonal change in December. In the SH solution, the phases of seasonal change in the ocean and on land are mostly the same. On the other hand, seasonal changes in the ocean have a different phase from those on land in the mascon solution. Such seasonal changes are driven by precipitation on land and wind stress in the ocean. Here I consider that the mascon solution reflects the reality more than the SH solution.

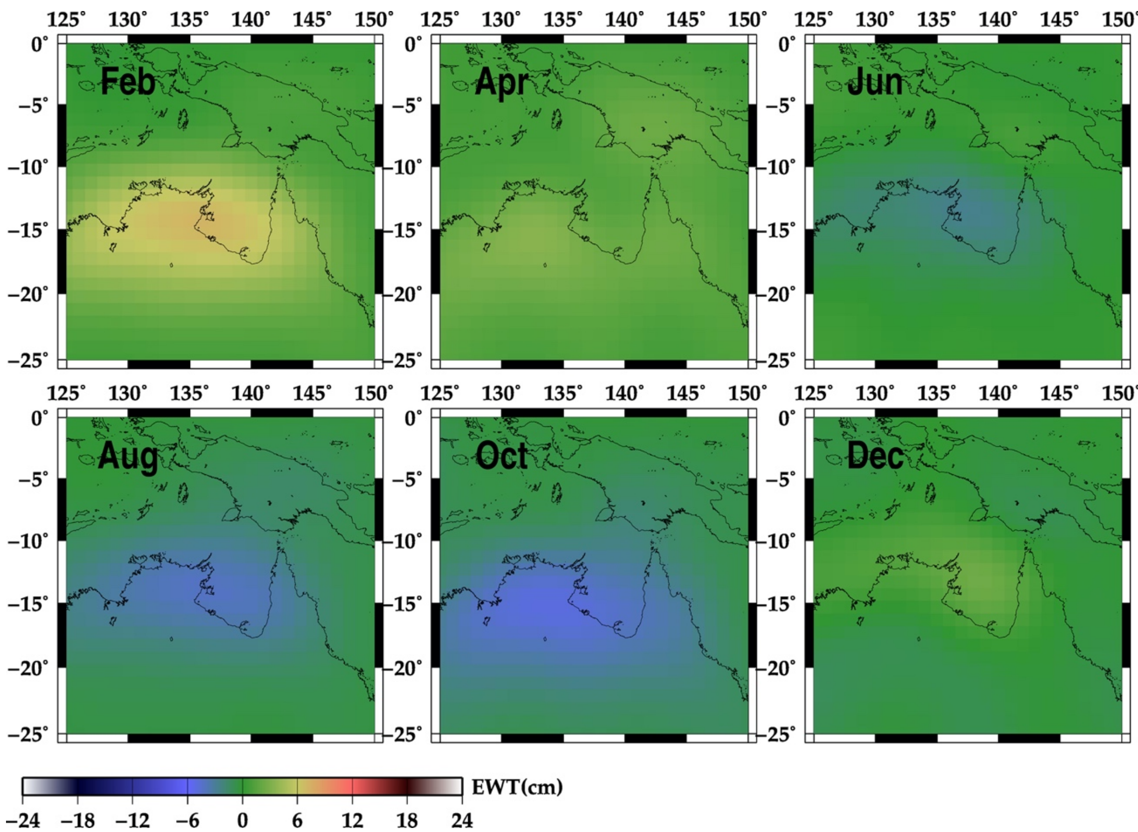

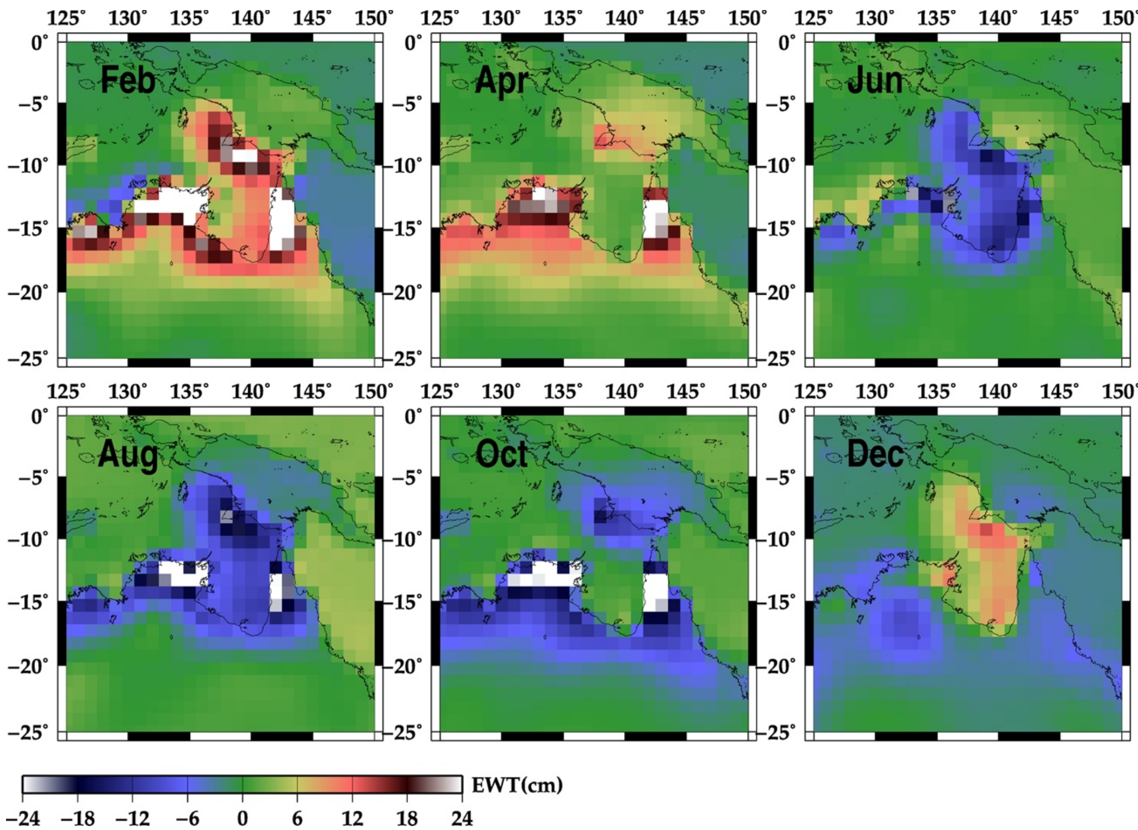

Figure3-1: Averaged seasonal changes (every other month) of the GRACE SH (above) and the mascon (below) solutions.

I compare the two GRACE solutions in time-series. Figure3-2 is the mass-driven SSH change in GOC (definition of area is shown in Figure1-20). The mascon solution has about twice as large amplitude as that of the SH solution.

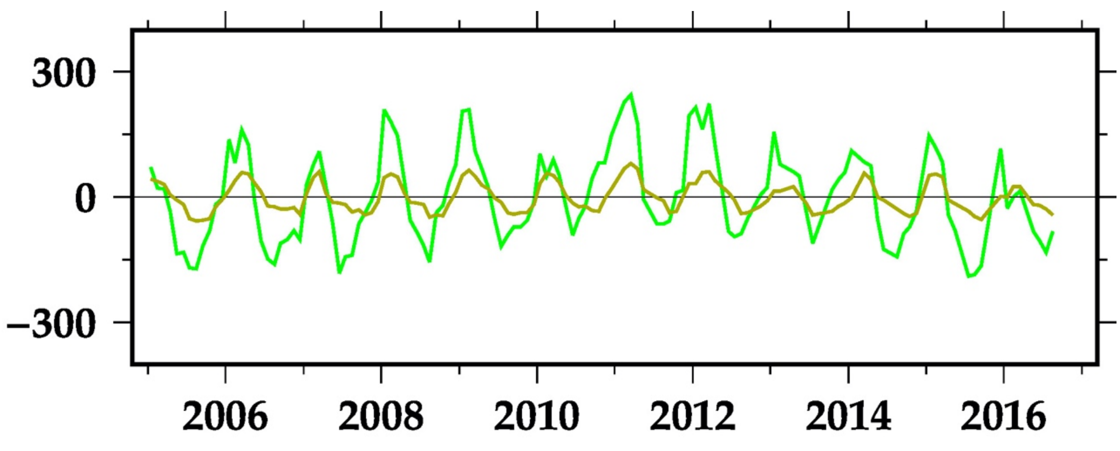

Figure3-2: SSH change at the center of GOC calculated using the GRACE mascon (green) and the SH (yellow) solutions. Unit is mm.

The difference between the 2 results would imply that the mascon solution can discriminate mass signals between the ocean and the land better than the SH solution. Below I use the mascon solution to compare with altimetric and thermosteric SSH changes.

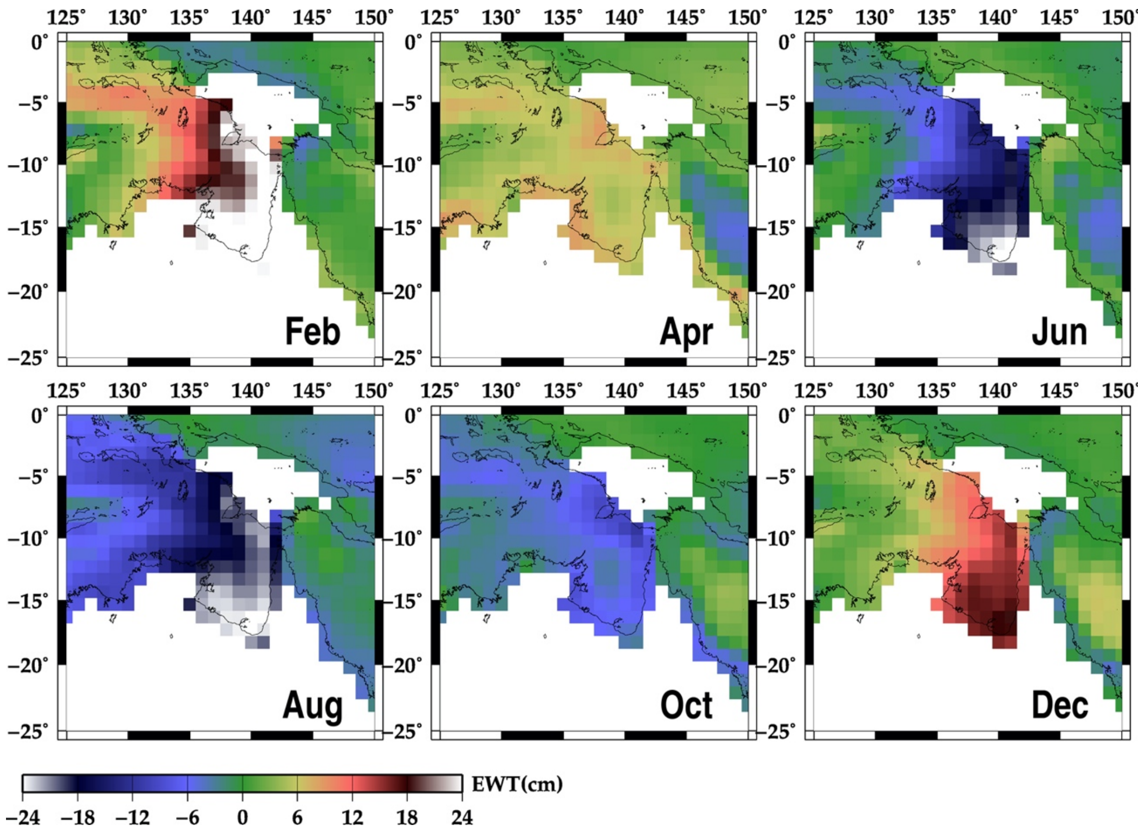

Figure3-3: Average seasonal SSH changes from satellite altimetry.

When comparing the mascon solution with the SSH data from altimeter, we can see that the mascon solution shows only a half of the amplitude of the altimetric data. Figure 3-4 shows average seasonal SSH changes of 3 indices in GOC. We can see that the mass-driven SSH change accounts for ~60% in the total SSH change. On the other hand, thermometric SSH change accounts for only ~10%. Therefore these 2 values cannot fully explain the seasonal altimetric SSH changes. The mascon solution can observe mass change with higher spatial resolution than the SH solution in GOC. Nevertheless, it does not completely describe the real changes in this shallow sea. Linear trend cannot be seen because of large amplitude of seasonal change.

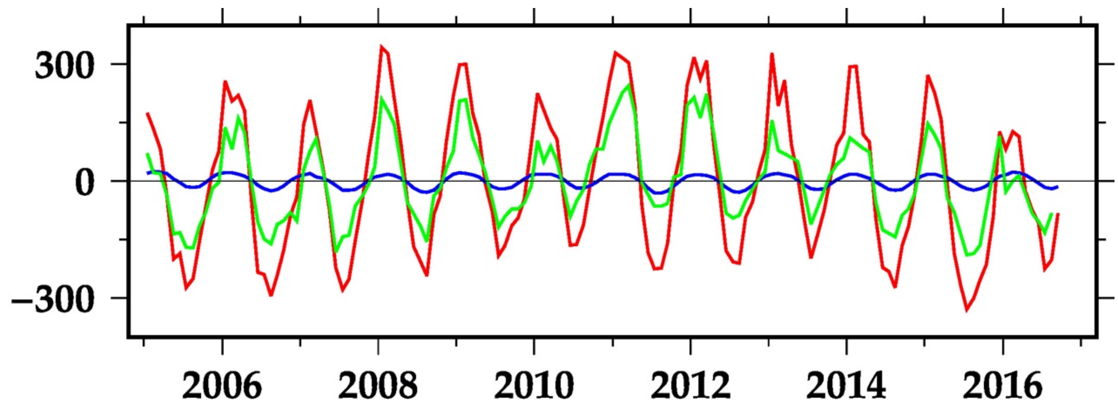

Figure3-4: SSH change observed by 3 different sensors (red : altimeter, blue : thermosteric, green : GRACE mascon) in 2005-2016

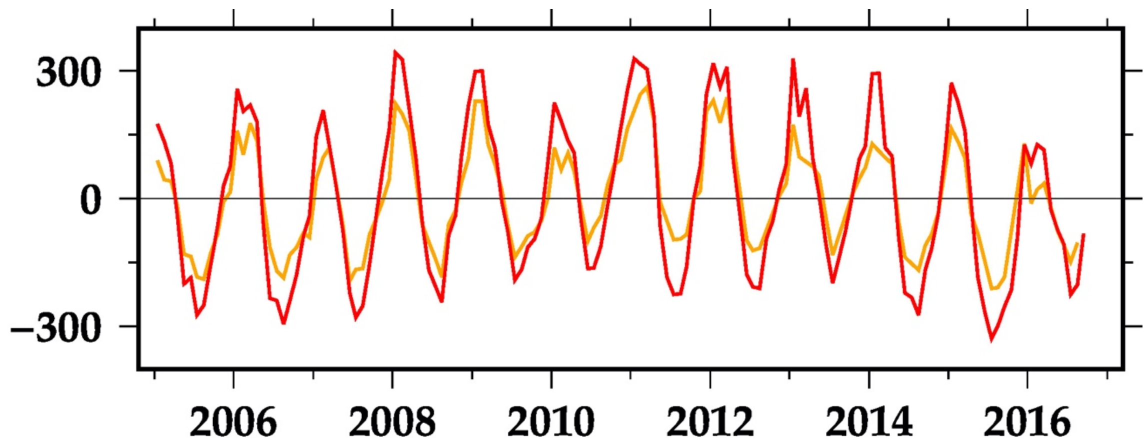

Figure3-5: Comparison between the SSH observed by altimetry and SSH reconstructed as the sum of the other 2 values (red: altimetric, orange: thermosteric + GRACE). Altimetric data can be reproduced about 80% by the other 2 values.

Next, I will see the seasonal and inter-annual SSH changes by using the Empirical Orthogonal Function (EOF) analysis of the raw data to study seasonal changes and of the data after removing linear and seasonal components to study inter-annual changes. Furthermore, I compare the SSH data from altimeter and from conventional tide gauges.

3.1.1.1 Seasonal change

The 1st mode in the altimetric EOF (35%) obtained using the raw data clearly shows seasonal changes, with the maximum in austral summer and minimum in winter being consistent with the previous studies (Figure3-6) [Wang et al., 2016; Tregoning et al. 2008].

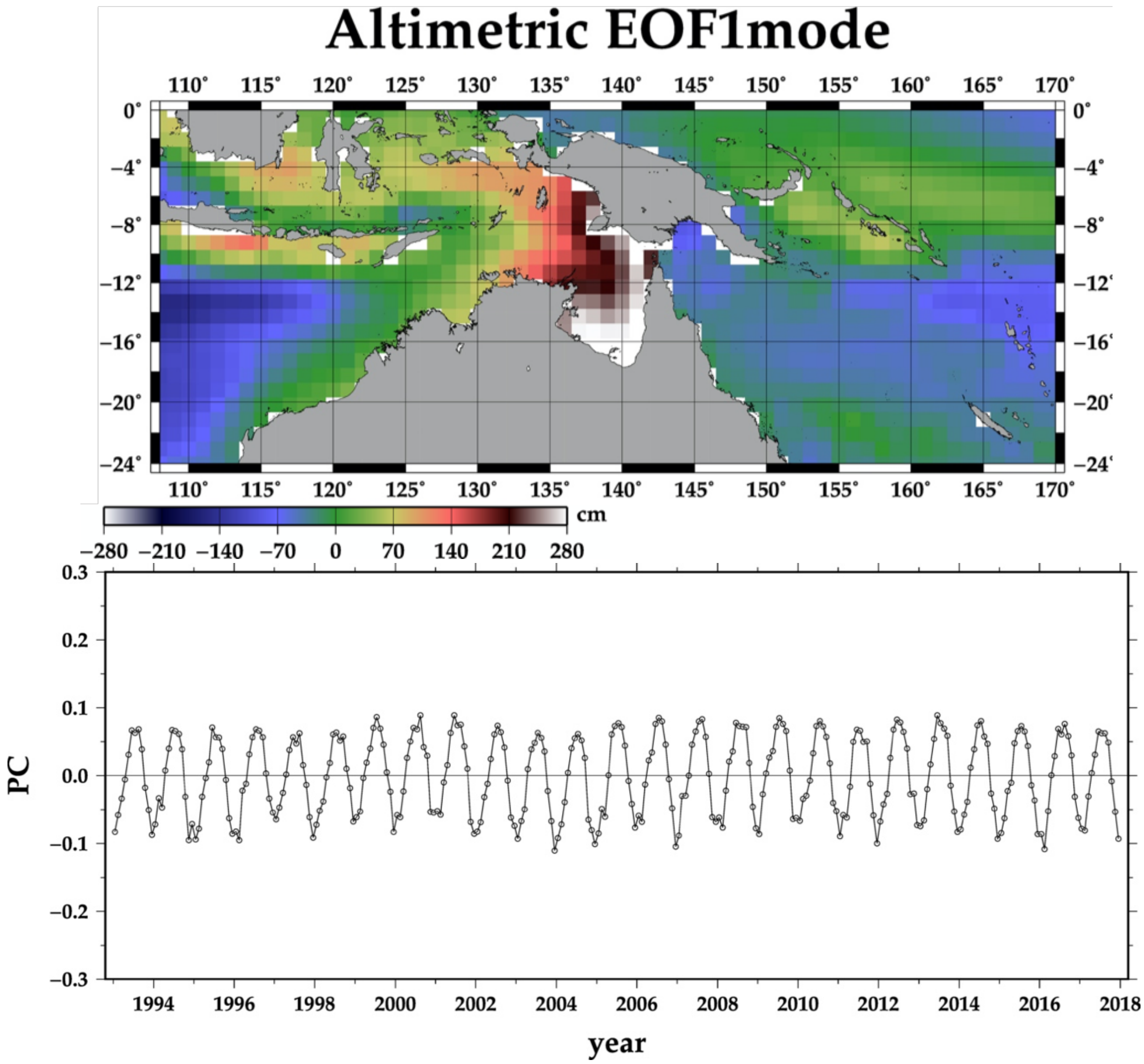

Figure3-6: Spatial (top) and temporal (bottom) functions of the EOF 1st mode () from the raw data of SSH in GOC.

Next, I compare seasonal change of SSH between altimeter and tide gauges. Average monthly changes are shown in Figure 3-7. Phases of these seasonal changes are coherent, and their amplitudes get larger at tide gauges deep inside of the gulf (Figure1-20). This would be physically reasonable if these seasonal changes are driven by seasonal winds toward SE.

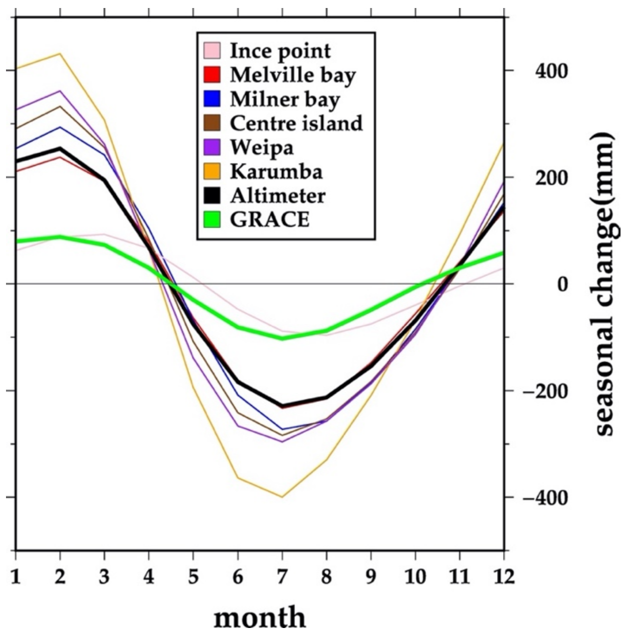

Figure3-7: Average monthly changes of SSH from satellite altimeter (black) and GRACE (green) at the center of GOC and tide gauges (others) around GOC. See Figure 1-10 for the tide gauge locations.

3.1.1.2 Inter-annual change

Figure 3-8 shows temporal and spatial functions of the altimetric EOF 1st and 2nd modes derived from the data after removal of the linear trend and seasonal variations. The 1st mode (34%) is correlated with the ENSO index (r=0.652). Although there is a time lag of a few months, 2 values show good correlation in both short and long period changes. The 2nd mode (13%) is correlated with not only ENSO (r=-0.529) but also IOD (r=-0.442).

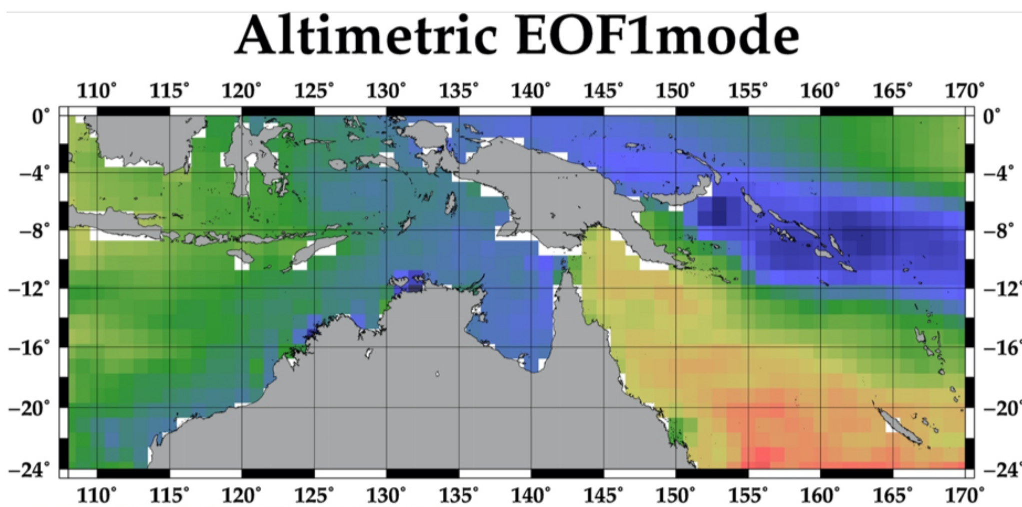

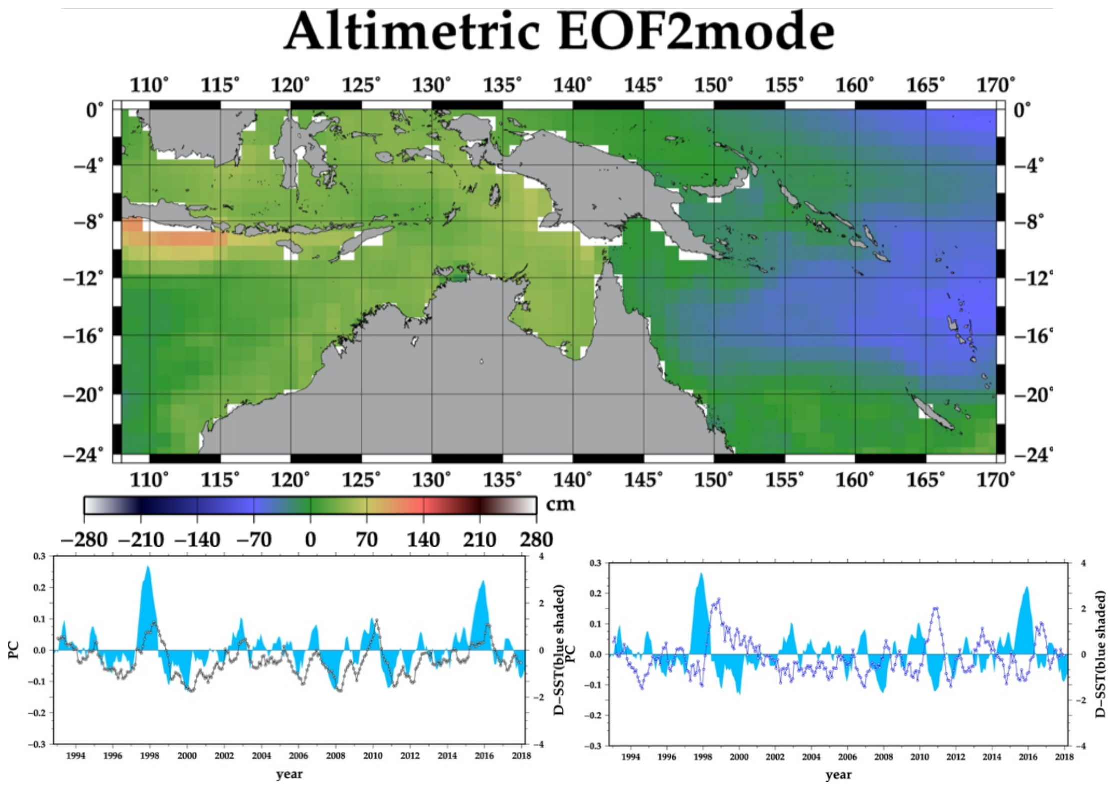

Figure3-8: Space and time functions of the EOF 1st and 2nd modes derived from the altimetric data after linear and seasonal components are removed.

This correlation between SSH and ENSO can also be seen in the tide gauge data (Figure3-9). Out of the 6 tide gauges used in this paper, 5 gauges were negatively correlated (r = -0.643 ~ -0.537) with the ENSO index. No gauges have correlation with IOD.

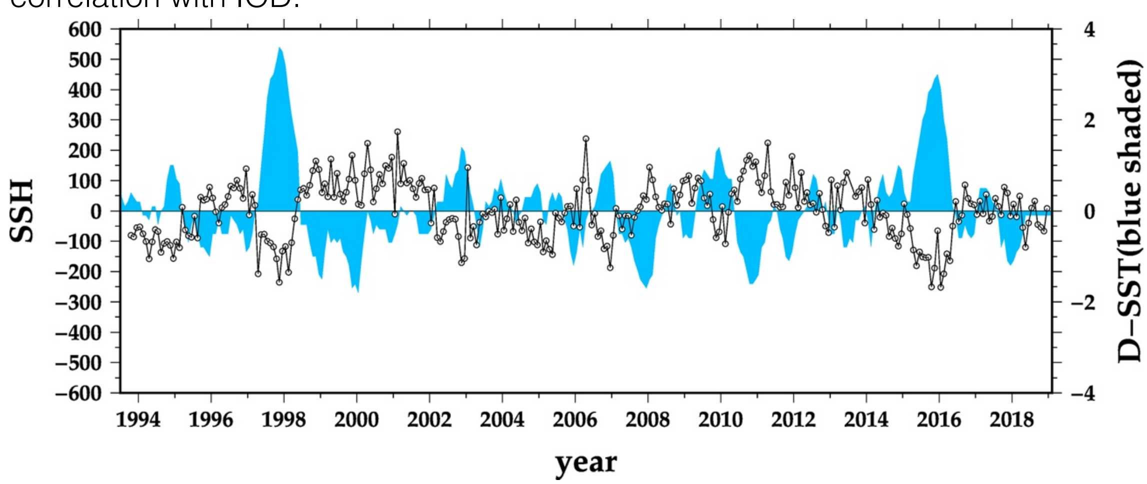

Figure3-9: Time-series of SSH from the Milner Bay tide gauge and the Nino3 D-SST. Their correlation coefficient is -0.643

To find out which of the steric or mass component is correlated with ENSO, I try similar EOF analyses for the thermometric SSH change data after removing the secular and seasonal components. The 1st mode (42%, shown in Figure3-10) was found to have a correlation with ENSO (r=0.542) and IOD (r=0.579).

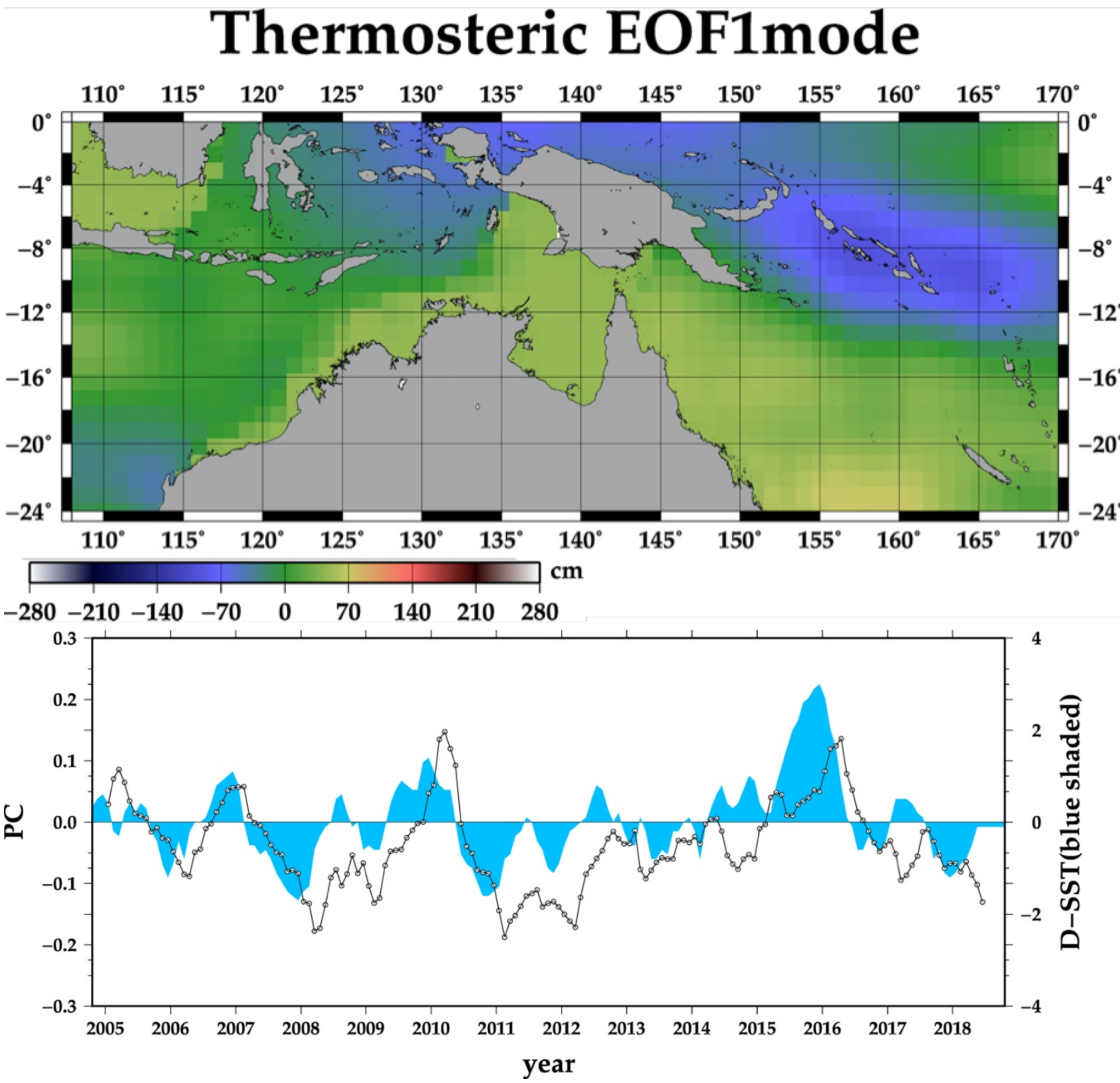

Figure3-10: Space and time functions of the EOF 1st mode from thermometric SSH changes after removal of secular and seasonal trends.

3.1.2 Mass change around GOC

Different from the other 2 quantities, altimetric and thermosteric SSH, GRACE data provide mass change information not only on the ocean but also on land. In this section, I attempt to separate signals between land and sea and to reveal characteristics of these areas through EOF analysis.

3.1.2.1 Seasonal change

Averaged seasonal change observed by GRACE show that the peak on the sea comes slightly earlier than that on land. This is because the drivers of seasonal changes are different between land (by precipitation) and ocean (by wind). This difference can also be seen by EOF-analysis to raw data of GRACE (Figure3-11). The 1st mode shows annual mass changes around GOC, and the 2nd mode shows slightly different annual changes between land and sea. Peak of the time-function of the 2nd mode comes slightly earlier than that of the 1st mode.

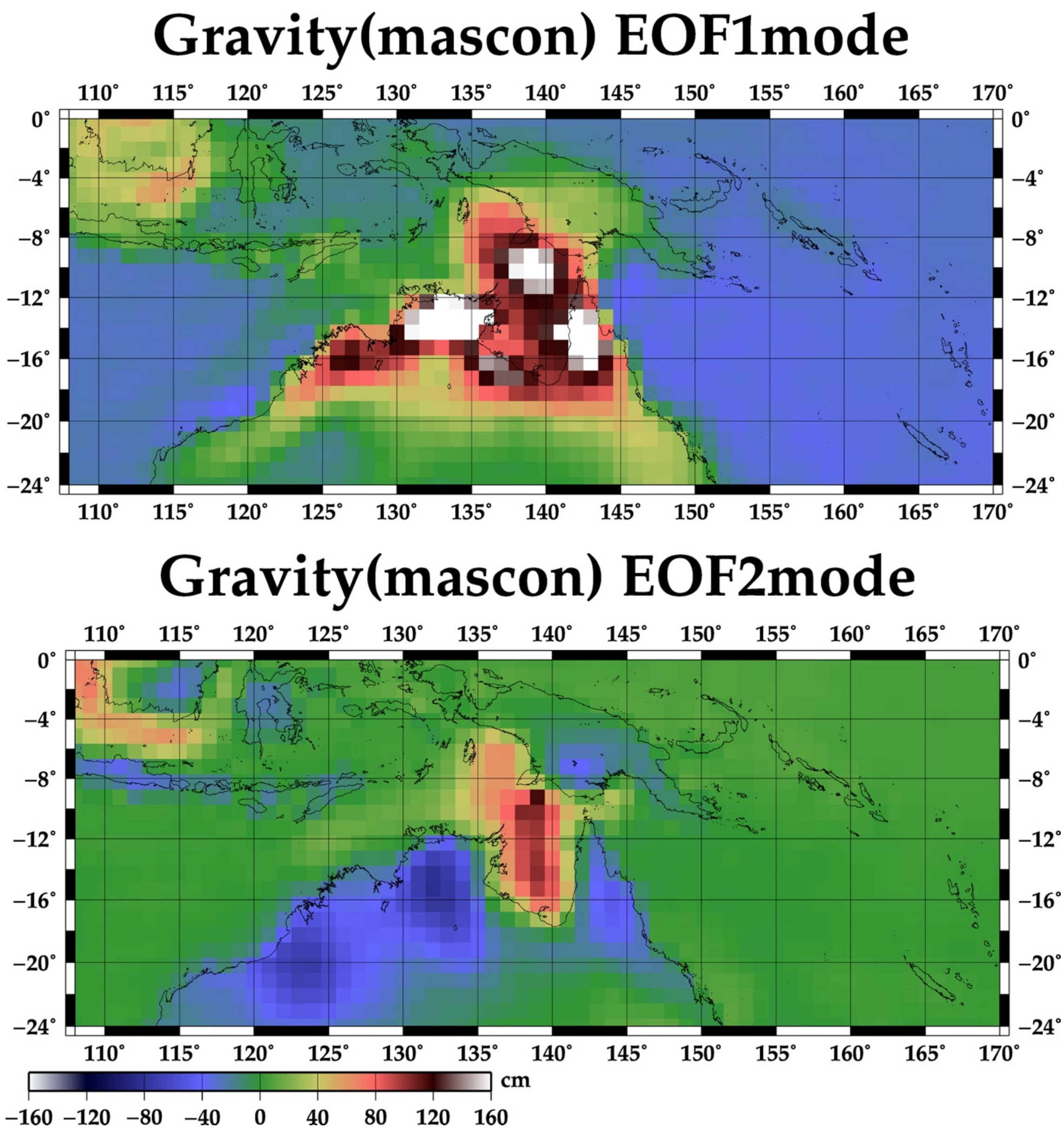

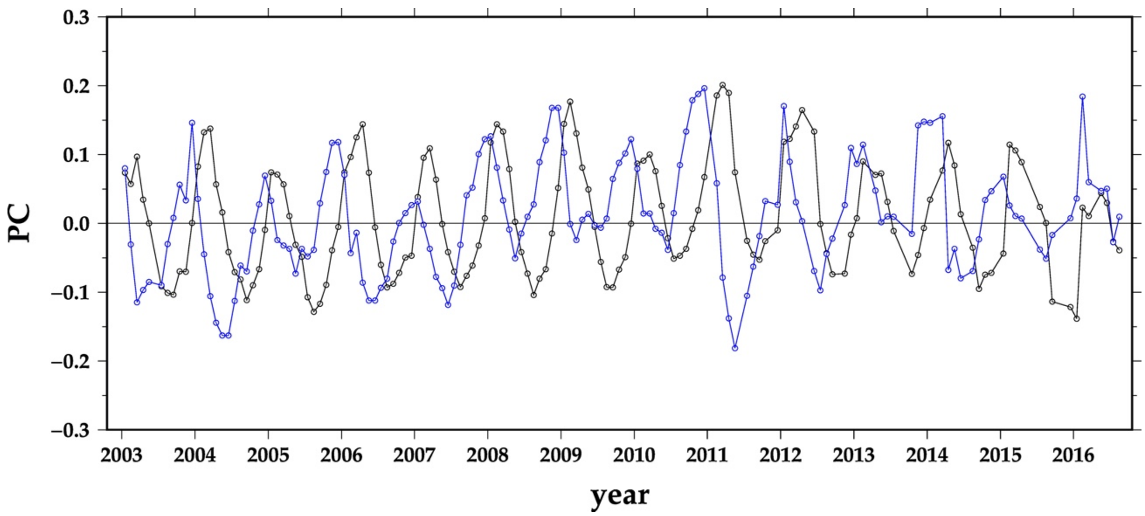

Figure3-11: The 1st (black) (54%) and the 2nd (blue) (14%) modes, derived from the raw GRACE mascon data, are shown with their spatial and temporal functions

The 3rd mode of EOF (10%) seems to reflect a dipole composed of the north-eastern and north-western parts of Australia. Temporal and spatial function of this mode is consistent with Rodell et al. (2018), i.e. it shows long-term alternation of precipitation and drought on the land (Figure3-12).

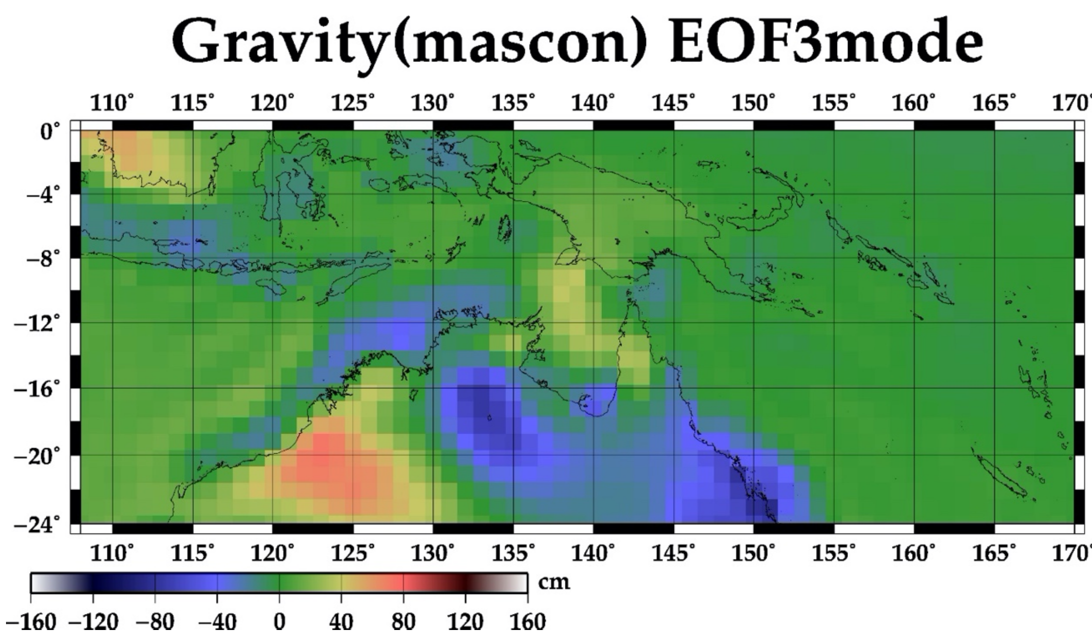

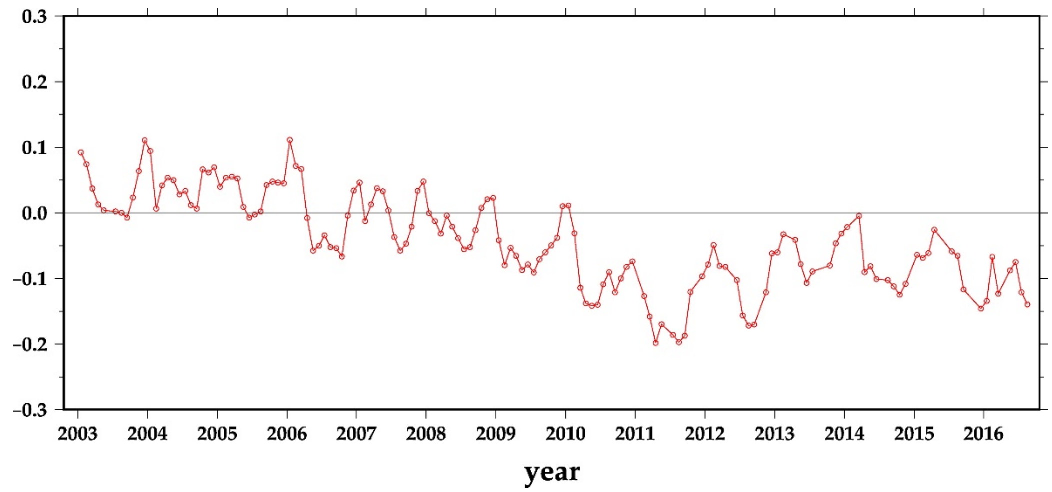

Figure3-12: Space and time functions of the EOF 3rd mode of the GRACE mascon solution.

3.1.2.2 Inter-annual change

By performing the EOF analysis on the GRACE mascon data after removing the secular and average seasonal components, we could see the influence of inter-annual climate changes.

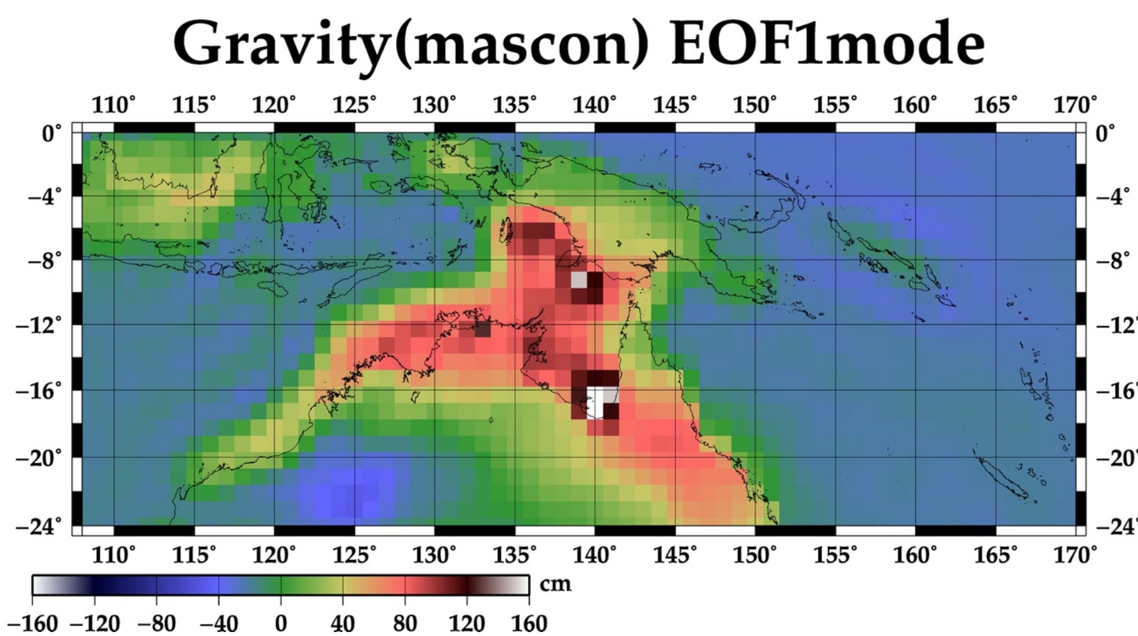

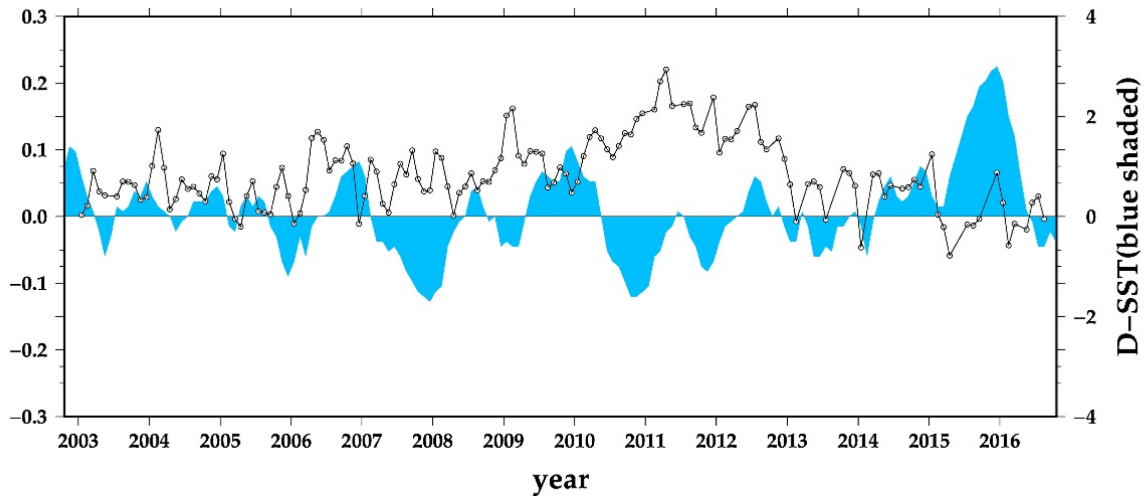

Figure3-13: Result of the EOF analysis for the GRACE mascon data after removal of average seasonal and linear components.

The EOF 1st mode (53%) seems to be related to climate changes. When compared with indices of climate changes, D-SST (ENSO index) is found to have a negative correlation (r=-0.565) with time function of this mode. Other indices such as IOD do not have so strong correlations.

3.1.3 Crustal movement

As seen in the previous section, different seasonal changes exist for different quantities around GOC. Can we see this difference by an independent observation? From here, I try to see crustal movements by Global Navigation Satellite Systems (GNSS) and compare them with the results of numerical calculations.

3.1.3.1 GNSS observations

To see how seasonal change of water storage in the ocean and on land emerge as crustal deformation signals, I show horizontal components of the GNSS stations around GOC (Figure3-14). They show clear seasonal crustal deformation, i.e. GNSS stations move towards GOC in austral summer and landward in winter. Maximum of the peak-to-peak seasonal displacement, e.g. in NMTN, is ~1cm.

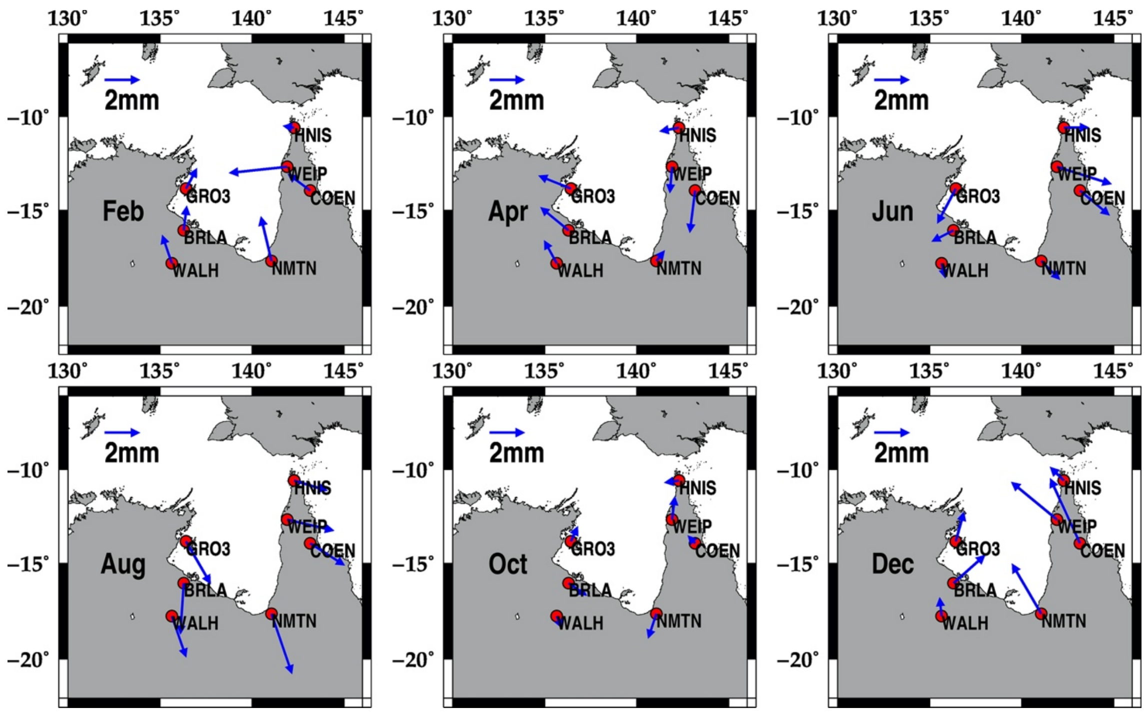

Figure3-14: Seasonal horizontal crustal movements (every other months) of GNSS stations around GOC. The arrows are drawn relative to the average positions of the stations.

3.1.3.2 Comparison with numerical calculation results

To consider validity of the observed seasonal horizontal movements of GNSS stations around GOC, I compare them with results of numerical calculation of crustal movements by surface load. I used the Green's functions and subroutines derived from the GOTIC2 software [Matsumoto et al., 2001]. In this study, calculation area is shown in Figure3-1, 3-3 and 3-14. Results of the calculation are shown in FIgure3-15. They are similar to the GNSS observations, i.e. the ground moves towards GOC in austral summer and against in winter reflecting increase of sea water load in summer. However, the amount of movement is about a half of what was observed by GNSS. In chapter4, I discuss the origin of such a discrepancy.

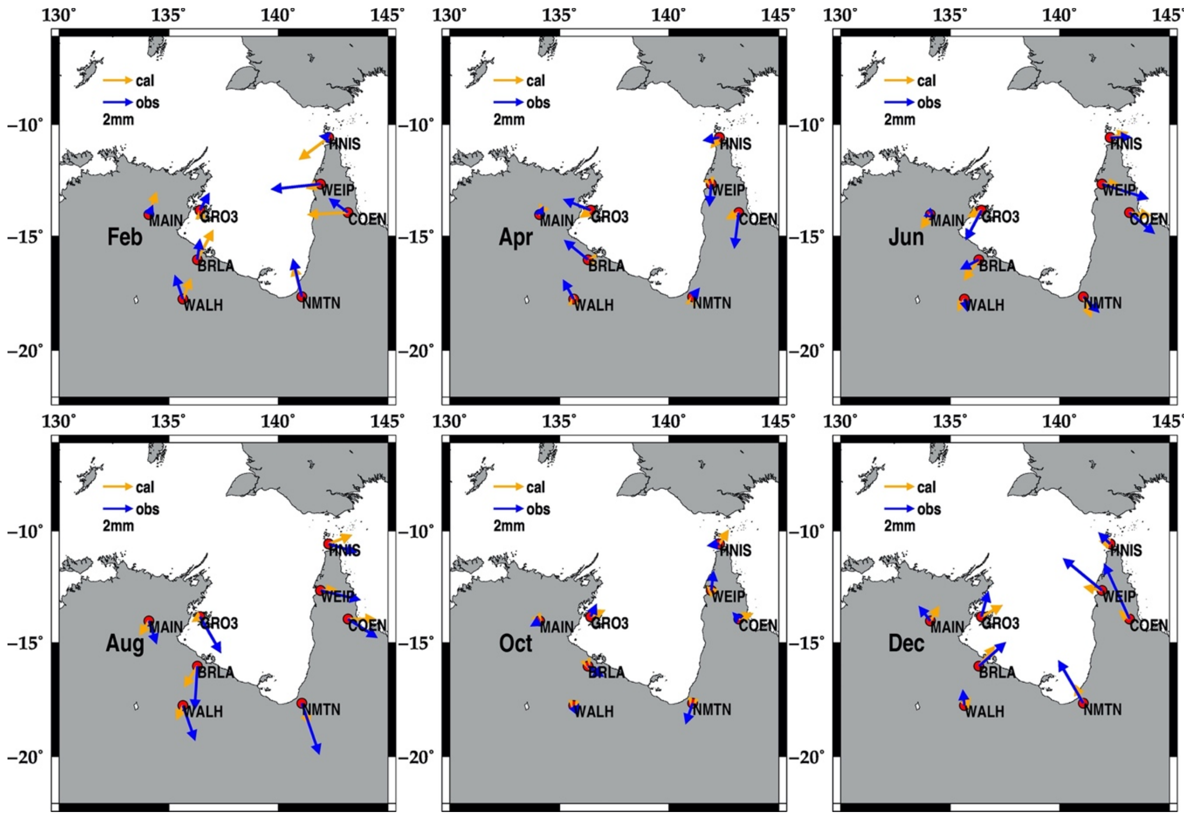

Figure3-15: Result of numerical calculation (orange). Blue arrow is the result of GNSS observation shown in Figure3-14.

3.2 GOT (Gulf of Thailand)

3.2.1 SSH changes

3.1.2.2 Inter-annual change

Similar to GOC, mass component accounts for most part of altimetric SSH change in GOT (Figure3-16). The large difference from GOC is the clear existence of the linear trend. In GOC, linear trend was much smaller than seasonal changes. On the other hand, in GOT, significant positive trend in altimeter ($7.062 \pm 0.842\ \mathrm{mm/yr}$) and significant negative trend in GRACE ($-4.591 \pm 0.927\ \mathrm{mm/yr}$) can be seen. SSH raise can be seen also by tide gauges. Linear trends at 3 tide gauge stations with records in 2005-2017 is 7~10 mm/yr. By the way, records over the past 40 years shows a less linear trend [Trisirisatayawong et al (2011)], suggesting that the SSH rise in GOT is accelerated.

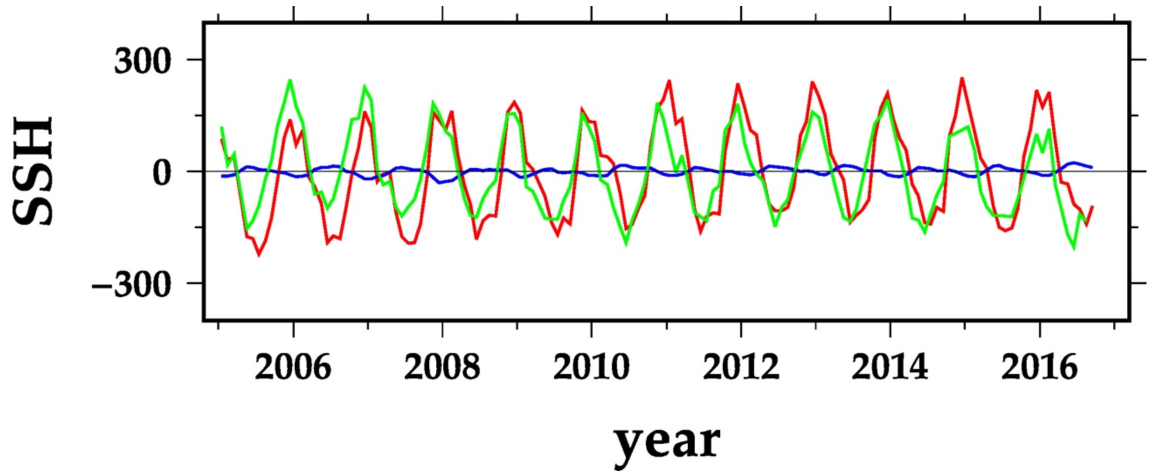

Figure3-16: 3 SSH indices (red: altimeter, blue: thermosteric and green: GRACE mascon) in 2005-2017. Annual changes of altimeter are consistent with those reconstructed by combining GRACE and thermosteric data (Figure3-17).

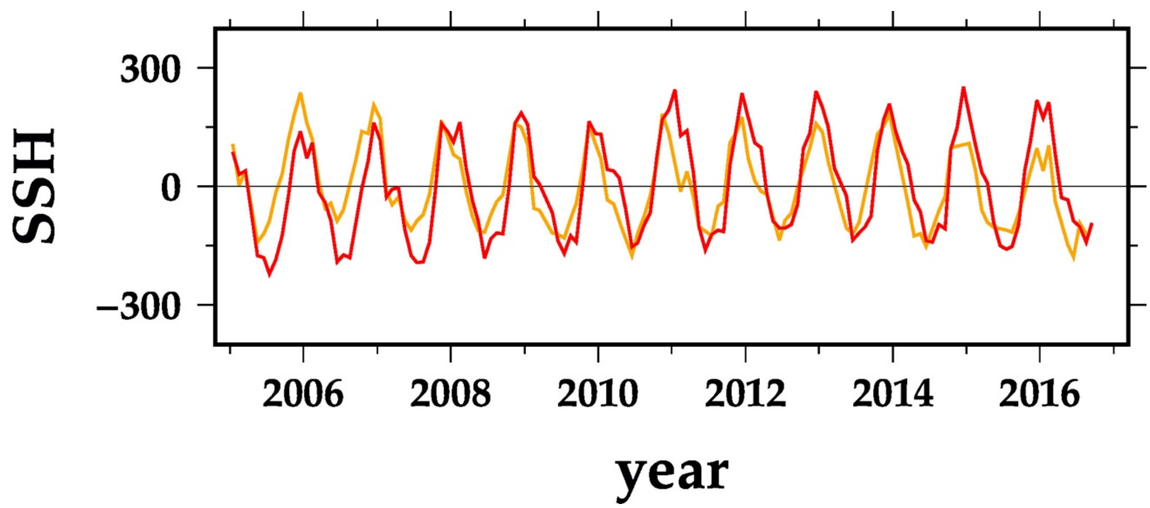

Figure3-17: Comparison of altimetric SSH by those reconstructed by combining the GRACE (barystatic) and thermosteric time series. (red) observation and (orange) reconstruction. Their seasonal components are in good agreement.

3.2.1.1 Seasonal changes

Seasonal change has a maximum in winter and minimum in summer as shown in Figure3-17. This can be seen in the result of EOF analysis of the altimetric data (Figure3-19). Seasonal change in GOT has the same phase as the coastal region of Vietnam.

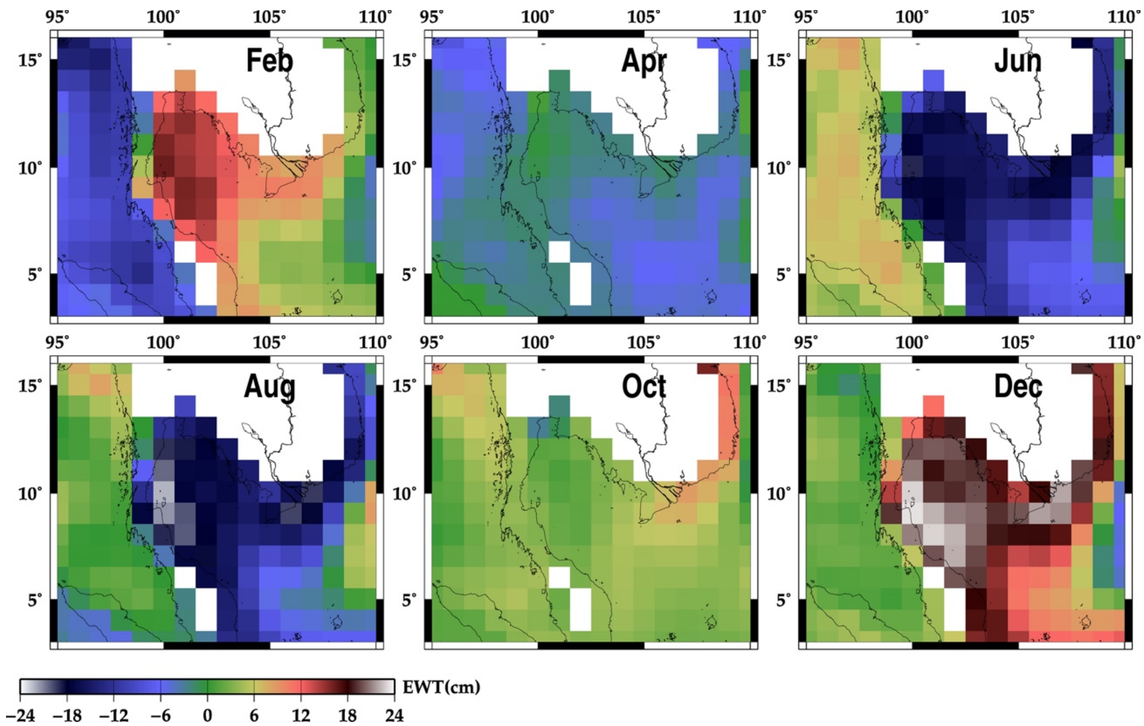

Figure3-18: Monthly averaged seasonal change of altimetric SSH around GOT.

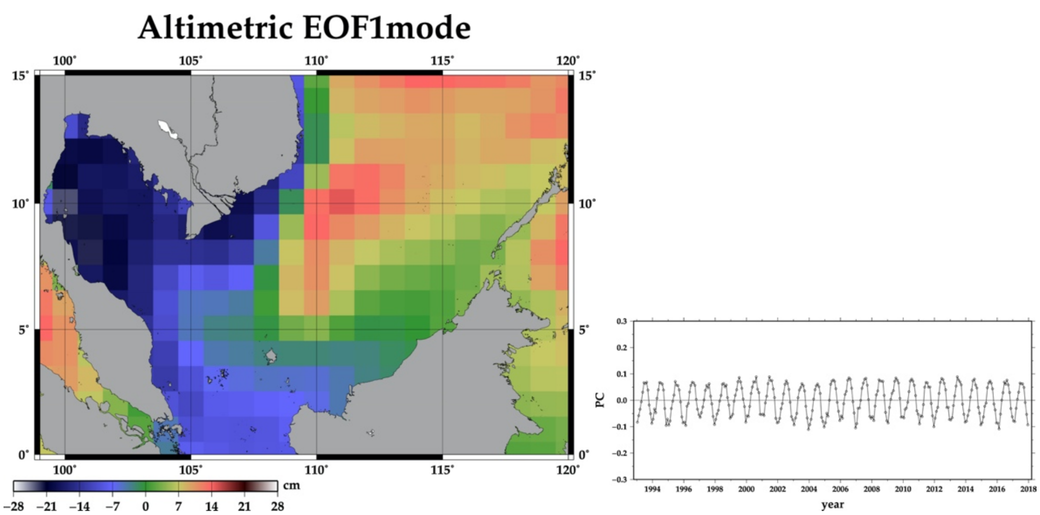

Figure3-19: Result of EOF analysis on altimetric SSH raw data.

This seasonal change can be also seen by the record of tide gauge (Figure3-20). There are no serious differences among 4 tide gauges.

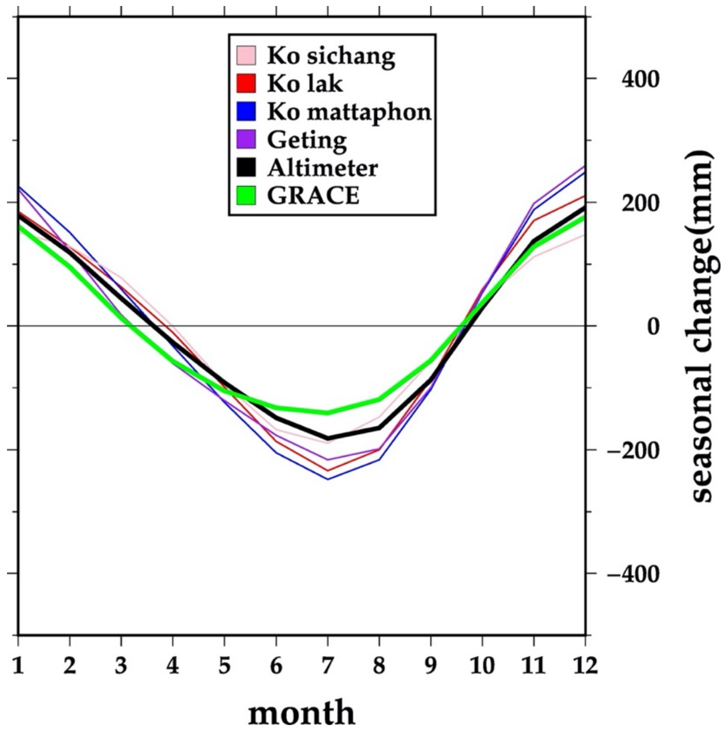

Figure3-20: Monthly averaged seasonal changes of SSH by altimeter, GRACE and tide gauge records at stations around GOT.

3.2.1.2 Inter-annual changes

Result of the EOF analysis on data after removing linear and seasonal trend shows correlation with ENSO index. Both 1st mode ($r = -0.524$) and 2nd mode ($r = -0.487$) has negative correlation with ENSO (Figure3-21). On the other hand, IOD does not have significant correlation with the EOF result.

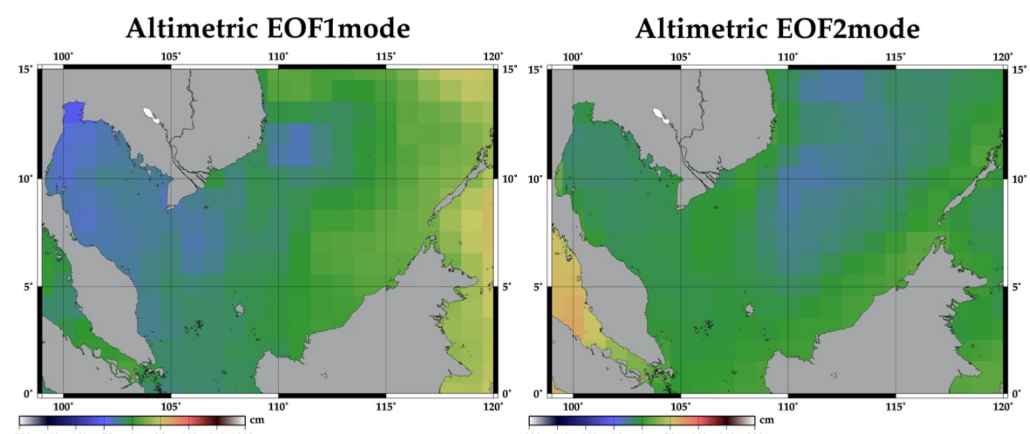

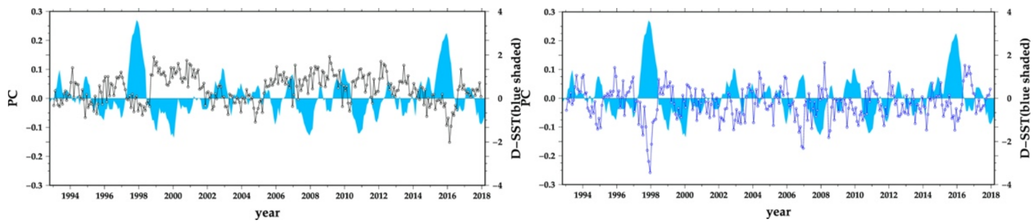

Figure3-21: Result of the EOF analysis on altimetric data after removing linear and seasonal components. We show space (top) and time (bottom) functions of the 1st mode (right) and the 2nd mode (left)

3.2.2 Mass changes around GOT

3.2.2.1 Seasonal changes

Monthly averaged seasonal gravity changes (Figure3-22) from the GRACE mascon solution show phases consistent with the altimeter data shown in Figure3-18. Opposite to GOC, the peak of seasonal changes in the GOT comes slightly later than that on land. Seasonal changes on land are strong at the Mekong River basin.

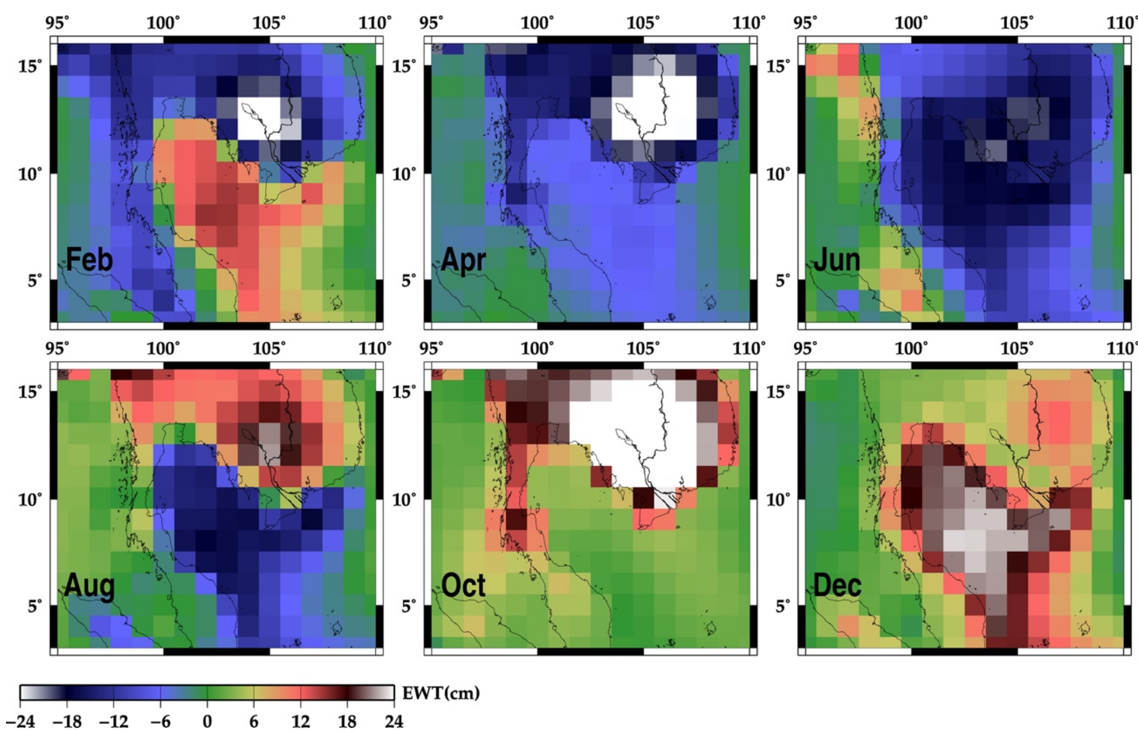

Figure3-22: Monthly averaged seasonal gravity changes around GOT.

Similar to the GOC case, comparison of the EOF 1st and 2nd modes in GOT highlights the difference of phase of seasonal change between land and sea (Figure3-23).

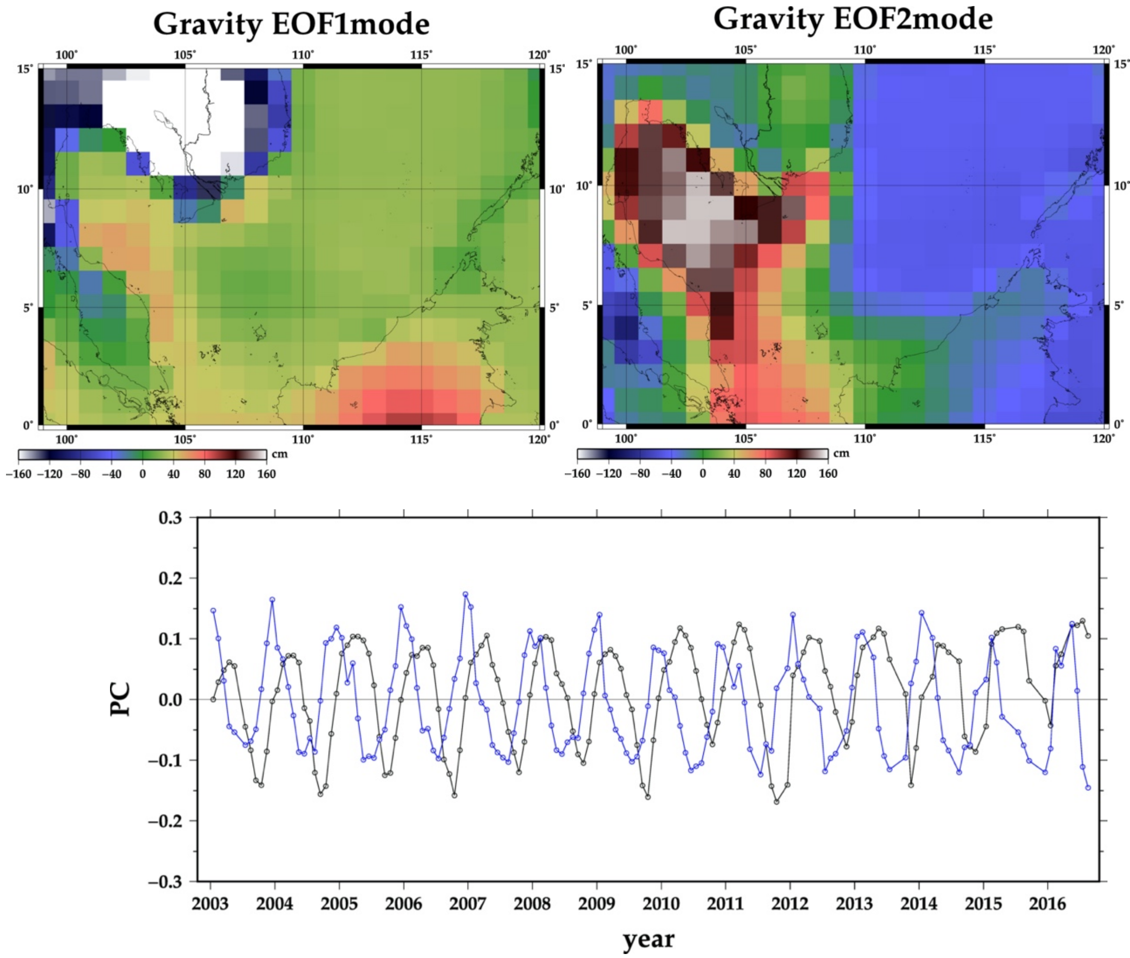

Figure3-23: Result of the EOF analysis on GRACE time-variable raw gravity data. 1st mode (black) mainly shows changes in groundwater and the water level of the Mekong River, 2nd (blue) mode shows mass changes in GOT. Temporal function shows difference between the peak seasons of the 2 modes.

3.2.2.2 Inter-annual change

Results of the EOF analysis (shown in Figure3-24) on the GRACE data after removals of the linear and seasonal components do not have correlations with the ENSO index and the IOD index. The 1st mode shows some influence from the co- and postseismic gravity change of the 2004 Sumatra-Andaman earthquake [Tanaka and Heki., 2016]. 2nd mode show strong signals around the Mekong River in Cambodia. Floods are observed in 2011 by water gauges near border between Vietnam and Cambodia [Uehara, 2012]. Spatial function of the 3rd mode show signals only in GOT, but it does not show correlation with climate change indices. It is still unknown what causes these changes.

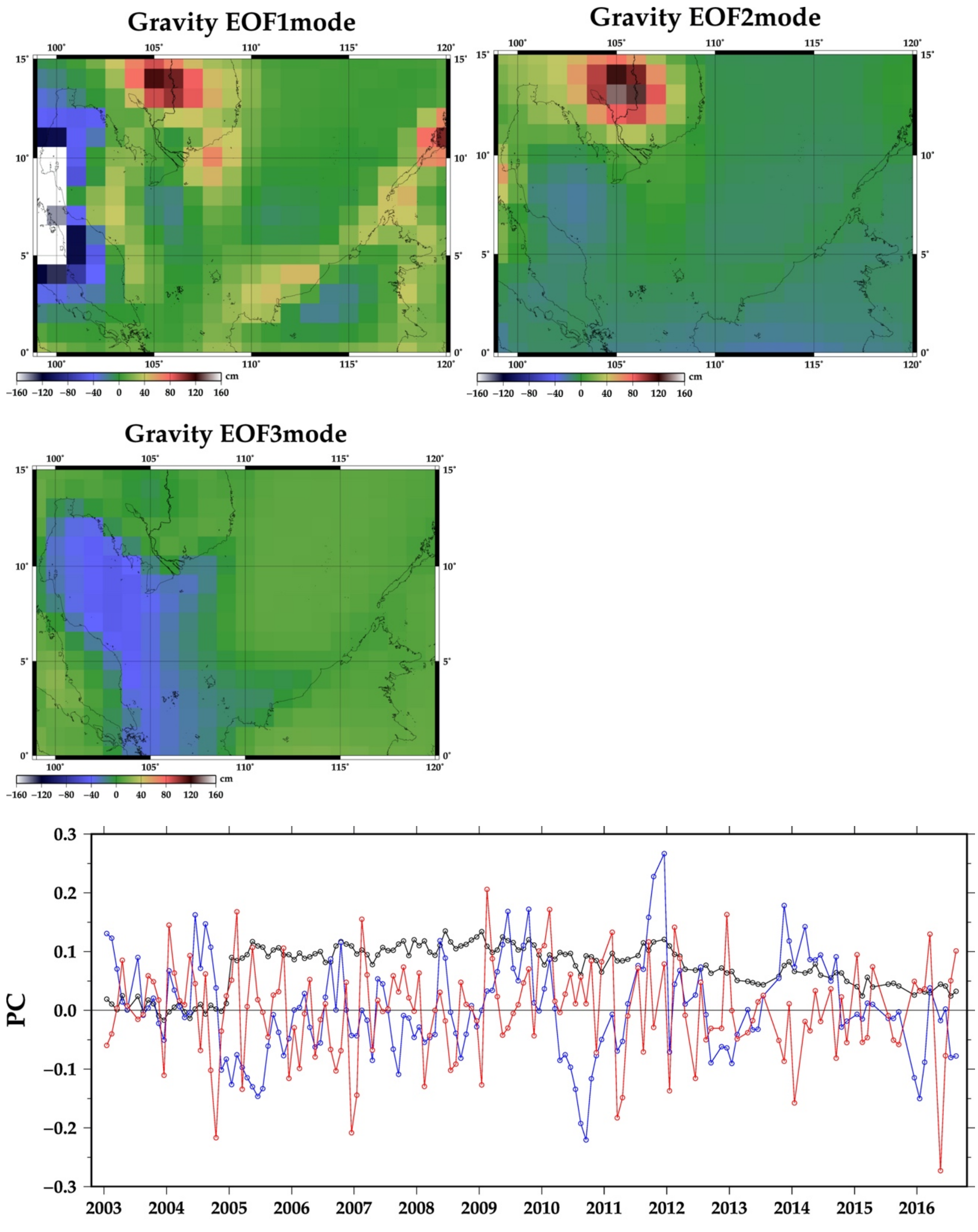

Figure3-24: Result of the EOF analysis on the GRACE data after removal of the linear and seasonal components. In the time function shown at bottom, colors show follows, (black) 1st mode, (blue) 2nd mode and (red) 3rd mode.

3.2.3 Crustal movements

3.2.3.1 GNSS observations

Figure3-25 shows seasonal horizontal displacements of several GNSS stations. NIMT in Bangkok moves only a little. On the other hand, movement of the other 2 stations seems to reflect the gravity contrast between land and sea shown in Figure3-22 and 3-23.

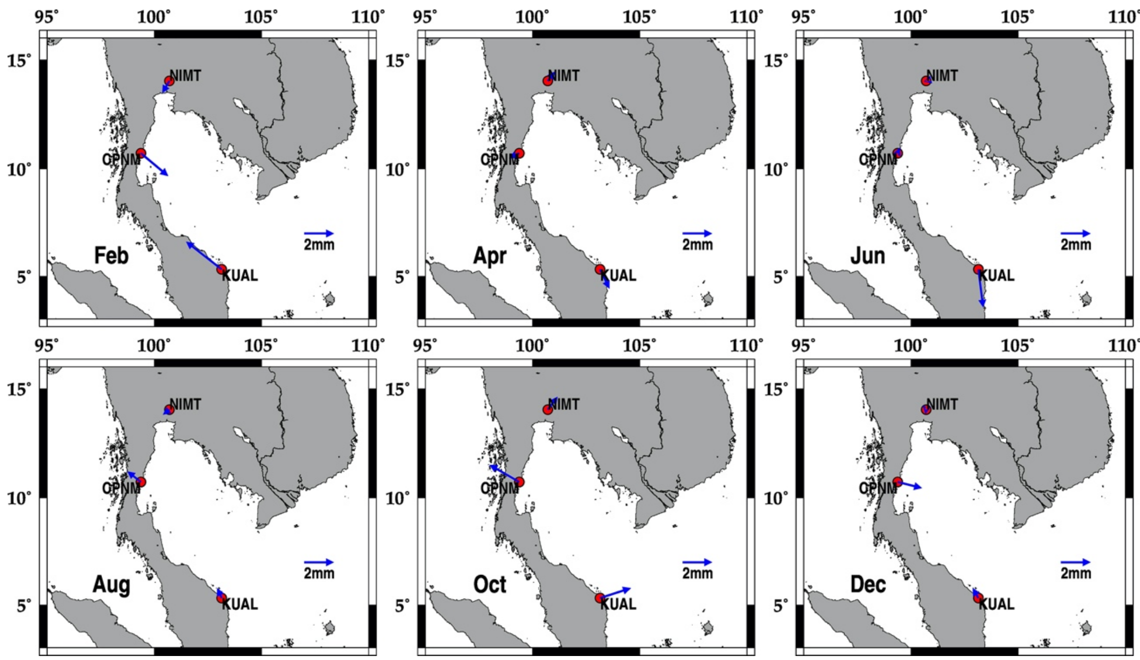

Figure3-25: Monthly averaged seasonal change of horizontal movement observed at three GNSS stations around GOT.

3.2.3.2 Comparison with numerical calculation

Like in the GOC case, I performed numerical calculation of seasonal horizontal crustal movements due to changes in surface load. Calculation results are shown in Figure 3-26. Input data are from GRACE data (land) and from altimeter and tide gauges (ocean). Observed displacements are 2~3 times as large as the calculated displacements. On the other hand, the azimuths of the displacements are roughly consistent with the mass changes on land and ocean (Figure 3-23). There is a significant contradiction at the CPNM station in October. Its calculated and observed azimuths are completely opposite. Calculated displacements are greatly influenced by gravity changes around the Mekong River basin. No large surface load can be seen in direction where GNSS observation points out.

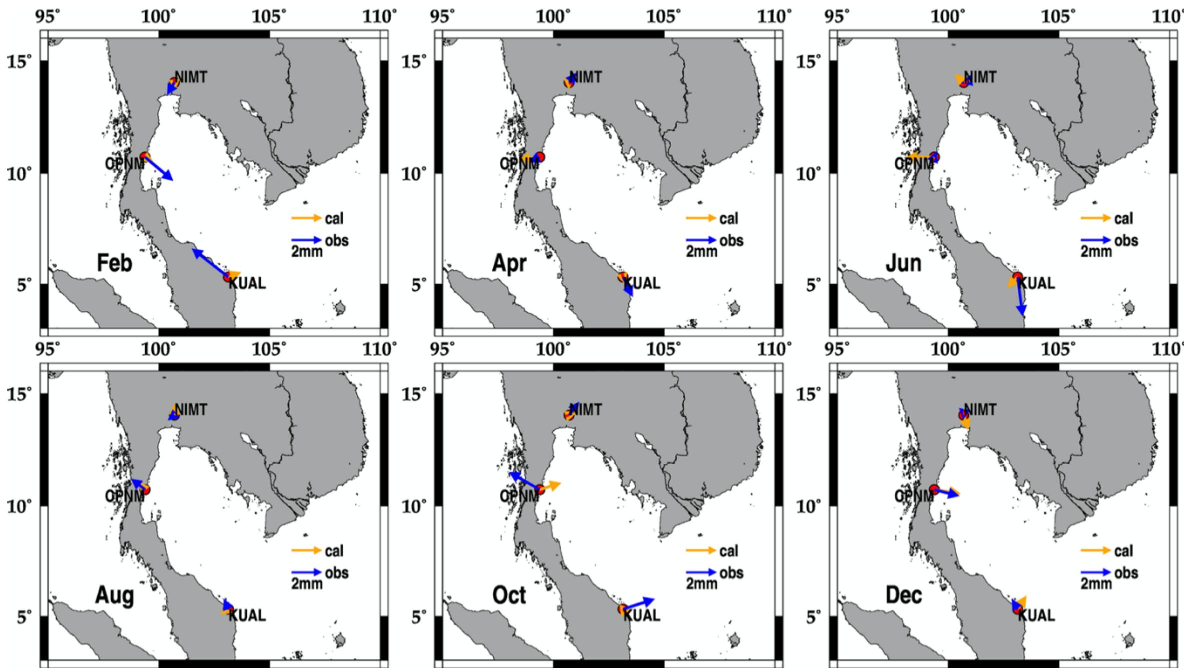

Figure3-26: Result of numerical calculation of horizontal crustal movement (orange) by surface load inferred from GRACE (land) and SSH (ocean). Blue arrow shows GNSS horizontal movement shown in Figure3-25.

Chapter4 Discussion

4.1 3 component of SSH change

4.1.1 Seasonal change

In terms of seasonal change, altimetric data has correlation with that of tide gauge even with tide error.

4.1.1.1 GOC

Amplitude of seasonal change is over 40cm by monthly averaged seasonal change shown in Figure3-7, maximum in February and minimum in July. This result is consistent with results of Wang et al., (2015), which says this seasonal change is caused by wind.

Data of tide gauges show that SSH gets bigger towards the southeast of the GOC, this result is the same as altimeter. According to Wang et al., (2015), it blows southeast winds in austral summer in GOC. Tide gauge records also supports that the seasonal change in this region is caused by wind.

Result of EOF analysis on raw data also shows seasonal change. Amplitude of seasonal change shown in 1st mode is 60cm in maximum, 30cm in minimum. This is not much different from tide gauge records.

4.1.1.2 GOT

Looking at Figure3-20, amplitude of seasonal change is about 40cm, maximum in December and minimum in July. 4 tide gauge records show same phase of seasonal change. 4 records show similar amplitude, because 3 stations are deep of the Gulf. South-east wind is prevailing in winter and North-west wind in summer in South China Sea including GOT [Hu et al., 2000]. Results of altimeter and tide gauges suggest that wind also causes seasonal change in this area.

Result of EOF analysis on raw data says amplitude is about 35cm in maximum and 12cm in minimum, not so much different from tide gauge.

4.1.3 Comparison between GRACE and altimeter

We can see the difference of amplitude of seasonal change between altimeter and GRACE mascon solution by Figure3-7 and 3-20. In GOC, seasonal change by GRACE mascon solution is half of that by altimeter. In GOT, this percentage is over 90%. This difference may come from the uncertainty of GRACE data described in Chapter2. GOC is one of the areas where RMS in SH solution is over 4cm and RMS preserved. Another possible reason is that the GOC is where Australian continent recessed, while GOT has two narrow sides of the surrounding land. Influence of thermosteric factor is small, GRACE data can almost explain that of altimeter in practice.

4.1.4 Inter-annual change

SSH on GOC is influenced by ENSO and IOD. Altimetric influence by ENSO can be seen in thermosteric. From comparison between Figure3-8 and 3-10, signals in spatial function is very similar, especially in Pacific Ocean. Basically, ENSO influence SSH change through thermal expansion.

However, correlation with ENSO also can be seen on GRACE data in GOC. EOF 1st mode shows that there is the signal correlated with ENSO in and around GOC. This result means La Niña works to store water in the gulf. Kleinherenbrink et al., (2017) says ENSO changes Pacific equatorial winds. Fasullo et al., (2013) found that multiple climate changes such as ENSO, IOD and SAM (Southern Annular Mode) caused heavy rainfall in the Australia. They discuss La Niña makes heavy precipitation. Combination of these results appear in the result of EOF 1st mode.

Contrary to ENSO, IOD does not have correlation with GRACE and thermosteric component. IOD also affects thermosteric component of SSH same as ENSO, however the signal is considered poor and hidden in ENSO.

4.2 Comparison between GRACE and GNSS

Horizontal movements of GNSS stations can explain mass changes observed by GRACE? To compare easily, I show Figure 4-1.

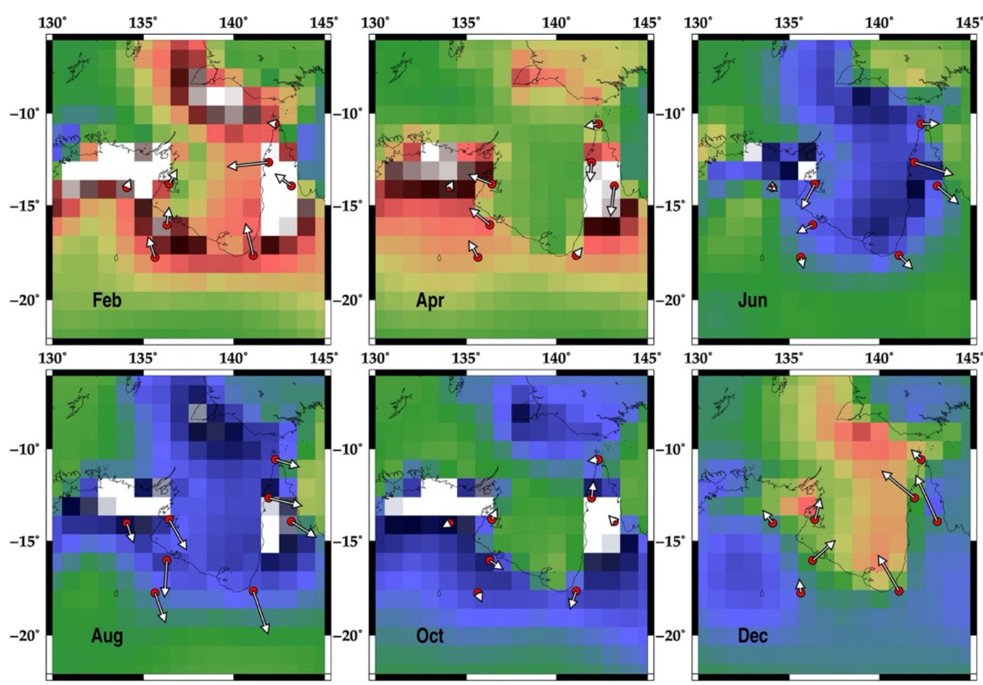

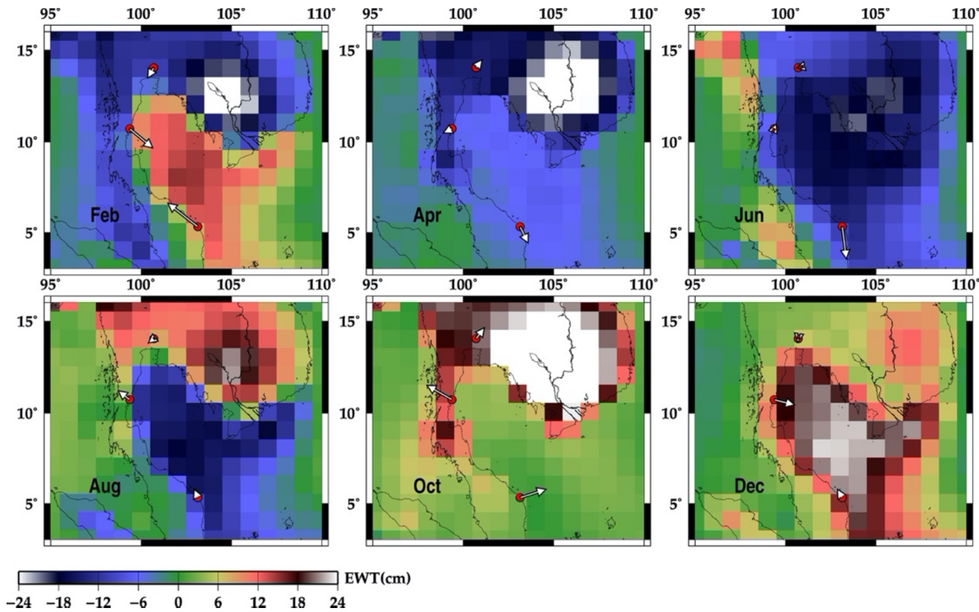

Figure4-1: Averaged seasonal change of GNSS horizontal movement and GRACE mass change (white arrow) around GOC (above) and GOT (below). They are shown in Figure 3-22 and 3-25 respectively.

In and around GOC, GNSS movement explain mass change well. When there is phase difference of seasonal change between land and sea, vectors points to the ocean (land). In summer, minimum of seasonal change in both land and sea, vectors points to out of this region.

The vectors are consistent with data of GRACE also in GOT. Though sometimes the amount of displacement is small compared with surface load, like on December, the azimuths of vector are well reflected surface load observed by GRACE.

4.3 GNSS observation vs numerical calculation

Through numerical calculation described in Chapter3, it is confirmed that mass change observed by GRACE and altimeter can cause the horizontal movement as observed by GNSS.

4.3.1 GOC

Overall, observational value is approximately twice larger than that of result of numerical calculation. In the season when there is negative phase in both land and sea (June to August), difference of value between observation and calculation is small. However, difference become very large in summer (December to February). This is caused by GRACE leakage shown in comparison of SSH. Mascon solution improved leakage between land and ocean, however, it seems like not completely.

On the other hand, direction of displacement is relatively similar. GNSS displacement heads to the ocean in December is surely reflected phase difference between land and ocean. In this way, the vectors of calculation and observation are better much when difference of the seasonal changes between land and sea is remarkable. The major difference with the observation is the lack of the component pointing to the land west of the GOC.

As above, result of numerical calculation suggest the signal on land is less than true. So, I try to perform numerical calculation again with signal that is twice larger than that of Figure3-26 on land. Figure4-2 is the result.

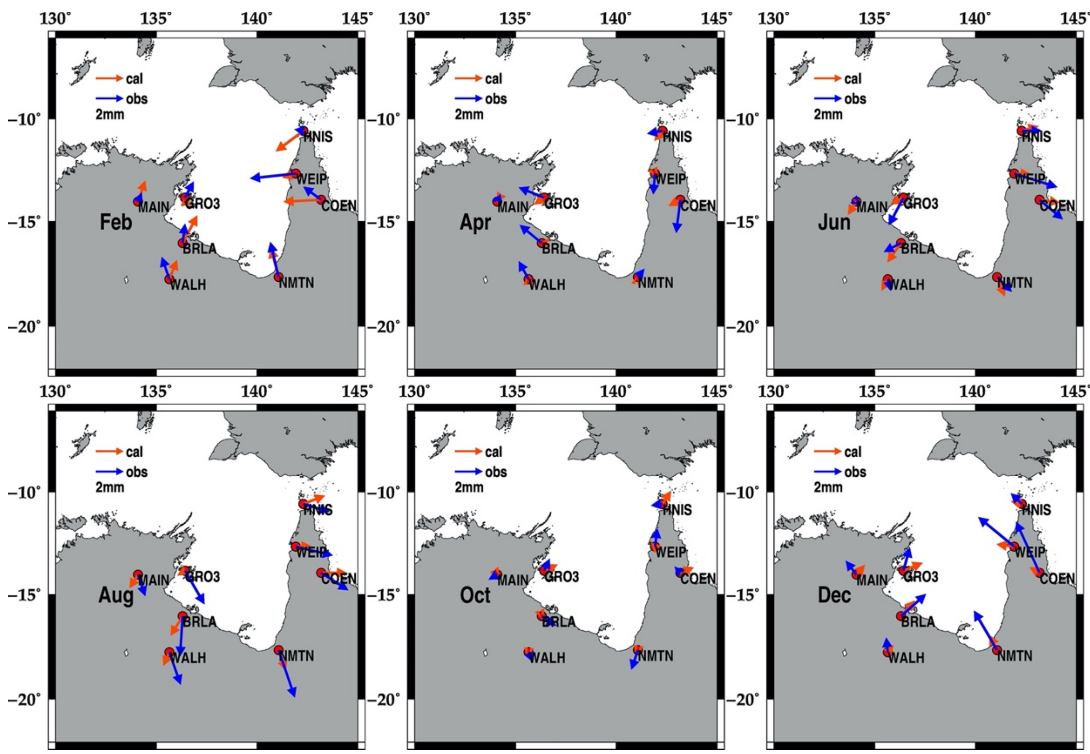

Figure4-2: Result of numerical calculation with signal that is twice larger than that of Figure3-26 on land (orange). Blue arrow shows movement of GNSS station shown in 3-14.

Looking at the result, amount of displacement is much larger than original and comes closer to observation, however the directions are almost unchanged. At the stations located at east and west bank, GRO3 and WEIP, the consistency between calculation and observation is low. This non-consistency is caused by local SSH rise in the coastal region that cannot be seen by GRACE.

4.3.2 GOT

Except at August and December, agreement between observed and calculated value is poor at all stations. NIMT station is in the Bangkok city, so it seems that influence such as subsidence by megacity has large account for GNSS observation. In KUAL station, computed vector is most different in these stations. Possible reason is the actual movement is more influenced by coastal SSH change than computed as described above. CPNM station has the closest computed vector to the observed one, except October. It seems that large positive signal around Mekong River draws. To consider influence of Mekong River, I perform numerical calculation again with load model without signals around Mekong River (assumption: no seasonal change around Mekong River) (Figure4-3).

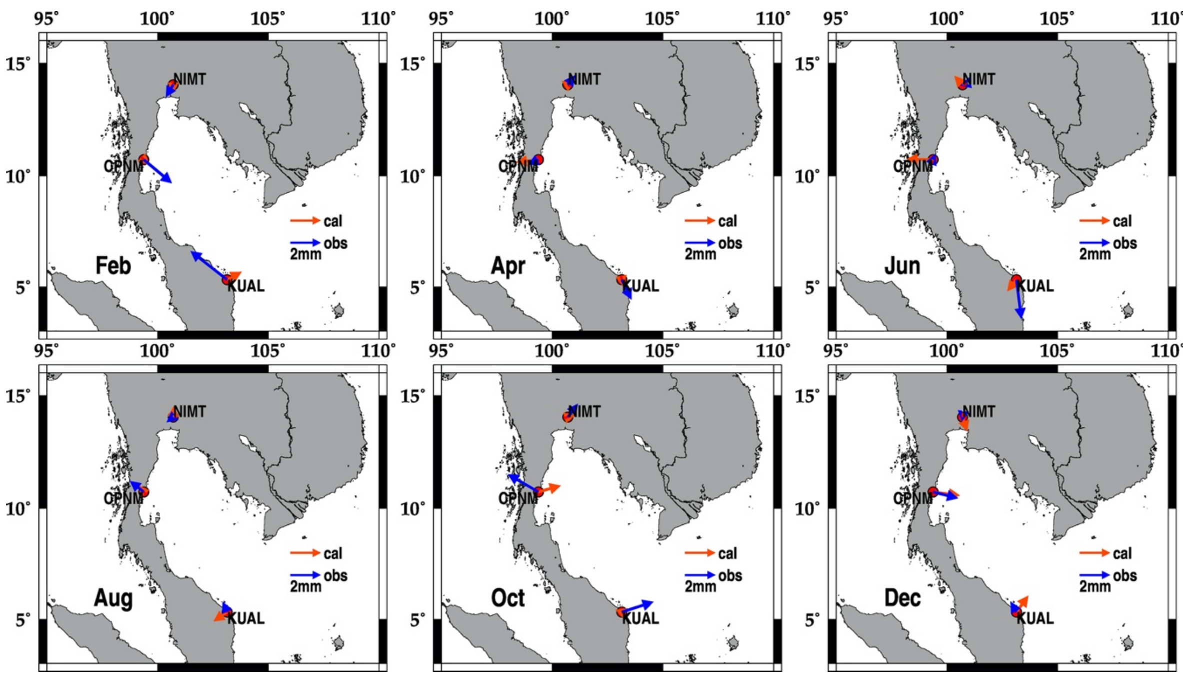

Figure4-3: Result of numerical calculation with load model that remove influence of Mekong River Basin from Figure3-26 (orange). Blue arrow shows movement of GNSS station shown in 3-14.

Even if the influence of the Mekong River Basin is excluded, the vectors do not change so much. As described above, movement of GNSS station well reflects the mass changes observed by GRACE. Because CPNM is located in narrow peninsula, the differences between land and sea do not be reflected completely.

Chapter5 Conclusion

I see changes of SSH and mass in and around the shallow sea, Gulf of Carpentaria and Thailand by multiple geodetic ways. SSH observation by satellites show large seasonal change up to 60cm (GOC) and 50cm (GOT). Most part of seasonal change is mass change driven by wind. Phases of seasonal change in the ocean and on land is different. This is why cause of seasonal change is different, wind and precipitation.

In GOC, inter-annual SSH change is influenced by climate change, most part by ENSO. Influence of ENSO happen through thermosteric components, however, GRACE data also shows correlation with ENSO. This result suggests that the combination of strengthening of wind and precipitation is happened.

For consideration validity of satellites data even with tidal error, I used tide gauge records for SSH and GNSS for crustal movement by surface load.

Monthly averaged seasonal change of tide gauges shows similar phase and amplitude as altimeter and GRACE. Differences of amplitude by location are consistent with the theory that these seasonal change is caused by wind. In GOC, GRACE can capture signals only half of altimeter.

Horizontal movement of GNSS stations is consistent with change of surface load observed by GRACE, including difference of phase of seasonal change. To confirm whether load change observed in GRACE can cause the displacement observed by GRACE, I perform numerical calculation with load data referred GRACE and altimeter. Although there is a tendency that amount of computed displacement is less than that of observation, load change like GRACE can cause the displacement observed by GNSS.

Through analysis of tide gauge records and GNSS observation, altimeter and GRACE data can use in these region even with large tidal error.

In May 22, 2018, GRACE Follow-On (GRACE-FO) was launched and SH RL01 solution has already released. GRACE-FO does not have significant resolution improvement, however, the important point is to keep observation continuously. Future long observation may provide new insights about climate changes. Like GRACE, GNSS observation network is still improving, development of network makes us to observe the load change more easily and extensively.

Chapter6 Acknowledgement

I was taken care of by a lot of people for writing this paper. I express my thanks below.
Before anyone, I should owe my deepest gratitude to Professor Kosuke Heki, my supervisor. From undergraduate laboratory assignment, he has given me lots of support in various situations, theme decision, how to read research paper, presentation and so on. I am sure that I could not do my work without him. Though my research activity end in this master course, I think strongly that what he taught to me will help me in my future working life. It is one of the greatest thing in my life what he is my supervisor.
Next, I want to tell my special thanks to Associate Professor Koji Matsumoto at National Astronomical Observatory of Japan. Figure3-15, 3-26, 4-3 and 4-4 is computed by program made by him. He also introduced papers about tide to me and gave me advise about my study. Those were a great help of my study.
Furthermore, I want to say thanks to all teachers and students of the Solid Seminar in Hokkaido University. In regular seminar, the teachers gave me many advise that improved and helped my study. Thanks to the students, especially students in room 8-306, my laboratory life was happy and interesting.
To close, I am deeply grateful to everyone involved to me for 3 years.

Chapter7 Reference

Resources of figures

https://www.climate.gov/news-features/understanding-climate/climate-change-glacier-mass-balance
https://aquarius.oceansciences.org/cgi/ed_act.htm?id=18
https://www.climate.gov/news-features/climate-tech/reading-between-tides-200-years-measuring-global-sea-level
https://podaac.jpl.nasa.gov/Altimetric_Data_Information/Missions
https://www.data.jma.go.jp/gmd/cpd/db/elnino/index/dattab.html
http://www.bom.gov.au/watl/about-weather-and-climate/australian-climate-influences.shtml?bookmark=enso
https://iri.columbia.edu/our-expertise/climate/enso/
http://www.jamstec.go.jp/aplinfo/sintexf/
https://seos-project.eu/GPS/GPS-c01-p03.html

Resources of programs

Spherical harmonics (http://www.geod.jpn.org/contents/book/program.html)
Crustal displacement by surface loads (https://www.miz.nao.ac.jp/staffs/nao99/)

Resources of data

https://podaac.jpl.nasa.gov
PSMSL (2018) (https://www.psmsl.org/data/obtaining/)
https://www.metoffice.gov.uk/hadobs/en4/download-en4-2-0.html
http://geodesy.unr.edu/NGLStationPages/gpsnetmap/GPSNetMap.html
https://www.aviso.altimetry.fr/en/data/products/sea-surface-height-products/global.html

Alothman, A. O., M. Bos, R. Fernandes, Ali. M. Radwan, M. Rashwan, 2020, Annual sea level variations in the Red Sea observed using GNSS, *Geophysical Journal International*, ggaa032.

Argus, D. F., F. W. Landerer, D. N. Wiese, H. R. Martens, Y. Fu, J. S. Famiglietti, B. F. Thomas, T. G. Farr, A. W. Moore, M. M. Watkins, 2017, Sustained water loss in California's mountain ranges during severe drought from 2012 to 2015 inferred from GPS, *J. Geophys. Res. Solid Earth*, **122**, 10559–10585.

Blewitt, G., W. C. Hammond, and C. Kreemer, 2018, Harnessing the GPS data explosion for interdisciplinary science, *Eos*, **99**.

Castle, S. L., B. F. Thomas, J. T. Reager, M. Rodell, S. C. Swenson, and J. S. Famiglietti, 2014, Groundwater depletion during drought threatens future water security of the Colorado River Basin. *Geophys. Res. Lett.*, **41**(16), 5904–5911.

Cazenave, A., 2018, Global sea-level budget 1993–present, *Earth Syst. Sci. Data*, **10**, 1551–1590.

Chambers, D. P., A. Cazenave, N. Champollion, H. B. Dieng, W. Llovel, R. Forsberg, K. von Schuckmann, and Y. Wada, 2017, Evaluation of the global mean sea level budget between 1993 and 2014, *Surv. Geophys.*, **38**, 309–327.

Chanard, K., J. P. Avouac, G. Ramillien, and J. Genrich, 2014, Modeling deformation induced by seasonal variations of continental water in the Himalaya region: Sensitivity to Earth elastic structure, *Journal of Geophysical Research: Solid Earth*, **119**, 5097– 5113.

Farrell, W. E., 1972, Deformation of the earth by surface loads, *Rev. Geophys. Space Phys.*, **10**, 761–797.

Fasullo, J. T., C. Boening, F. W. Landerer, R. S. Nerem, 2013, Australia's unique influence on global sea level in 2010–2011, *Geophys Res Lett.*, **40**, 4368–4373.

Feng, W., M. Zhong, J.-M. Lemoine, R. Biancale, H.-T. Hsu, and J. Xia, 2013, Evaluation of groundwater depletion in North China using the Gravity Recovery and Climate

Experiment (GRACE) data and ground-based measurements, *Water Resour. Res.*, **49**, 2110–2118.
Forbes A. M. J., and J. A. Church, 1983, Circulation in the Gulf of Carpentaria. II. Residual currents and mean sea level, *Aust J Mar Freshw Res*, **34**(1), 11–22.
Geruo, A., J. Wahr, and S. Zhong, 2013, Computations of the viscoelastic response of a 3-D compressible earth to surface loading: An application to glacial isostatic adjustment in Antarctica and Canada, *Geophys. J. Int.*, **192**(2), 557–572.
Gharineiat Z., X. Deng, 2018, Description and assessment of regional sea-level trends and variability from altimetry and tide gauges at the northern Australian coast, *Adv Space Res*, **61**(10), 2540–2554.
Good, S. A., M. J. Martin and N. A. Rayner, 2013, EN4: quality controlled ocean temperature and salinity profiles and monthly objective analyses with uncertainty estimates, *Journal of Geophysical Research: Oceans*, **118**, 6704-6716.
Heiskanen, W. and H. Moritz, 1967, Physical Geodesy.
Heki, K. and K. Matsuo, 2010, Coseismic gravity changes of the 2010 earthquake in Central Chile from satellite gravimetry, *Geophys. Res. Lett.*, **37**, L24306.
Heki, K. and Y. Mitsui, 2013, Accelerated Pacific Plate subduction following interplate thrust earthquakes at the Japan Trench, *Earth Planet. Sci. Lett.*, **363**, 44-49.
Hellerman, S., and M. Rosenstein, 1983, Normal monthly wind stress over the world's ocean with error estimates, *J. Phys. Oceanogr.*, **13**, 1093-1104.
Holgate, S. J., A. Matthews, P. L. Woodworth, L. J. Rickards, M. E. Tamisiea, E. Bradshaw, P. R. Foden, K. M. Gordon, S. Jevrejeva, and J. Pugh, 2013, New data systems and products at the permanent service for mean sea level, *J. Coastal Res.*, **29**(3), 493–504.
Hu, J., H. Kawamura, H. Hong, Y. Qi, 2000. A review on the currents in the South China Sea: seasonal circulation, South China Sea warm current and Kuroshio intrusion, *J. Oceanogr*, **56**, 607–624.
Ichikawa, K., 2014, 21 世紀初頭の衛星海面高度計. *Oceanography in Japan*, **23**(1), 13-27.
IPCC, 2013, Climate Change 2013, *The Physical Science Basis. Contribution of Working Group I to the Fifth Assessment Report of the Intergovernmental Panel on Climate Change*, [Stocker, T. F., D. Qin, G.-K. Plattner, M. Tignor, S. K. Allen, J. Boschung, A. Nauels, Y. Xia, V. Bex and P. M. Midgley (eds.)], Cambridge University Press, Cambridge, United Kingdom and New York, NY, USA, 1535 pp.
Kaula, W. M., 1966, Tests and combination of satellite determinations of the gravity field with gravimetry, *J. geophys. Res.*, **71**, 5303-5314.
Landerer, F., and S. Swenson, 2012, Accuracy of scaled GRACE terrestrial water storage estimates, *Water Resour. Res.*, **48**, W04531.
Laven, K. V., 2010, Gridsphere Code.
[Available at https://www.mathworks.com/matlabcentral/fileexchange/28842-grid-sphere]
Munekane, H., 2013, 下から見た衛星重力ミッション GRACE, *測地学会誌*, **59**(3), 111-118.
Matsumoto, K., T. Sato, T. Takanezasa, and M. Ooe, 2001, GOTIC2: A program for computation of oceanic tidal loading effect, *J. Geod. Soc. Jpn.*, **47**, 243– 248.
Matsuo, K., and K. Heki, 2010, Time-variable ice loss in Asian high mountains from satellite gravimetry, *Earth Planet. Sci. Lett.*, **290**, 30-36.
Matsuo, K., and K. Heki, 2011, Coseismic gravity changes of the 2011 Tohoku-Oki Earthquake from satellite gravimetry, Geophys. Res. Lett., 38, L00G12.
Matsuo, K., and K. Heki, 2013, Current ice loss in small glacier systems of the Arctic Islands from satellite gravimetry, *Terr. Atmos. Ocean. Sci.*, **24**, 657-670.
Matsuo, K., and K. Heki, 2014, Glacier mass balance in Asian high mountains: Reconsideration of satellite gravimetry estimates, *Seppyo*, **76**, 45-57.
Morishita, Y., and K. Heki, 2008, Characteristic precipitation patterns of El Nino / La Nina in time-variable gravity fields by GRACE, *Earth Planet. Sci. Lett.*, **272**, 677-682.
Nerem, R. S., B. D. Beckley, J. T. Fasullo, B. D. Hamlington, D. Masters, and G. T. Mitchum, 2018, Climate-change–driven accelerated sea-level rise detected in the altimeter era, *Proceedings of the National Academy of Sciences*, **115**(9), 2022-2025.

Ogawa, R. and K. Heki, 2007, Slow postseismic recovery of geoid depression formed by the 2004 Sumatra-Andaman Earthquake by mantle water diffusion, *Geophys. Res. Lett.*, **34**, L06313.
Oliver, E. C. J., and K. R. Thompson, 2011, Sea level and circulation variability of the Gulf of Carpentaria: Influence of the Madden-Julian Oscillation and the adjacent deep ocean, *Journal of Geophysical Research*, **116**, C02019.
Tanaka, Y., and K. Heki, 2014, Long- and short-term postseismic gravity changes of megathrust earthquakes from satellite gravimetry, *Geophys. Res. Lett.*, **41**, 5451-5456.
Tanaka, Y., K. Heki, K. Matsuo, and N. V. Shestakov, 2015, Crustal subsidence observed by GRACE after the 2013 Okhotsk deep-focus earthquake, *Geophys. Res. Lett.*, **42**.
Reager, J. T., A. S. Gardner, J. S. Famiglietti, D. N. Wiese, A. Eicker, and M.-H. Lo, 2016, A decade of sea level rise slowed by climate-driven hydrology, *Science,* **351**(6274), 699-703.
Rietbroek R., S. E. Brunnabend, J. Kushche, J. Schröter, C. Dahle, 2016, Revisiting the contemporary sea-level budget on global and regional scales, *Proceedings of the National Academy of Sciences*, **113**, 1504–1509.
Rodell, M., J. S. Famiglietti, D. N. Wiese, J. T. Reager, H. K. Beaudoing, F. W. Landerer, and M.-H. Lo, 2018, Emerging trends in global freshwater availability, *Nature*, **557**, 651–659.
Rowlands, D., S. Luthcke, J. McCarthy, S. Klosko, D. Chinn, F. Lemoine, J.-P. Boy, and T. Sabaka, 2010, Global mass flux solutions from GRACE: A comparison of parameter estimation strategies—Mass concentrations versus stokes coefficients, *J. Geophys. Res.*, **115**, B01403.
Save, H., S. Bettadpur, and B. D. Tapley (2012), Reducing errors in the GRACE gravity solutions using regularization, J. Geod., 86(9), 695–711.
Save, H., S. Bettadpur, and B. D. Tapley, 2016, High resolution CSR GRACE RL05 mascons, *J. Geophs. Res. Solid Earth*, **121**, 7547–7569.
Stammer, D., R. D. Ray, O. B. Andersen, B. K. Arbic, W. Bosch, L. Carrère, Y. Cheng, D. S. Chinn, B. D. Dushaw, G. D. Egbert, S. Y. Erofeeva, H. S. Fok, J. A. M. Green, S. Griffiths, M. A. King, V. Lapin, F. G. Lemoine, S. B. Luthcke, F. Lyard, J. Morison, M. Müller, L. Padman, J. G. Richman, J. F. Shriver, C. K. Shum, E. Taguchi, Y. Yi, 2014, Accuracy assessment of global barotropic ocean tide models, *Rev. Geophys.*, **52**(3), 243-282.
Swenson, S., and J. Wahr, 2006, Post-processing removal of correlated errors in GRACE data, *Geophys. Res. Lett.*, **3**3, L08402.
Tapley, B., B. Schutz, and G. H. Born (2004a), *Statistical Orbit Determination*, Academic Press.
Tanaka, Y., and K. Heki, 2016, GRACE seismology: Review and perspective of satellite gravimetry for earthquake sciences, *Zisin 2*, **69**, 69-85.
Tregoning, P., G. Ramillien, and K. Lambeck, 2008, GRACE estimates of sea surface height anomalies in the Gulf of Carpentaria, Australia, *Earth Planet. Sci. Lett.*, **271**, 241–244.
Trisirisatayawong I., M. Naeije, W. Simons, and L. Fenoglio-Marc, 2011, Sea level change in the gulf of Thailand from GPS-corrected tide gauge data and multi-satellite altimetry, *Global and Planetary Change*, **76**, 137–151.
Tu, Y., and K. Heki, 2017, Decadal modulation of repeating slow slip event activity in the southwestern Ryukyu Arc possibly driven by rifting episodes at the Okinawa Trough, *Geophys. Res. Lett.*, **44**, 9308-9313.
Yi, S., K. Heki, and A. Qian, 2017, Acceleration in the global sea level rise: 2005-2015, *Geophys. Res. Lett.*, **44**(11), 905-911.
Wahr, J., M. Molenaar, and F. Bryan, 1998, Time variability of the Earth's gravity field: Hydrological and oceanic effects and their possible detection using GRACE, *J. Geophys. Res.*, **103**(B12), 30205–30229.
Wahr, J., S. A. Khan, T. van Dam, L. Liu, J. H. van Angelen, M. R. van den Broeke, and C. M. Meertens, 2013, The use of GPS horizontals for loading studies, with applications to northern California and southeast Greenland, *Journal of Geophysical Research: Solid Earth*, **118**, 1795–1806.

Wang, J., J. Wang, and X. Cheng, 2015, Mass-induced sea level variations in the Gulf of Carpentaria, *J. Oceanogr.*, **71**(4), 449-461.
Wang, L., C. K. Shum, F. J. Simons, B. Tapley, and C. Dai, 2012, Coseismic and postseismic deformation of the 2011 Tohoku-Oki earthquake constrained by GRACE gravimetry, *Geophys. Res. Lett.*, **39**, L07301.
Wouters, B., and D. P. Chambers, 2010, Analysis of seasonal ocean bottom pressure variability in the Gulf of Thailand from GRACE, *Global and Planetary Change*, **74**, 76–81.